MICROCOPY RESOLUTION TEST CHART

NATIONAL BUREAU OF STANDARDS 1963-A

AFOSR·TR· 86-2114

FIRST ANNUAL TECHNICAL REPORT

on

Al and Mg ALLOYS FOR AEROSPACE APPLICATIONS
USING RAPID SOLIDIFICATION AND POWDER
METALLURGY PROCESSING

Submitted by

Hamish L. Fraser
Department of Materials Science
University of Illinois
1304 W. Green Street
Urbana, IL 61801

DTIC
ELECTE
DEC 1 2 1986
S
D
D

REPORT DOCUMENTATION PAGE

1a. REPORT SECURITY CLASSIFICATION	1b. RESTRICTIVE MARKINGS
Unclassified	
2a. SECURITY CLASSIFICATION AUTHORITY	3. DISTRIBUTION/AVAILABILITY OF REPORT
2b. DECLASSIFICATION/DOWNGRADING SCHEDULE	Approved for public release; distribution unlimited.

4. PERFORMING ORGANIZATION REPORT NUMBER(S)	5. MONITORING ORGANIZATION REPORT NUMBER(S)
	AFOSR·TR· 86-2114

6a. NAME OF PERFORMING ORGANIZATION	6b. OFFICE SYMBOL (If applicable)	7a. NAME OF MONITORING ORGANIZATION
Univ. of Illinois		AFOSR

6c. ADDRESS (City, State and ZIP Code)	7b. ADDRESS (City, State and ZIP Code)
Dept of Material Science 1304 W. Green St. Urbana, Il 61801	Bld 410 Bolling AFB DC

8a. NAME OF FUNDING/SPONSORING ORGANIZATION	8b. OFFICE SYMBOL (If applicable)	9. PROCUREMENT INSTRUMENT IDENTIFICATION NUMBER
AFOSR	NE	AFOSR-85-0191

8c. ADDRESS (City, State and ZIP Code)	10. SOURCE OF FUNDING NOS.			
Bld 410 BAFB D.C 20332-6448	PROGRAM ELEMENT NO.	PROJECT NO.	TASK NO.	WORK UNIT NO.
	61102F ~~2306~~	2306 ~~A1~~	A1	

11. TITLE (Include Security Classification) Al and Mg Alloys for Aerospace Applications Using Rapid Solidification and Powder Metallurgy Processing

12. PERSONAL AUTHOR(S) Hamish L. Fraser

13a. TYPE OF REPORT	13b. TIME COVERED	14. DATE OF REPORT (Yr., Mo., Day)	15. PAGE COUNT
Annual	FROM May 85 TO May 86	11/14/86	

16. SUPPLEMENTARY NOTATION

17.	COSATI CODES		18. SUBJECT TERMS (Continue on reverse if necessary and identify by block number)
FIELD	GROUP	SUB. GR.	

19. ABSTRACT (Continue on reverse if necessary and identify by block number)

The microstructures and mechanical properties of rapidly solidified Al-and Mg-based alloys were investigated. Rapidly solidified particulate was produced by either laser surface melting (LSM) and self-quenching, melt spinning or centrifugal atomization. Consolidation of particulate produced by the latter two techniques was achieved by either extrusion or dynamic compaction. The first area of work involved the high modulus Al-Be and Al-MN alloys. The elastic modulus of solution-treated Al-Mn alloys increased with an increase in Mn content at the rate of 10GPa/at% Mn, consistent with theoretical predictions of solid solution effects. The second area of work concerned the Al alloys for elevated temperature applications, namely alloys. The microstructures and mechanical properties of the Al-8Fe-2Mo alloy, consolidated by either extrusion or dynamic compaction were investigated. The third area of work concerned Mg alloys for elevated temperature applications. Rapid solidification processing was successfully used to produce a refined dispersion of Mg_2Si in the matrix of Mg-Li alloys.

20. DISTRIBUTION/AVAILABILITY OF ABSTRACT	21. ABSTRACT SECURITY CLASSIFICATION
UNCLASSIFIED/UNLIMITED ☐ SAME AS RPT. ☐ DTIC USERS ☐	UUUU

22a. NAME OF RESPONSIBLE INDIVIDUAL	22b. TELEPHONE NUMBER (Include Area Code)	22c. OFFICE SYMBOL
Dr. Alan Rosenstein	767-4933	NE

DD FORM 1473, 83 APR EDITION OF 1 JAN 73 IS OBSOLETE.

TABLE OF CONTENTS

Dist   Avail and/or
             Special

A-1

1. INTRODUCTION

> This report covers the progress made in the first year of a three year study on the rapid solidification processing (RSP) of Al- and Mg-based alloys. In this study, effort has been applied in three areas: 1) Processing (both particulate production and consolidation), 2) Microstructural effects, and 3) Mechanical properties. The underlying objective has been to control the microstructure to obtain favorable mechanical properties. This will, perforce, entail a detailed understanding of the microstructures, as affected by factors such as alloy chemistry and processing variables, and, in turn, their effects on the mechanical properties. The microstructural changes which occur in heat-treated, as-rapidly solidified materials, as well as those in materials consolidated, either by extrusion or by the relatively new technique of dynamic compaction, have been investigated. The alloy systems studied include: 1) high modulus Al alloys, namely, Al-Mn and Al-Be, 2) Al alloys for elevated temperature applications, namely, Al-8Fe-2Mo, and 3) Mg alloys for elevated temperature applications, namely, Mg-20Gd and Mg-Li-Si. The report is divided into three major sections: 1) Brief overview of RSP of individual alloys, 2) Results, and 3) Future work. Individual sections are further subdivided as appropriate.

2. BACKGROUND

2.1 High Modulus Al Alloys (Al-Mn and Al-Be)

The development of high strength Al alloys, combined with the need to limit component weight in aircraft, has led to a situation where it is possible that material failures in compression members will be characterized by elastic instability rather than yielding. The material parameter governing structural stability is the elastic modulus. Changes in the elastic modulus can occur either by solid solution effects or by the presence of a second phase. In the first case, Leigh [1] has shown theoretically that any solute which decreases the electron concentration of Al will result in an increase in the modulus. This electronic effect is well demonstrated in Al-Li [2] where the Li in solid solution causes an increase in the modulus. In the second case, the modulus can be increased by forming a composite where the matrix is elastically constrained by dispersions of a less compliant second phase [3-5].

The theoretical formulations of Paul [6] have shown that the elastic modulus of a composite should lie between an upper and lower bound condition given approximately by:

$$E_p.E_m/[(1-V_p).E_m + V_p.E_p] < E_c < (1-V_p).E_m + V_p.E_p) \qquad (1)$$

1

where V_p is the volume fraction of the second phase particles, and E_c, E_m and E_p refer to the elastic modulus of the composite, matrix and particle, respectively. The difference between these bounds is small, provided that the ratio of E_p/E_m is less than about three. In the alternative formulation of Hashin and Shtrikman[7], these upper and lower limits are derived by calculations of the upper and lower limits for the bulk modulus, K, and the shear modulus, G, and, in turn, relate these to the elastic modulus by:

$$E = 9KG/(3K + G) \qquad (2)$$

The important point that emerges (see equation 1) is that the modulus of the composite increases with both the modulus and volume fraction of the second phase particles.

RSP provides a method of producing novel microstructures in the form of extended solid solutions and/or refined second phase constituents. From the standpoint of increasing elastic modulus, alloys based on Al-Mn and Al-Be are of particular interest. For Al-Mn alloys, not only can extended solid solutions containing up to 6 at.% Mn be obtained by RSP [8], but additional increments in elastic modulus are expected over alloys produced by traditional methods, where an increase in modulus of 4.8 GPa/at pct%Mn have been reported [2]. Novel microstructures and mechanical properties of RSP Al-Be alloys have also been reported [9,10]. In these alloys, the RSP microstructure consists of a refined dispersion of Be particles in a Al matrix. As a result, the changes in elastic modulus are expected to follow the lower composite bound, where the behavior is best approximated by an elastically-soft matrix with elastically-hard spherical inclusions. In this report, the mechanical properties and microstructures of RSP Al-Be and Al-Mn alloys after thermomechanical processing are reported.

2.2 Al Alloys for Elevated Temperature Applications (Al-8Fe-2Mo)

Development of Al alloys for elevated temperature use has been a continuing goal [11]. The interest has stemmed primarily from the need to improve elevated temperature properties, while simultaneously effecting a reduction in the weight of components. Secondly, there is interest in replacing components fabricated from Ti alloys with those of advanced Al alloys, not only from the standpoint of weight savings, but also because of the difficulties associated with the processing of Ti alloys.

Following the initial RSP work of Jones [12], alloys based on Al-8 wt% Fe containing approximately 2 wt% Mo or Ce have emerged as potential candidates for elevated temperature applications [11,13-16]. The microstructures of RSP particulate produced in these alloys have been

described on an optical scale as either Zone A or Zone B, the former appearing featureless in response to etching by Keller's reagent, the latter exhibiting strong contrast. On a finer scale, the Zone A microstructure appears as a cellular-dendritic structure based on α-Al with intercellular regions composed of a randomly oriented, refined distribution of particles of the quasi-crystalline T' phase [17]. One attractive aspect of the Zone A microstructure, which makes production of material containing large quantities of it highly desirable, is its relatively high hardness [12]; this hardness is associated with the refined dispersion of the T' intercellular phase [15,17]. Unfortunately, for the typical size distributions of powders produced by conventional RSP techniques, with the exclusion of the smallest sizes ($\approx$ 3 μm), the microstructure consists of a mixture of Zone A and Zone B [14], which, in turn, leads to considerable variations in properties. Models based on the relationships between undercooling, cooling rate and the heat transfer coefficient have been proposed [14,15,17] not only to successfully explain the evolution of these specific microstructures, but also to develop a processing scheme, via melt spinning, to produce particulate whose microstructures are composed entirely of Zone A.

It has been shown during research performed in AFOSR-82-0186 [15] that the Zone A microstructure produced in the Al-8Fe-2Mo alloy by melt spinning is remarkably stable against decomposition at temperatures up to 400°C; this effect is associated with the stabilizing influence of Mo on the quasi-crystalline T' phase.[18] Alternatively, consolidation by extrusion results in a decomposed microstructure, with disappointingly poor fracture toughness; this being attributed to oxide particles entrained from the prior particle surfaces and an unfavorable morphology of precipitated second phase intermetallics [15,18]. There are two possible approaches to alleviate this problem. The first approach is to utilize proper vacuum degassing techniques for particulate coupled with modifications in alloy chemistry to produce a more favorable morphology and possibly character of the second phase precipitates. This route has been adopted by Das and co-workers [19-21], who showed that Si additions to Al-8Fe-V alloys produces a more attractive morphology of precipitates, accompanied by appreciable improvements in fracture toughness. In view of these findings, a study on the effect of Si on Al-8Fe-2Mo alloys was undertaken, preliminary results of which are reported here. The second approach is to use cold compaction techniques, namely, dynamic compaction, where the integrity of the Zone A microstructure is preserved.

Dynamic compaction is a consolidation technique which has only recently been applied to rapidly solidified particulate [22]. It differs from the traditional powder consolidation techniques such as extrusion in that it is a "cold" process. Because of this unique feature, dynamic compaction is thought to offer good potential for the consolidation of RS particulate with retention of the RS microstructure. Preliminary results of these studies were reported earlier [18]; results of further progress made and of those involving combinations of dynamic compaction and hot

isostatic pressing (HIP) are reported here.

2.3 Mg Alloys for Elevated Temperature Applications (Mg-Gd and Mg-Li-Si)

There have been a number of attempts to strengthen magnesium alloys for elevated temperature service [23,24]. One method involves alloying with elements that form a fine network of stable precipitates within the matrix; thorium and zirconium are standard alloying elements used for this purpose. Another method involves alloying with elements that exhibit both a large maximum solid solubility in magnesium and a rapid decrease in solubility with decreasing temperature. Using elements with these properties, the alloys can be solution heat-treated, quenched, and subsequently aged to produce a refined dispersion of second phase particles. The most successful alloying additions are those which give rise to thermally stable precipitates. For example, aluminum and zinc are excellent additions for room temperature applications because they form large volume fractions of precipitates while not substantially increasing the density of the alloy; however, the compounds formed upon aging these alloys are not thermally stable. For elevated temperature applications, more suitable alloying elements are the rare earth elements yttrium, gadolinium, and terbium. The maximum solid solubilities for several alloying elements [24], the precipitating phases [25], and their decomposition temperatures [24] are shown in Table 1. The decomposition temperature may be used to give a rough estimate of the strength and stability of the phase. The highest elevated temperature strengths have been reported for alloys containing gadolinium and terbium. This has been attributed to the combined effects of the large maximum solid solubility of these elements in magnesium near the eutectic temperature, which allows relatively large volume fractions of second phase particles to be produced via heat treatment, and also the high strength of the ordered intermetallic phases that form during precipitation. The property improvements obtained by using these rare earth additions can be substantial when compared to alloys produced with conventional alloying elements, as is evident from the 150% increase in tensile properties for a heat treated Mg-20wt%Gd alloy when compared to conventional Mg-Th alloy identically processed [24]. The thermal stability of the microstructure was not specified, but creep data for the alloy showed improvement over standard alloys.

Although the use of rare earth alloying additions in magnesium appear to yield excellent results, several disadvantages may limit the use of these alloys. A primary concern involves the thermal stability of the phases precipitated during heat treatment. The product of solubility and diffusivity is the most important parameter in the coarsening rate for Ostwald ripening and although the rare earths have a low diffusivity in magnesium, their solubility, especially for gadolinium, yttrium, and terbium, are very high at elevated temperatures. Age hardened alloys are optimized when the product of solubility and diffusivity are maximized (providing there is a rapid decrease in

4

solubility with temperature), whereas the coarsening rate is lowest when this parameter is minimized. It may be found after further study that the long term property improvements may not be realized due to coarsening effects. The second problem with these alloys is their high density. Because they contain large quantities of rare earths, the densities of the alloys are increased by about 18%. For example, the alloys Mg-20Gd and Mg-20Tb have densities of 2.06 g/cm^3 and 2.07 g/cm^3, respectively, compared to 1.74 g/cm^3 for unalloyed magnesium.

Table 1

Values for the maximum solubility for several alloying elements in magnesium.
The precipitating phases and the decomposition temperatures for the phases are included.

System	Maximum solubility (wt%)	Precipitating Phase	Decomposition Temperature (°C)
Mg-Al	12.7	$Mg_{17}Al_{12}$	462
Mg-Zn	8.4	$MgZn$	347
Mg-Y	12.0	$Mg_{24}Y_5$	605
Mg-Gd	23.5	$Mg_{24}Gd_5$	640
Mg-Tb	24.0	$Mg_{24}Tb_5$	580
Mg-Th	5.0	$Mg_{23}Th_6$	772
Mg-Si	≈zero	Mg_2Si	1097

As an alloying element for magnesium, lithium is unique (Fig. 1) [26]. The hcp α-magnesium matrix is retained with the addition of lithium to 5.5wt% (17at%)Li, and at lithium concentrations greater than 10.9wt% (30at%) the matrix is bcc β-lithium. Small additions of lithium lower the c/a ratio of α-magnesium, improving the ductility and workability of the matrix [27]. The increase in ductility has been attributed to prismatic slip of the type {1010} <1210> occurring simultaneously with basal slip {0001} <1210> at room temperature [28,29]. These two types of slip lead to four of the five independent slip systems necessary for the general accommodation of deformation of the specimen, with the additional deformation coming from twinning and/or slip on other systems. The cubic β-lithium matrix is easily deformable at room temperature and large ductilities have been observed [30]; however, the observed tensile strength was low. In an attempt to strengthen these cubic alloys, additions of Cd, Zn, Al, and Ag have

found to decompose at room temperature, with an accompanying loss in the strength of the alloy.

Both the α and β alloys exhibit low elevated temperature properties, and attempts to improve this situation using silicon additions have been only partially successful [32]. Silicon additions to these alloys are attractive because this element produces a dispersion of coarse Mg_2Si particles within the matrix and it also has a very low solid solubility in magnesium; 0.0032wt% (0.0028at%) at 635°C [33]. This low solubility reduces the rate at which the Mg_2Si dispersoids coarsen, but should preclude the formation of precipitates by a standard aging process. In conventionally processed alloys, the silicide dispersions act only as a grain-refiner and a grain growth inhibitor; no aging response has been observed in magnesium-lithium-silicon alloys. If a fine dispersion of Mg_2Si particles can be formed, either by aging or by refining the solidification structure, then these particles should exhibit improved elevated temperature stability when compared to those formed by conventional solution and aging treatments. If rapid solidification of these alloys produces a metastable supersaturation of silicon in the magnesium matrix, a fine precipitate dispersion may be produced by controlled thermal treatment of the alloy. This may be a viable method of increasing the usable temperature range of magnesium alloys. In the present study, the microstructure and aging response of rapidly solidified magnesium-lithium-silicon alloys has been investigated using x-ray and analytical electron microscopy techniques.
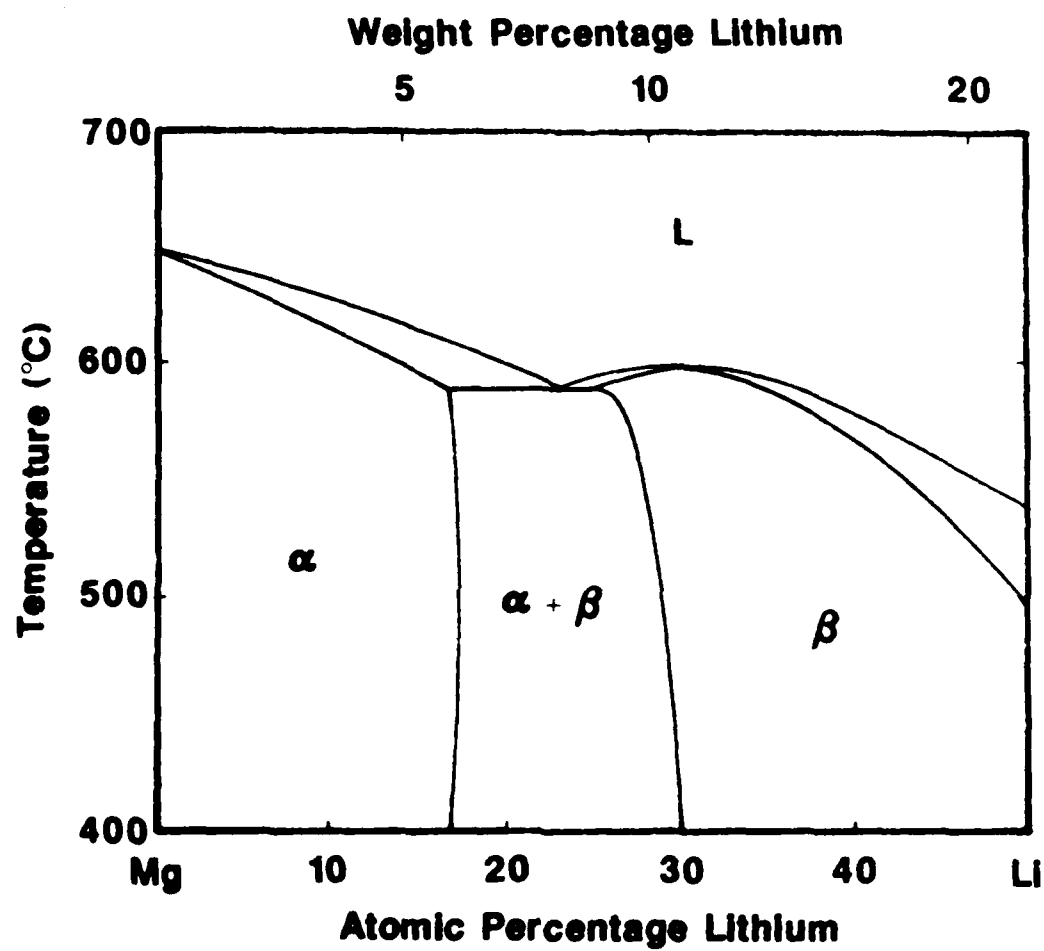
Fig. 1. Partial Mg-Li phase diagram.

3. RESULTS

3.1 Al-Be and Al-Mn Alloys

In the following, the microstructure and mechanical properties of conventionally cast and rapidly solidified Al-Be and Al-Mn alloys are reported.

3.1.1 Microstructures of Al-Be Alloys

The as-cast microstructure of Al-Be alloys exhibits primary dendrites of Be, together with a eutectic mixture consisting of Be rods in an Al matrix. A typical example is shown in the optical micrograph in Fig. 2 for the Al-4 wt% (11 at%) Be alloy. For this alloy, the volume fraction of Be was calculated to be 5.8%. When alloys containing increasing amounts of Be are rapidly solidified by Laser Surface Melting (LSM) and self-quenching, the microstructures show a transition from a cellular structure consisting of Al interspersed with linear arrays of cph Be precipitates to ones consisting predominantly of a uniformly refined dispersion of bcc Be particles in an Al matrix [9,34]. A typical example is shown in Fig. 3 for the Al-4Be alloy. The formation mechanism for these microstructures has been interpreted on the basis of undercooling prior to nucleation such that a metastable monotectic reaction occurs [9,34]. A metastable Al-Be phase diagram derived from the work of Murray [35] is shown in Fig. 4. The monotectic composition is approximately 2 wt% Be.

The thermal stability of the bcc Be dispersions in the Al-4Be alloy produced by LSM was investigated by following the changes in microhardness and microstructure for samples heat-treated at 400°C. Microhardness measurements showed a decrease with aging time, as shown in Fig. 4. Concurrently, the microstructure undergoes a transformation from bcc Be particles to cph Be prism-rods, a representative example of which is shown in the bright-field (BF) micrograph in Fig. 6a for the 8 hr treatment. To facilitate the crystallographic analyses of these prism-rods, a higher heat-treatment temperature (500°C for 1 hr) was employed to increase the prism-rod size. The microstructure following this treatment showed both the prism-rod morphology characteristic of the 400°C treatment and a second morphology consisting of blocky particles (Fig. 6b).

Several crystallographic orientations involving cph Be were observed in the heat-treated material and these are listed in Table 2. A total of 11 orientation relationships have been listed, and 8 of the 11 orientations were observed experimentally. Some of the orientation relationships (OR's) represent permutations of the symmetry elements of the other orientations. Experimental

8

evidence for these OR's is presented in the series of micrographs in Figs. 7 through 14. Each figure contains a bright-field/dark-field pair, an experimental diffraction pattern, and a computer simulation for the same electron beam direction. The large, medium, and small computed diffraction spots correspond to those arising from the matrix, precipitate, and double diffraction, respectively. The results show that OR's 1,2,3,4, and 7 produce the prism rods in the 400°C heat-treatments (Fig. 6a), and OR's 2,3, and 8 produce the more equiaxed and facetted particles observed after the higher temperature heat-treatments (Fig. 6b). A large number of variants of the 8 OR's were observed.

Calculations of the number of variants for each OR based on the method of Cahn and Kalonji [36] and determinations of the intersection point group and multiplicity show that 58 possible variations of the 8 OR's can occur in any one Al grain. For the prism-rod morphology alone, there are 36 possible variants, which explains the large number of orientations observed for this morphology (Fig. 6a). From calculations of the lattice mismatch between cph Be and Al [34] and the observable absence of a large strain contrast around the particles in the TEM micrographs, it appeared that lattice plane matching and strain energy effects [37] have little influence on the crystallography of the prism-rod Be particles.

Table 2

Crystallographic Orientations Between Al and cph Be

1.	$[100] \parallel [1\bar{2}10]$	$(010) \parallel (0001)$	$(100) \parallel (10\bar{1}0)$
2.	$[101] \parallel [1\bar{2}10]$	$(\bar{1}01) \parallel (10\bar{1}0)$	$(010) \parallel (000\bar{1})$
3.	$[10\bar{1}] \parallel [1\bar{2}10]$	$(\bar{1}01) \parallel (0001)$	$(010) \parallel (10\bar{1}0)$
4.	$[010] \parallel [1\bar{2}10]$	$(\bar{1}01) \parallel (0001)$	$(101) \parallel (\bar{1}010)$
5.	$[101] \parallel [1\bar{2}10]$	$(\bar{1}\bar{1}1) \parallel (0001)$	$(\bar{1}21) \parallel (10\bar{1}0)$
6.	$[101] \parallel [1\bar{1}00]$	$(\bar{1}\bar{1}1) \parallel (0001)$	$(\bar{1}21) \parallel (11\bar{2}0)$
7.	$[001] \parallel [1\bar{2}10]$	$(100) \parallel (10\bar{1}\bar{1})$	$(010) \parallel (10\bar{1}2)$
8.	$[101] \parallel [0001]$	$(\bar{1}\bar{1}1) \parallel (\bar{1}010)$	$(\bar{1}21) \parallel (1\bar{2}10)$
9.	$[101] \parallel [0001]$	$(\bar{1}\bar{1}1) \parallel (\bar{1}2\bar{1}0)$	$(\bar{1}21) \parallel (10\bar{1}0)$
10.	$[101] \parallel [10\bar{1}0]$	$(\bar{1}\bar{1}1) \parallel (1\bar{2}10)$	$(\bar{1}21) \parallel (0001)$
11.	$[101] \parallel [1\bar{2}10]$	$(\bar{1}\bar{1}1) \parallel (10\bar{1}0)$	$(\bar{1}21) \parallel (000\bar{1})$

In contrast to the LSM rapidly solidified alloys, melt spinning did not produce a uniform dispersion of Be particles. Instead, the microstructures exhibited a precursor reaction (Figs. 15a and 15b), which indicated that nucleation occurred in the L_1-L_2 phase field of Fig. 4, prior to the

9

monotectic reaction. To determine the mechanical properties, ribbon particulate was extruded at 375°C with an extrusion ratio of 18:1. Optical metallography indicated a fully dense product (Fig. 16). The hardness of the extrusion was 54 DPH. Thin foil examination of the extrusion revealed a dynamically recrystallized microstructure of Al grains (1-2 um) containing a coarse dispersion of Be particles (Figs. 17a and 17b).

3.1.2 Microstructures of Al-Mn Alloys

Al-1.1Mn and Al-7.5Mn-2Mo alloys were chill cast and a typical as-cast structure is shown in Fig. 18a for the latter alloy. The effect of solution treatment (630°C for 1 hr) followed by artificial aging (200°C for 96 hrs) of the Al-1.1Mn alloy was examined. The resultant microstructure exhibited some second phase precipitation, presumably of the Al_6Mn phase (Fig. 18b).

In an effort to determine the the response of Al-Mn alloys to RSP and subsequent consolidation, the Al-7.5Mn-2Mo alloy was melt spun; the resultant microstructures were cellular with intercellular regions composed of Mn rich particles (Fig. 19a). Heat-treatment of the melt-spun ribbons at 400°C produced coarse second phase particles (Fig. 19b) and analytical studies revealed that the Al matrix contained a substantial concentration of Mn [38].

3.1.3 Tensile Properties

Al-Be Alloys

The monotonic properties of the Al-4Be alloy, for both as-cast material and extruded melt-spun ribbons, is presented in Table 3. The extruded material showed significantly superior strength and ductility relative to the cast material; however, the elastic modulus was about the same. Fractography revealed that the failure mode for both materials was by void coalescence (Fig. 20).

Since the solubility of Be is less than 0.3 at %, the elastic modulus of the Al-Be composite should depend only on the volume fraction of Be. The calculated volume fraction of 5.8% for the Al-4Be alloy is low and, therefore, from the standpoint of elastic modulus, an optimal dispersion of small Be particles with a high aspect ratio is preferable. Thus, the morphology and size of the Be needles in LSM heat treated material (Fig.6a) should have provided good elastic constraint to the Al matrix. Unfortunately, the precursor reaction prevented formation of these unique microstructures in the melt-spun ribbon. As a consequence, the elevated temperatures experienced during extrusion produced a microstructure consisting of a coarse dispersion of Be

10

particles, free of the prism-rod morphology, and therefore provided virtually no improvements in the elastic modulus. The variation in the elastic modulus with Be content is shown in Fig. 21; the measured values are consistent with those calculated using the Hashin and Shtrikman formulation [7] for a dispersion of spherical particles. Significant improvements in the elastic modulus of Al alloys by composite alloying would require high Be concentrations.

Table 3

Monotonic Properties* of Al-Be Alloys

	Extruded Al-3.7Be	Cast Al-4.8Be
Elastic Modulus	71.5 GPa	74.4 GPa
Yield Strength	126 MPa	65 MPa
Ultimate Strength	163 MPa	127 MPa
Reduction in Area	83%	30%
True Fracture Strength	350 MPa	172 MPa
True Fracture Ductility	1.80	0.203
Strain Hardening Exponent	0.094	0.203
Strength Coefficient	224 MPa	230 MPa

* Values reported are the average of two samples

Al-Mn Alloys .

The variation in elastic modulus with Mn content for as-cast and solution treated (630°C for 1 hr) Al-Mn alloys is presented in Fig. 22. The results showed an increase in modulus of Al at a rate of 10 Gpa/at % Mn, which differs from that of 4.8 GPa/at % Mn reported elsewhere[2]. A rapid increase in modulus is predicted by Leigh's model [1] and the present results are consistent with this. Aging (200°C for 96 hrs) the solution-treated Al-1.1Mn alloy resuled in a drop in modulus (Fig. 22); this effect is presumably associated with the precipitation of the Al_6Mn phase (Fig 18b). However, the volume fraction of the second phase was lower than the calculated value of 4% for the 1.1Mn composition. Therefore, the discrepencies in modulus data are probably associated with the unreported presence of these precipitates.

Since the elastic constants for the Al_6Mn intermetallic are not available, the data of Dudzinski [3-5] was modelled (Fig. 23) on the basis of the Hashin and Shtrikman formulation [7] to yield values of 150 Gpa and 0.25 for the elastic modulus and Poisson's ratio, respectively.

11

Application of these results to the Al-1.1Mn alloy predicted values for the elastic modulus which are in good agreement with that measured for the artificially aged alloy. (For example, the measured modulus of 68.3 GPa is within the calculated upper and lower bounds of 68.5 and 68.1 GPa, respectively). In addition, the results showed that the increase in modulus of Al-Mn alloys is associated primarily with solid solution effects.

The elastic modulus of the cast Al-7.5Mn-2Mo alloy fell outside the Hashin and Shtrikman [7] bounds (Fig. 23). The low value of the elastic modulus in this material was associated with casting porosity. Brittle fracture of this cast alloy occurred which was attributed to the presence of large intermetallic particles [38].

3.1.4 Fatigue Properties

The fatigue strength of the Al-4Be extruded ribbon was evaluated and the results for ten samples are summarized in Table 4. Three of the ten samples were subjected to a 500°C, 1 hr heat-treatment. The microstructure following this treatment consisted of coarse Be particles in an Al matrix; the prism-rod morphology characteristic of the LSM material was absent. The failure criteria, which was based on a 10% load drop, produced a crack size of 2.2 mm (Fig. 24a). Crack initiation occurred at a surface indentation caused by the knife edge of the strain guage (Fig. 24b) . However, the presence of such a notch had little influence on the short term fatigue

Table 4

Fatigue Life Data of Al-3.7Be Extruded Ribbon

Specimen No.	$\Delta\varepsilon/2$	$\Delta\sigma/2$ (MPa)	N_f
1	0.004	112	620
2*	0.006	86	980
3	0.006	126	321
4	0.002	99.5	6,950
6	0.0015	88	48,900
7	0.00072	50	5×10^6
8	0.001	70	836,000
9*	0.00072	50	775,000
10*	0.001	70	372,000

* After heat treatment

12

life. Fatigue striations were of the order of the grain size, and crack branching was evident (Fig. 24c). The fatigue properties of the Al-4Be alloy correspond to that of an intermediate Al alloy as seen in Fig. 25, where the data are compared with those of the 1100-T6 and 7075-T6 Al alloys.

Fig. 2. Light-optical micrograph of an as-cast Al-4Be alloy.
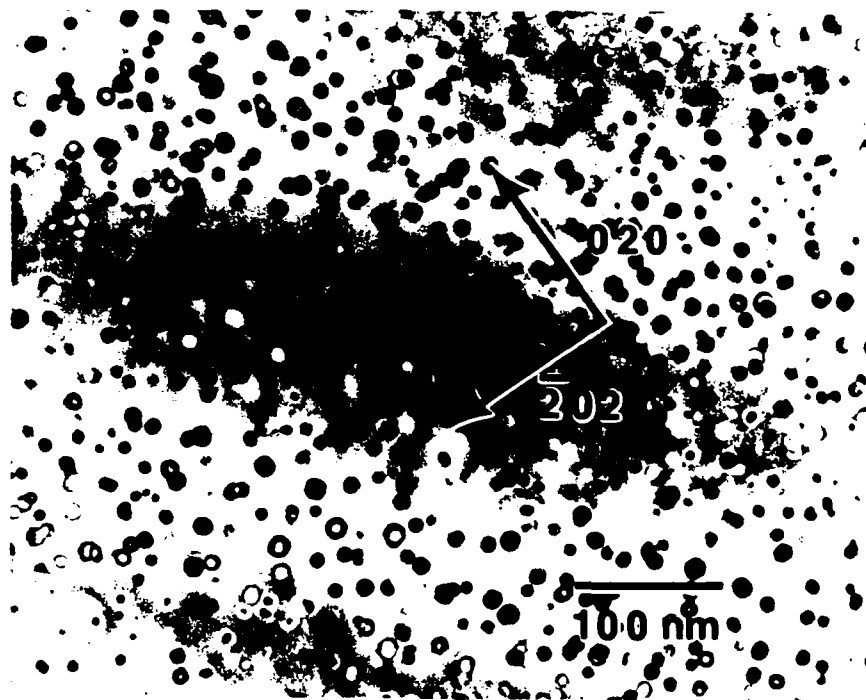
Fig. 3. BF micrograph of the LSM Al-4Be filament showing a uniform distribution of Be particles in an Al matrix.
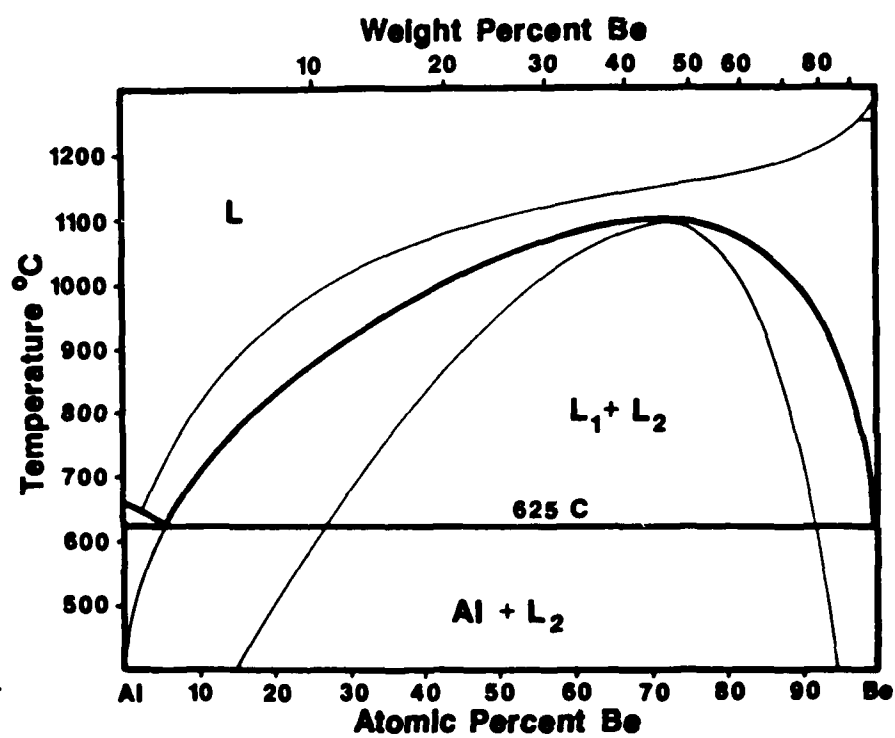
Fig. 4.   Metastable phase diagram for the Al-Be system.
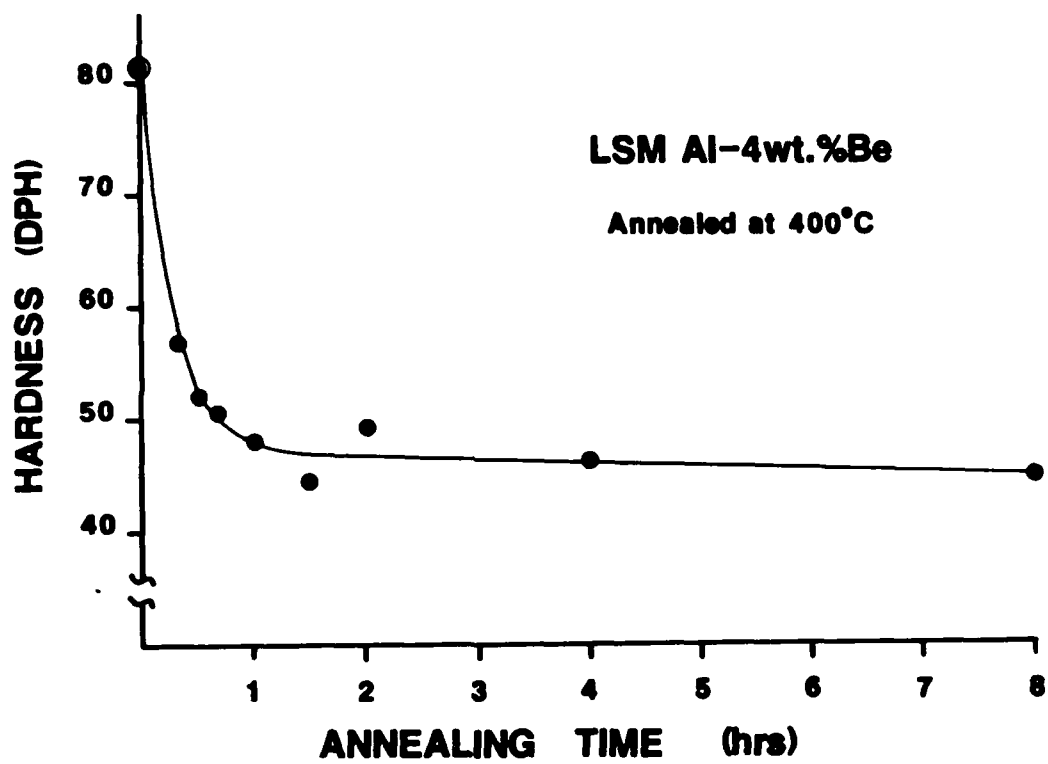
Fig. 5. Variation of microhardness with aging time at 400°C for the LSM Al-4Be alloy.

Fig. 6. BF micrographs showing examples of the prism-rod morphology of Be particles produced by heat-treating the LSM Al-4Be filament at a) 400° for 8 hrs and b) 500°C for 1 hr; the latter also shows Be particles with an equiaxed shape.
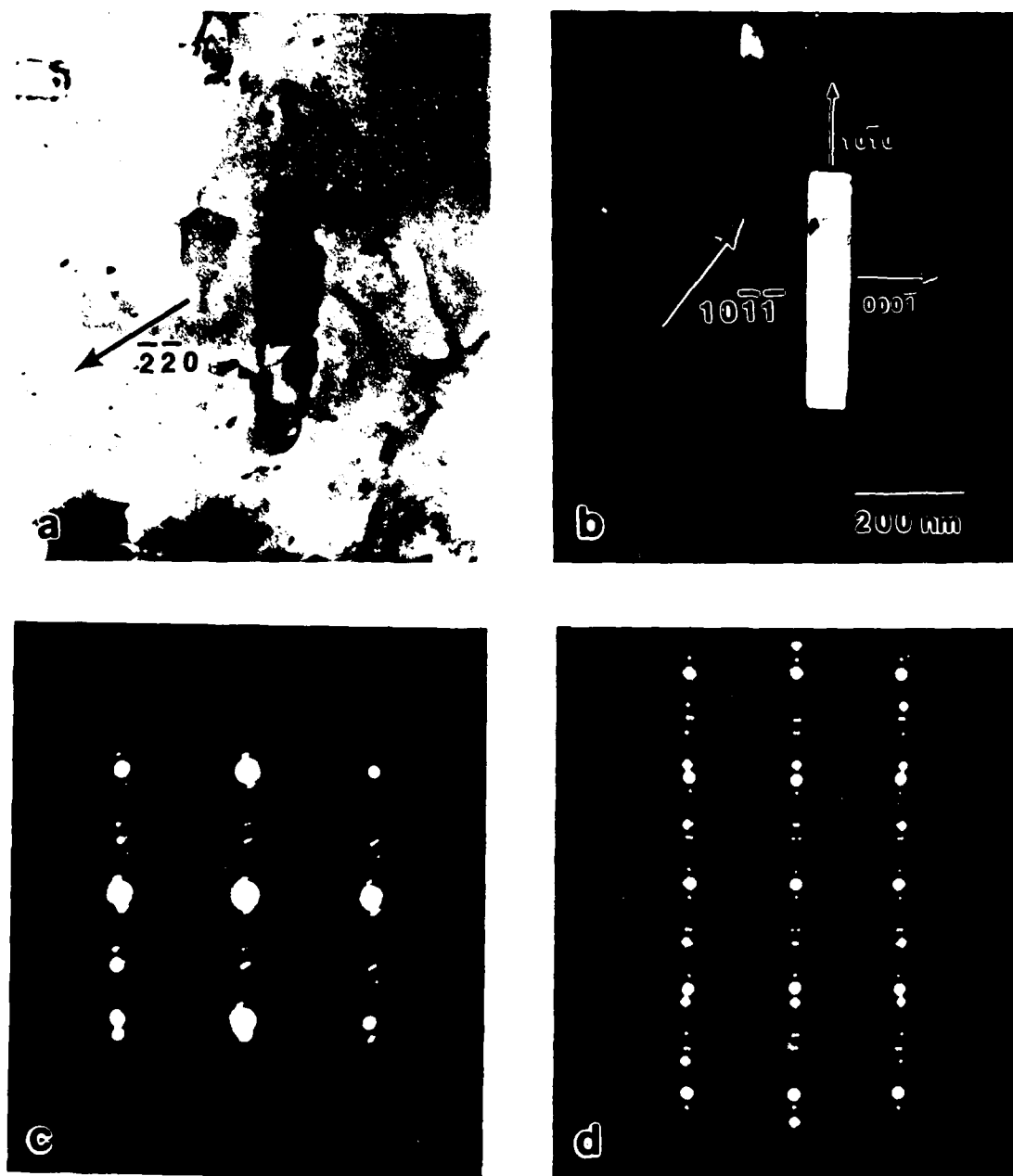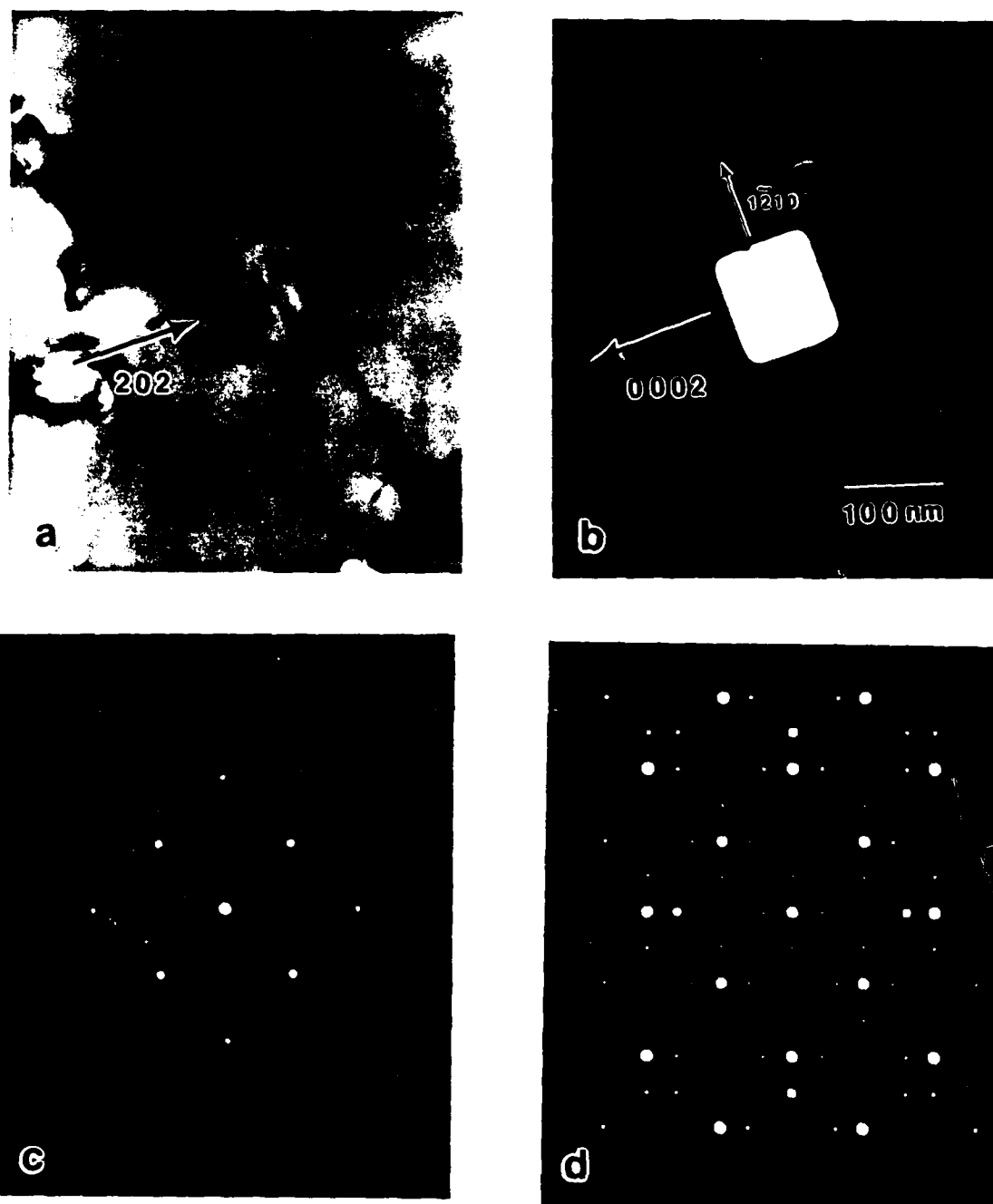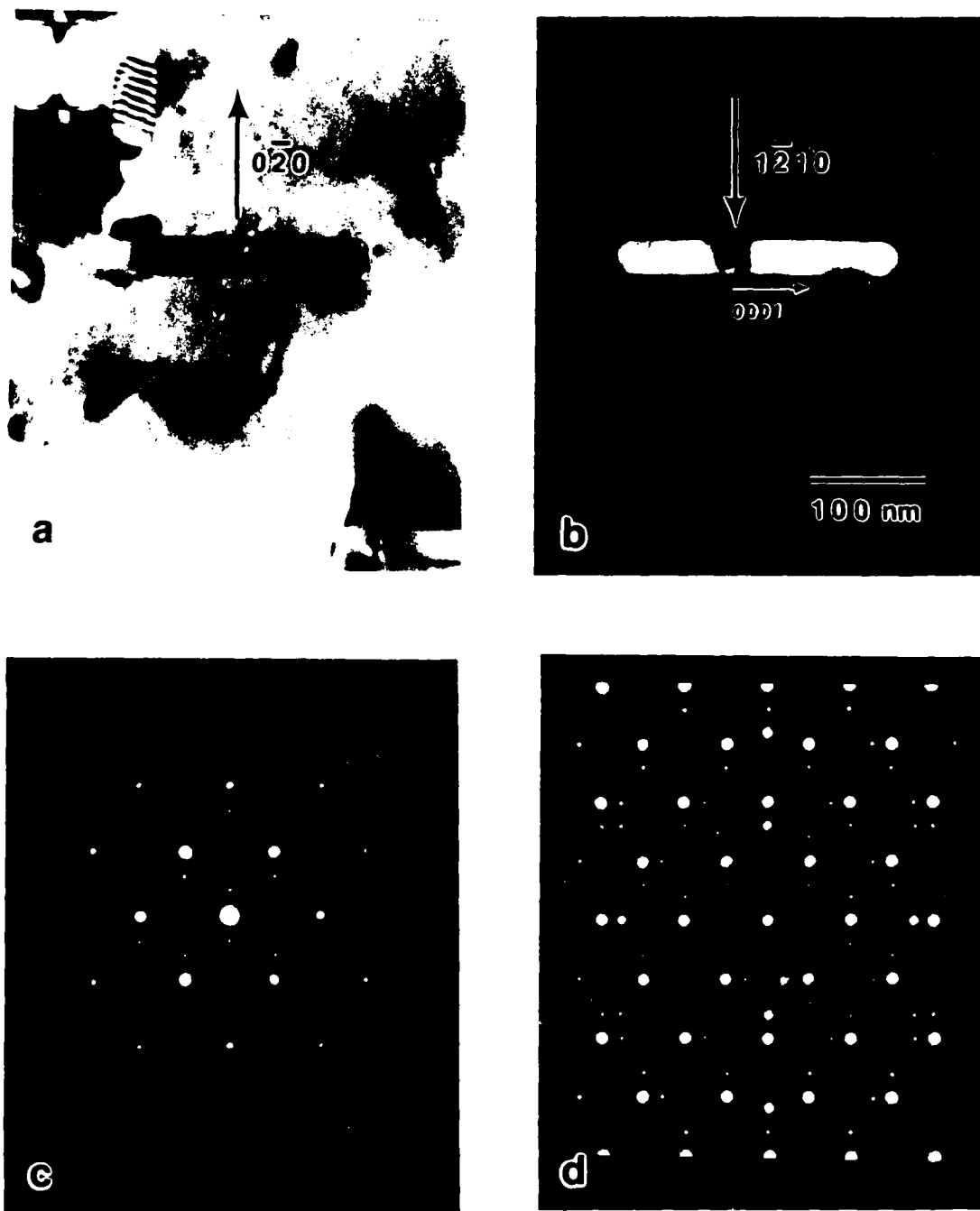
Fig. 7. Experimental data for orientation relationship #1. The intersection point group is mmm and an orthorhombic crystal type is expected. Experimental data (a-d) and (e-h) show two orthogonal views of two different cph Be particles which were identified with this OR. Facets were identified on the dark field image. The prism-rod shape is consistent with the intersection point group. (a-d) $\mathbf{B} = [001]_{Al} \parallel [1\bar{2}10]_{Be}$. (e-h) $\mathbf{B} = [010]_{Al} \parallel [0001]_{Be}$. (d and h) simulated diffraction patterns for the given orientation.

19
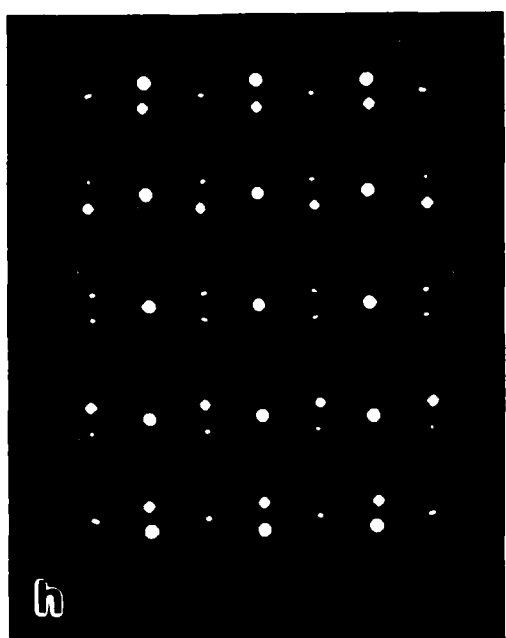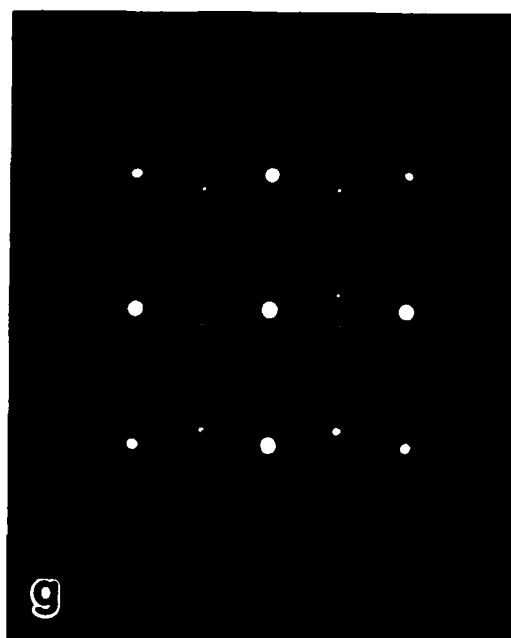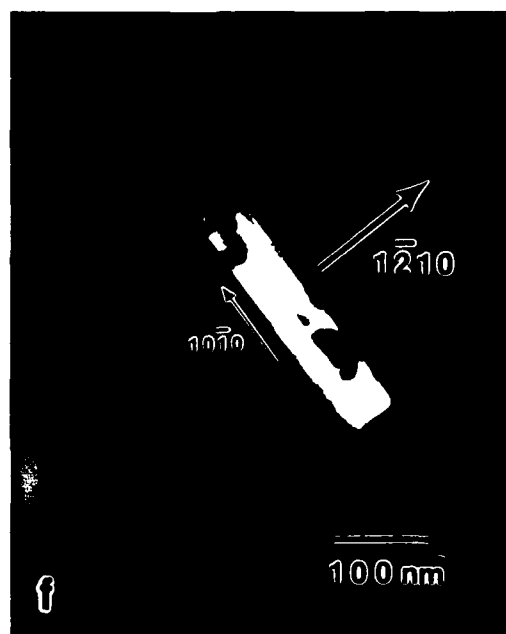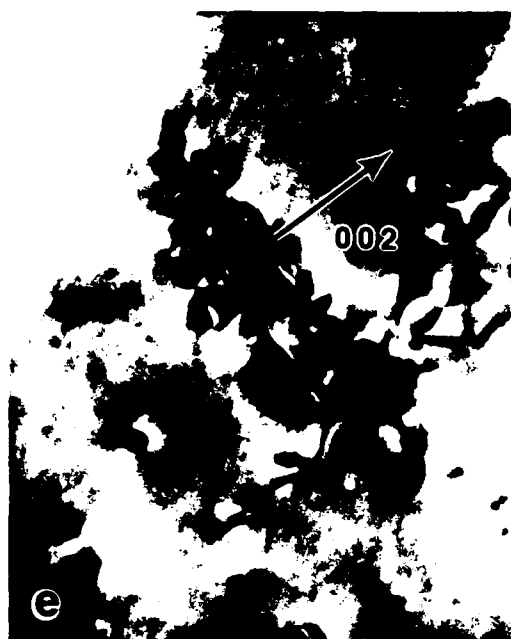
Fig. 7. (Continued).
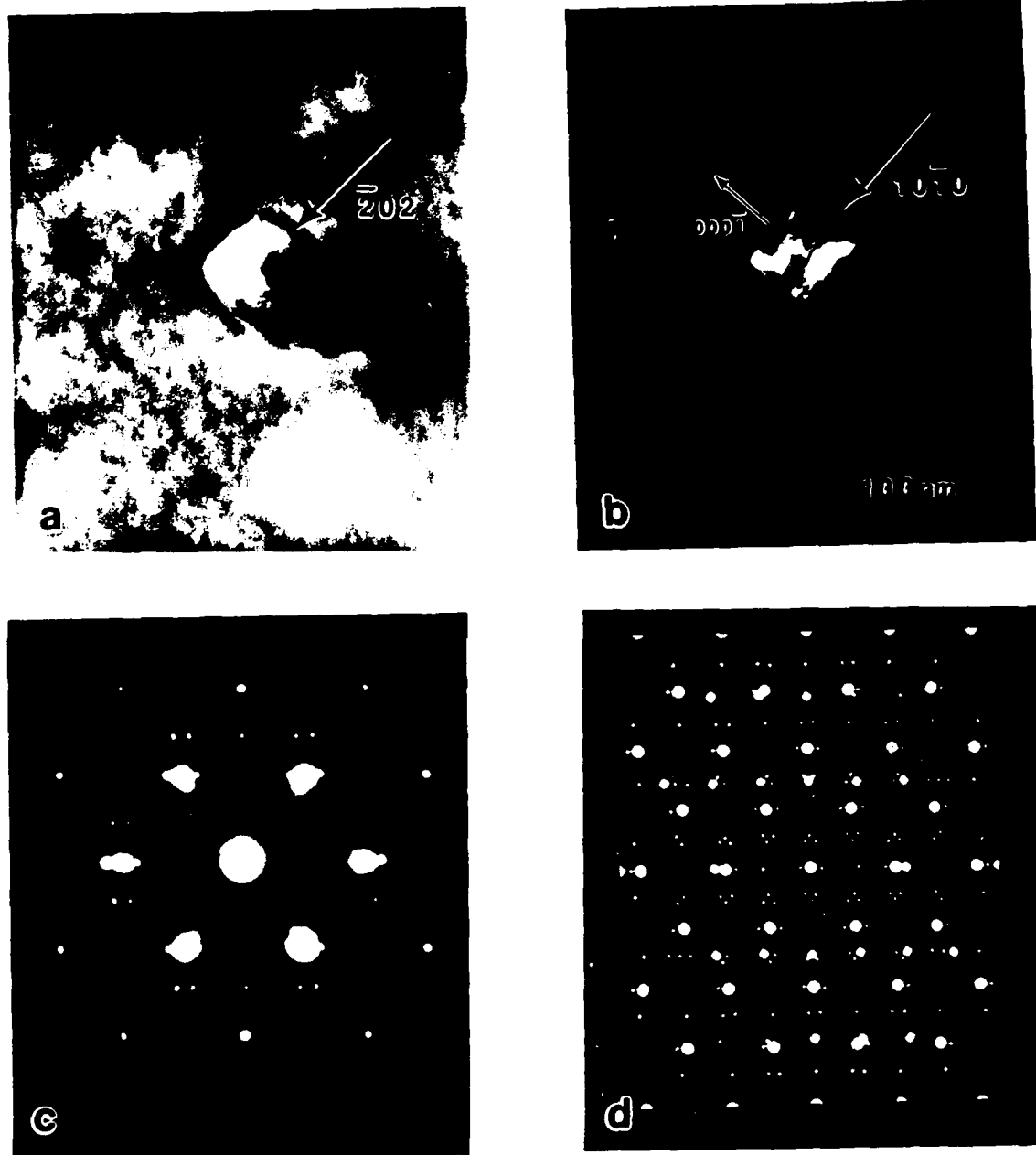
Fig. 8. Experimental data for orientation relationship #2. The intersection point group is mmm and an orthorhombic crystal type is expected. Experimental data (a-d) and (e-h) show two orthogonal views of two different cph Be particles which were identified with this OR. Facets were identified on the dark field image. The prism-rod shape is consistent with the intersection point group. (a-d) $\underline{B} = [101]_{Al} \parallel [1\bar{2}10]_{Be}$. (e-h) $\underline{B} = [010]_{Al} \parallel [000\bar{1}]_{Be}$. (d and h) simulated diffraction patterns for the given orientation.

21
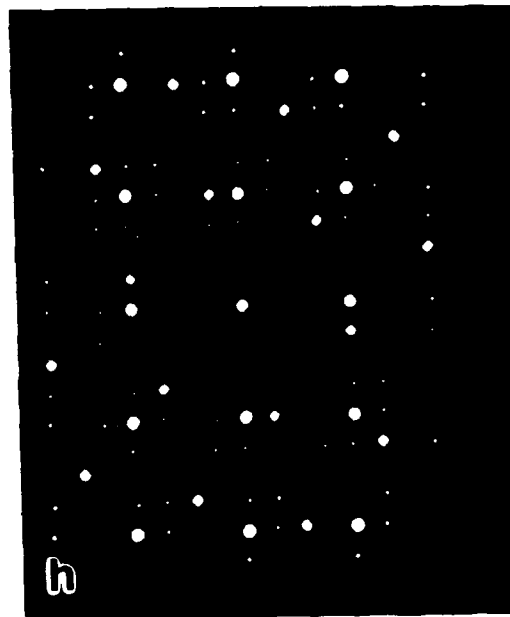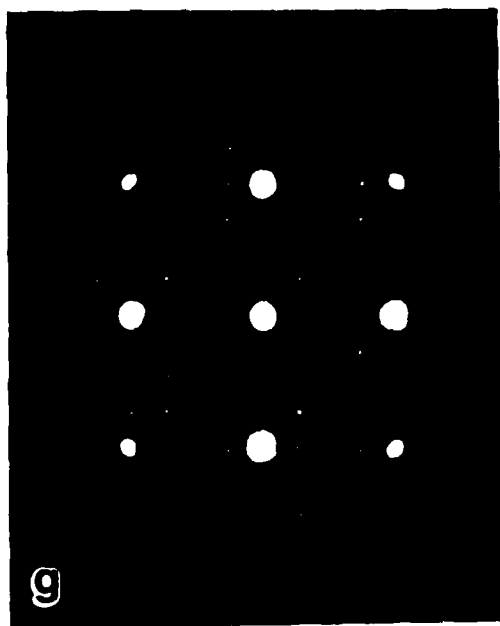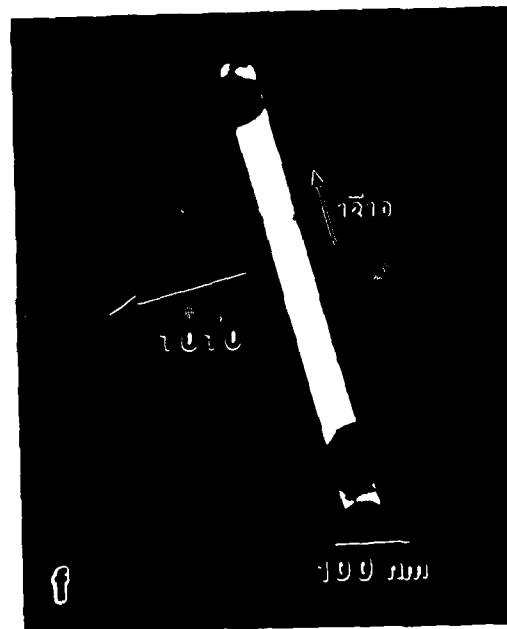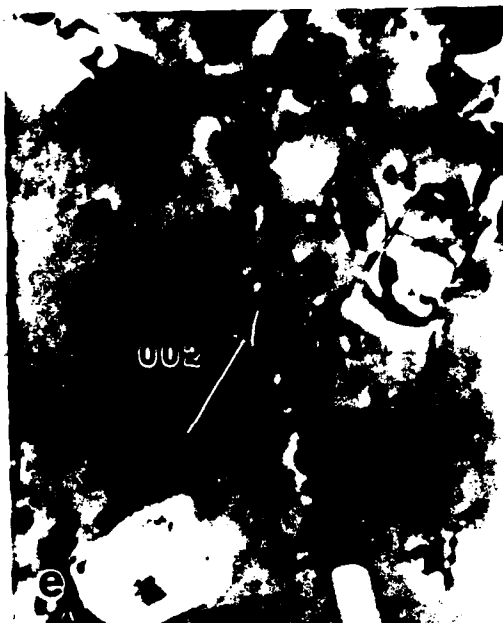
Fig. 8. (Continued).

Fig. 9. (a-d) Experimental data for orientation relationship #3. The intersection point group is mmm and an orthorhombic crystal type is expected. Facets were identified on the dark field image. The prism shape is consistent with the intersection point group. (d) Simulated diffraction pattern with $\underline{B} = [010]_{Al} \parallel [10\bar{1}0]_{Be}$ for the given OR.
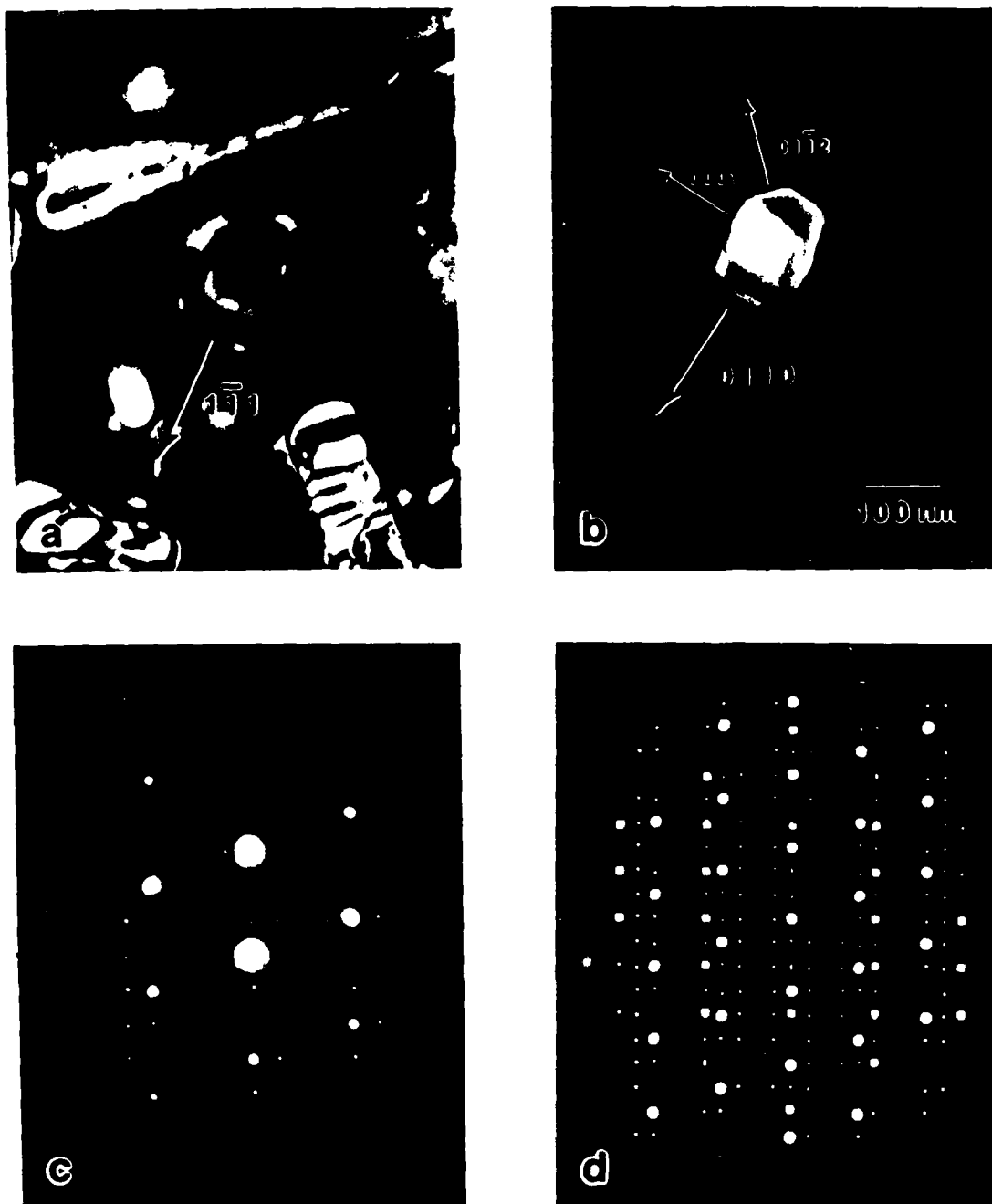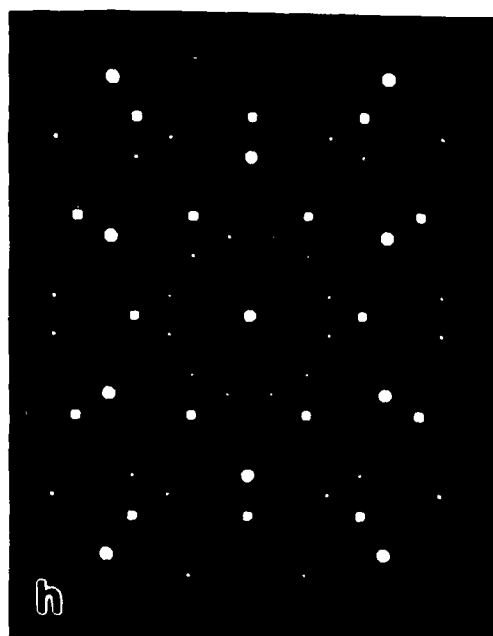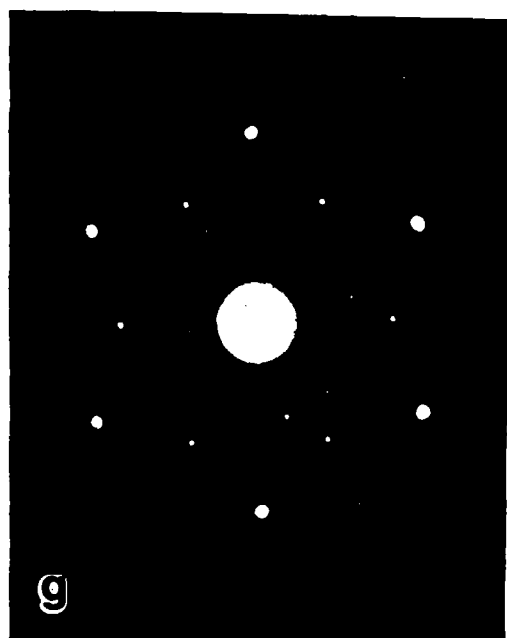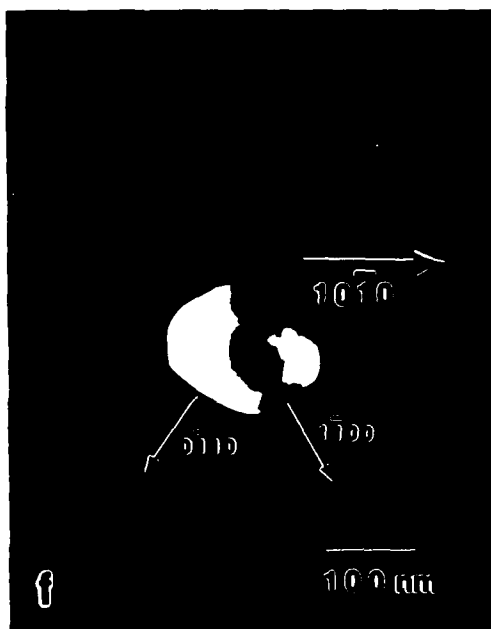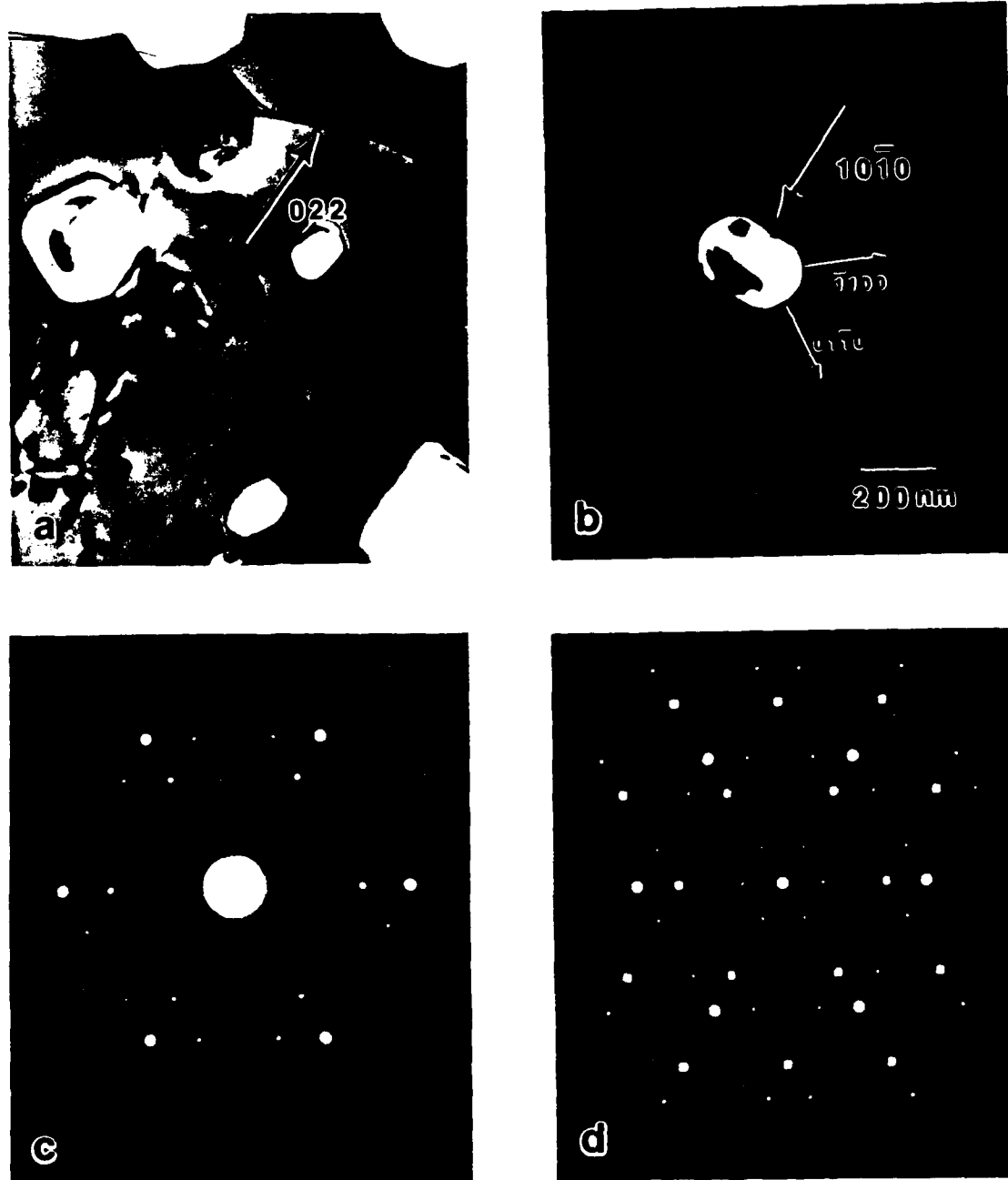
Fig. 10. (a-d) Experimental data for orientation relationship #4. The intersection point group is mmm and an orthorhombic crystal type is expected. Facets were identified on the dark field image. The prism-rod shape is consistent with the intersection point group. (d) Simulated diffraction pattern with $\underline{B} = [\bar{1}0\bar{1}]_{Al} \parallel [10\bar{1}0]_{Bc}$ for the given OR.

24

Fig. 11. (a-d) Experimental data for orientation relationship #5. The intersection point group is 3m and a trigonal crystal type is expected. Experimental data (a-d) and (e-h) show two orthogonal views of two different cph Be particles which were identified with this OR. Facets were identified on the dark field image. The exact crystal shape could not be determined from the available data. (a-d) $\underline{B} = [10\bar{1}]_{Al} \parallel [1\bar{2}10]_{Be}$. (e-h) $\underline{B} = [\bar{1}\bar{1}1]_{Al} \parallel [0001]_{Be}$. (d and h) simulated diffraction patterns for the given orientation.

25

Fig. 11. (Continued).

26

Fig. 12. (a-d) Experimental data for orientation relationship #6. The intersection point group is 3m and a trigonal crystal type is expected. Facets were identified on the dark field image. The exact crystal shape could not be identified from the available data. (d) Simulated diffraction pattern with $\underline{B} = [\bar{1}\bar{1}1]_{Al} \parallel [0001]_{Be}$ for the given OR.
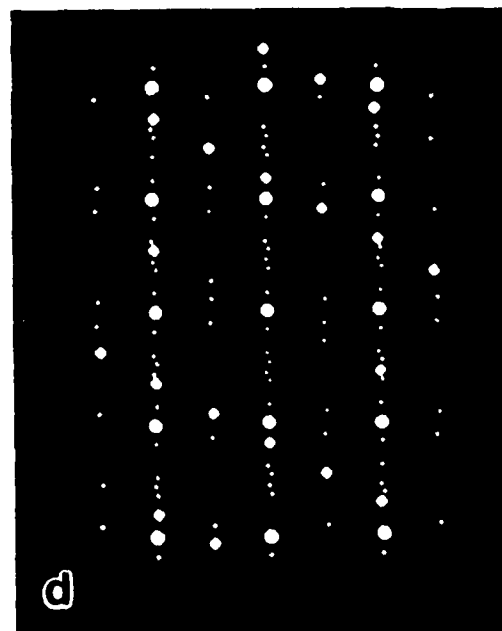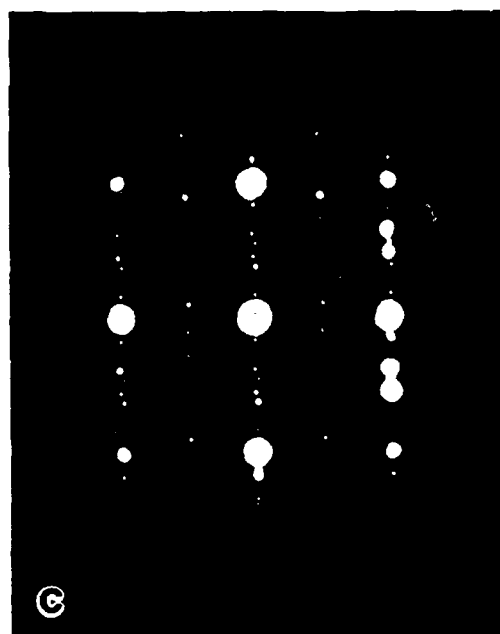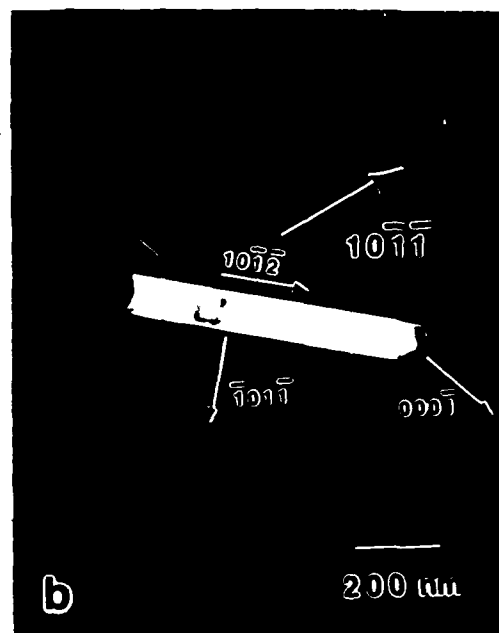
Fig. 13. (a-d) Experimental data for orientation relationship #7. The intersection point group is 2/m and a monoclinic crystal type is expected. Facets were identified on the dark field image. The exact crystal shape could not be identified from the available data; however, a prism-rod is suggested with a mirror axis perpendicular to the rod. (d) Simulated diffraction pattern with $\underline{B} = [001]_{Al} \parallel [1\bar{2}10]_{Be}$ for the given OR.
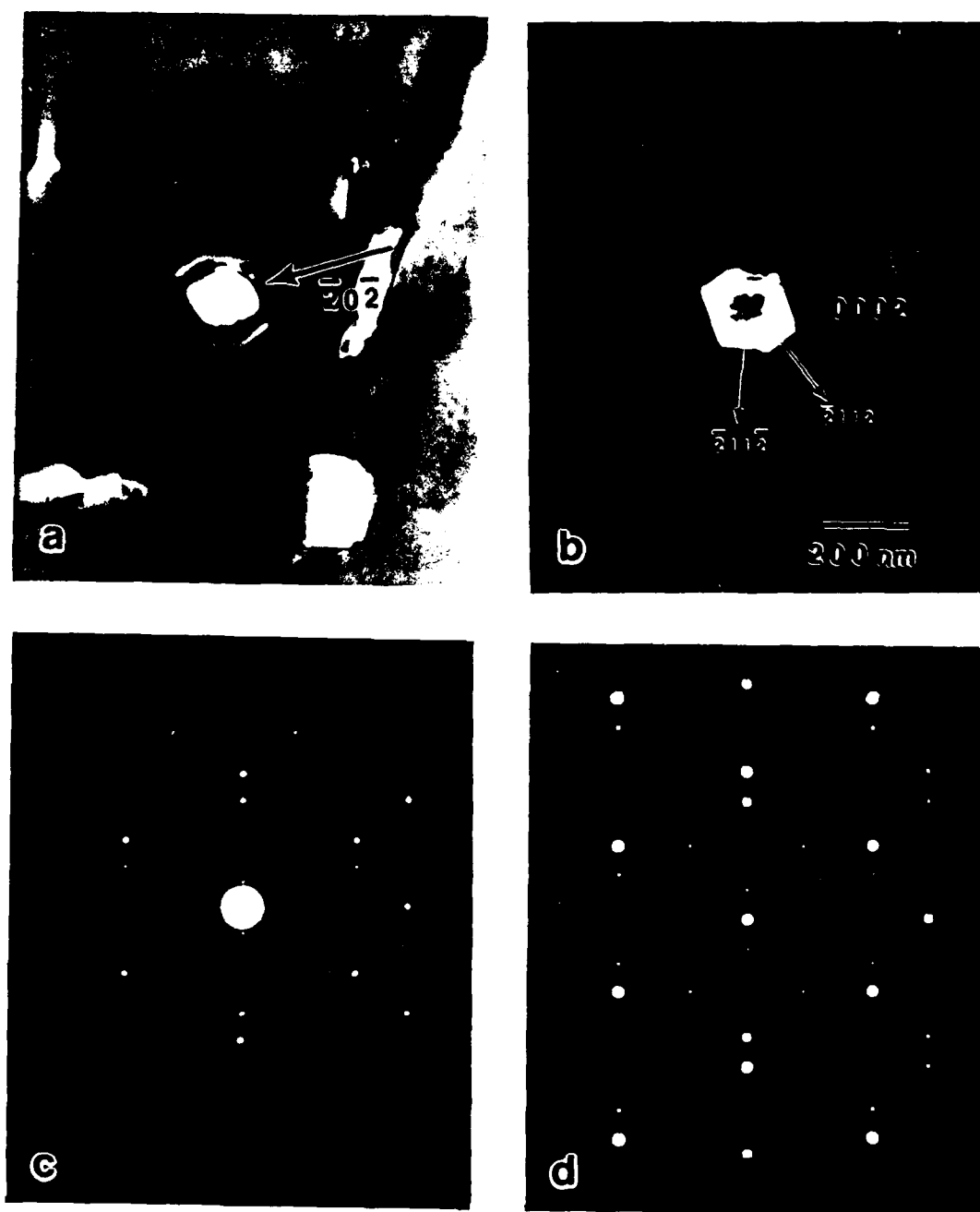
Fig. 14. (a-d) Experimental data for orientation relationship #8. The intersection point group is 2/m and a monoclinic crystal type is expected. Facets were identified on the dark field image. The exact crystal shape could not be identified from the available data: (d) Simulated diffraction pattern with $\underline{B} = [\bar{1}\bar{1}1]_{Al} \parallel [\bar{1}010]_{Be}$ for the given OR.
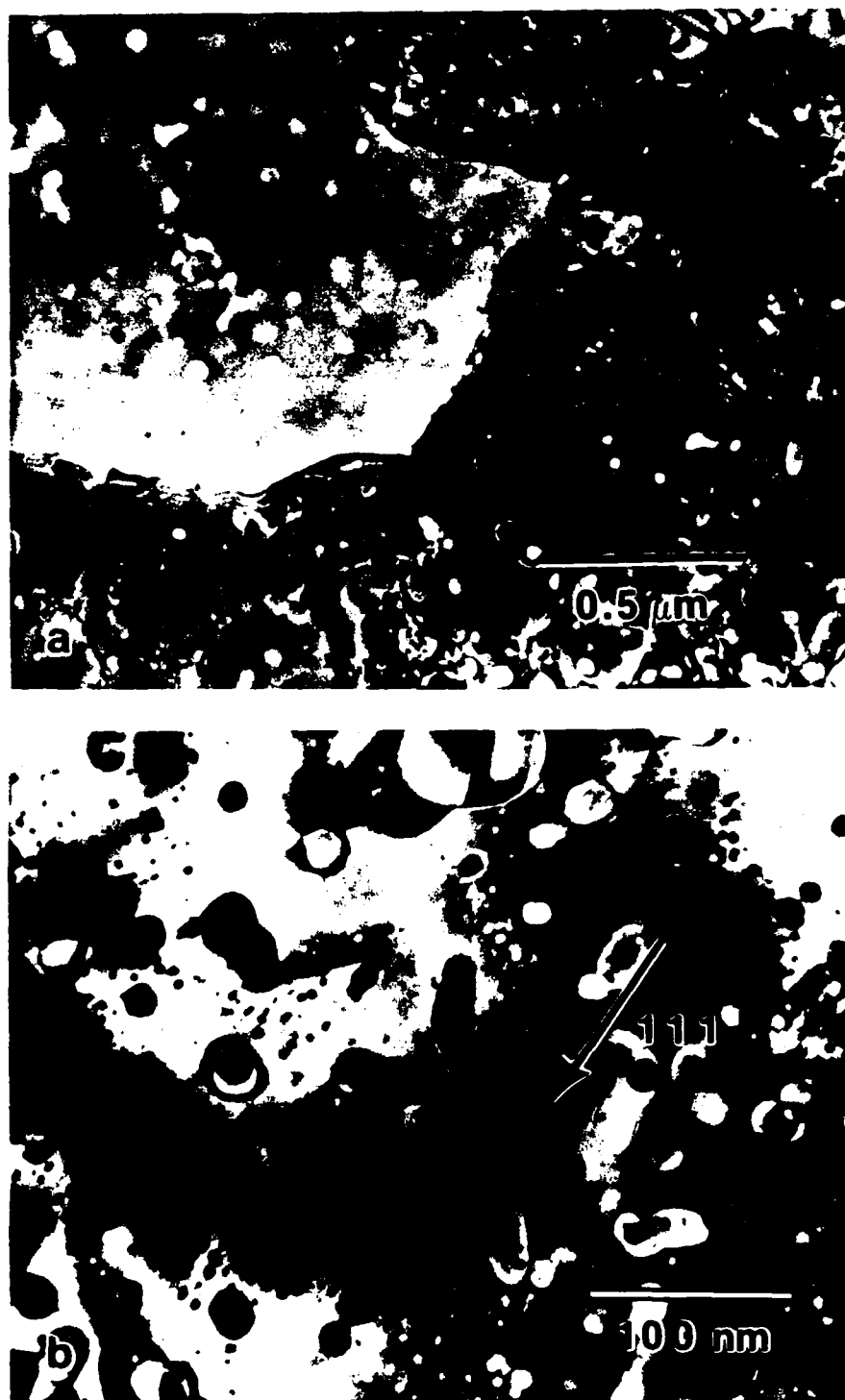
Fig. 15. BF micrographs (a and b) of the melt-spun Al-4Be alloy showing the presence of both
coarse particles resulting from the pro-monotectic reaction involving a liquid phase
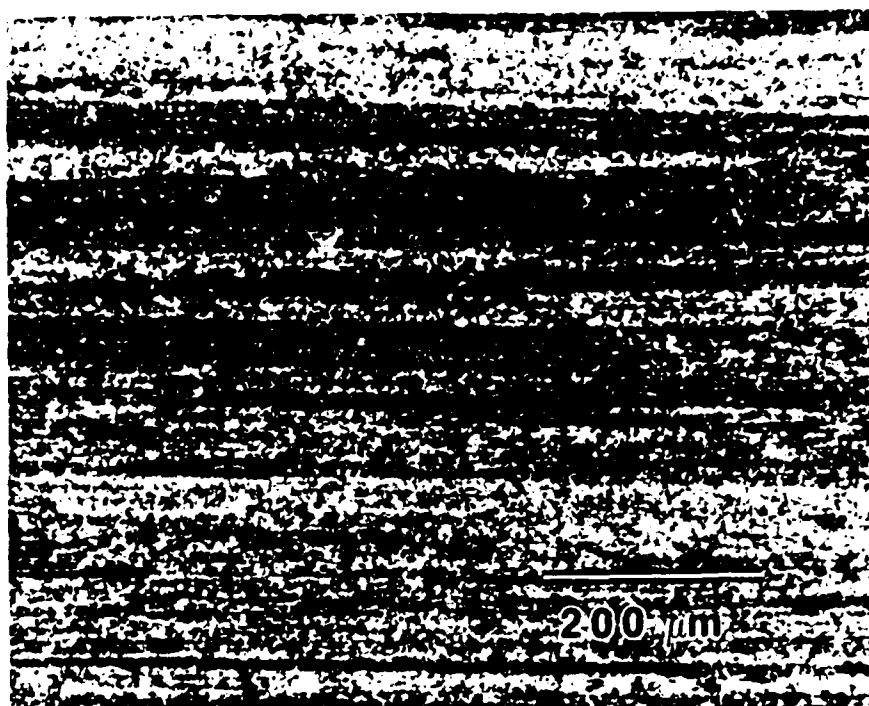separation and fine particles resulting from the monotectic reaction.

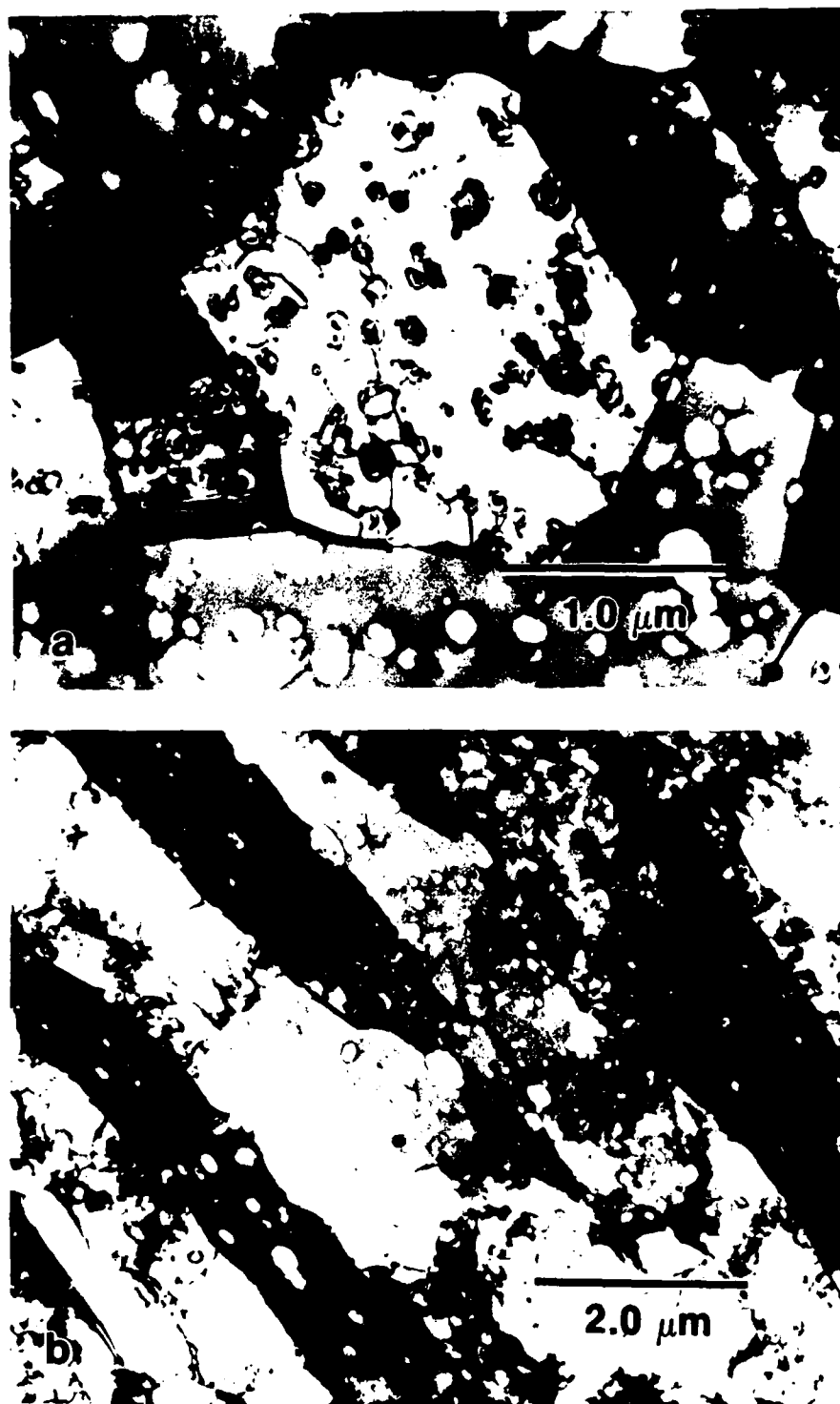Fig. 16. Light-optical micrograph (longitudinal cross-section) of the Al-4Be extruded ribbon.

Fig. 17. BF micrographs from a) Transverse and b) Longitudinal cross-sections of the extruded Al-4Be ribbon.
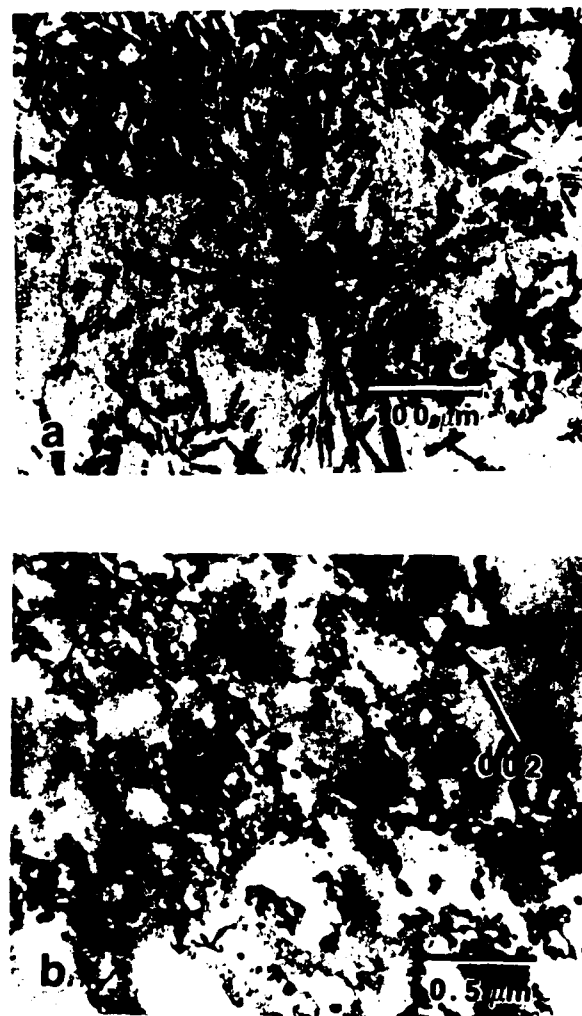
Fig. 18. a) Light-optical micrograph of a cast Al-7.5Mn-2.0Mo alloy; b) BF micrograph of the solution-treated and aged Al-1.1Mn alloy showing a low volume fraction of Mn-rich precipitates.
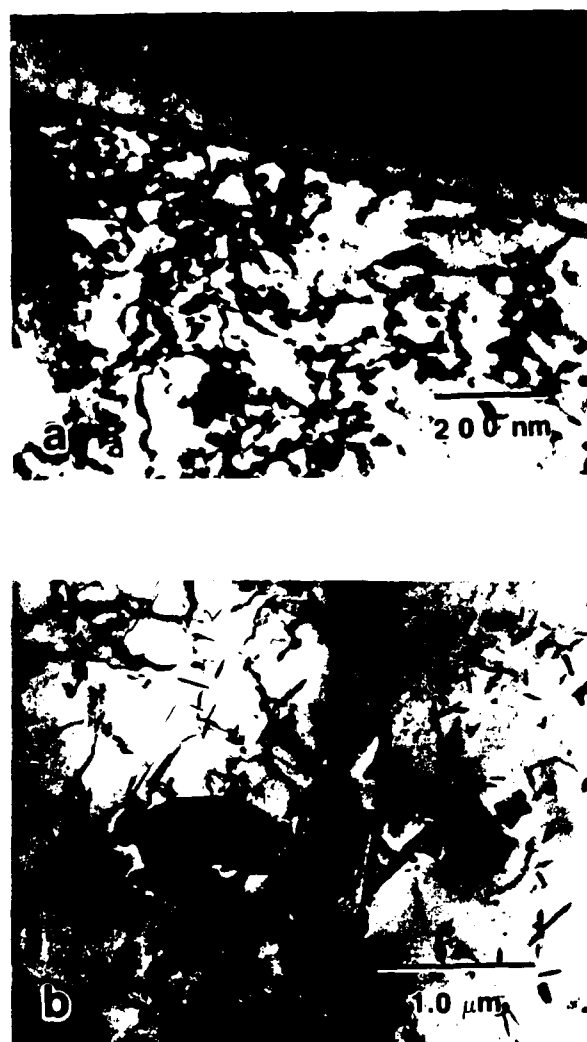
Fig. 19. BF micrographs of Al-7.5Mn-2.0Mo alloy. a) As-melt spun; b) Aged at 400°C for 1 hr.
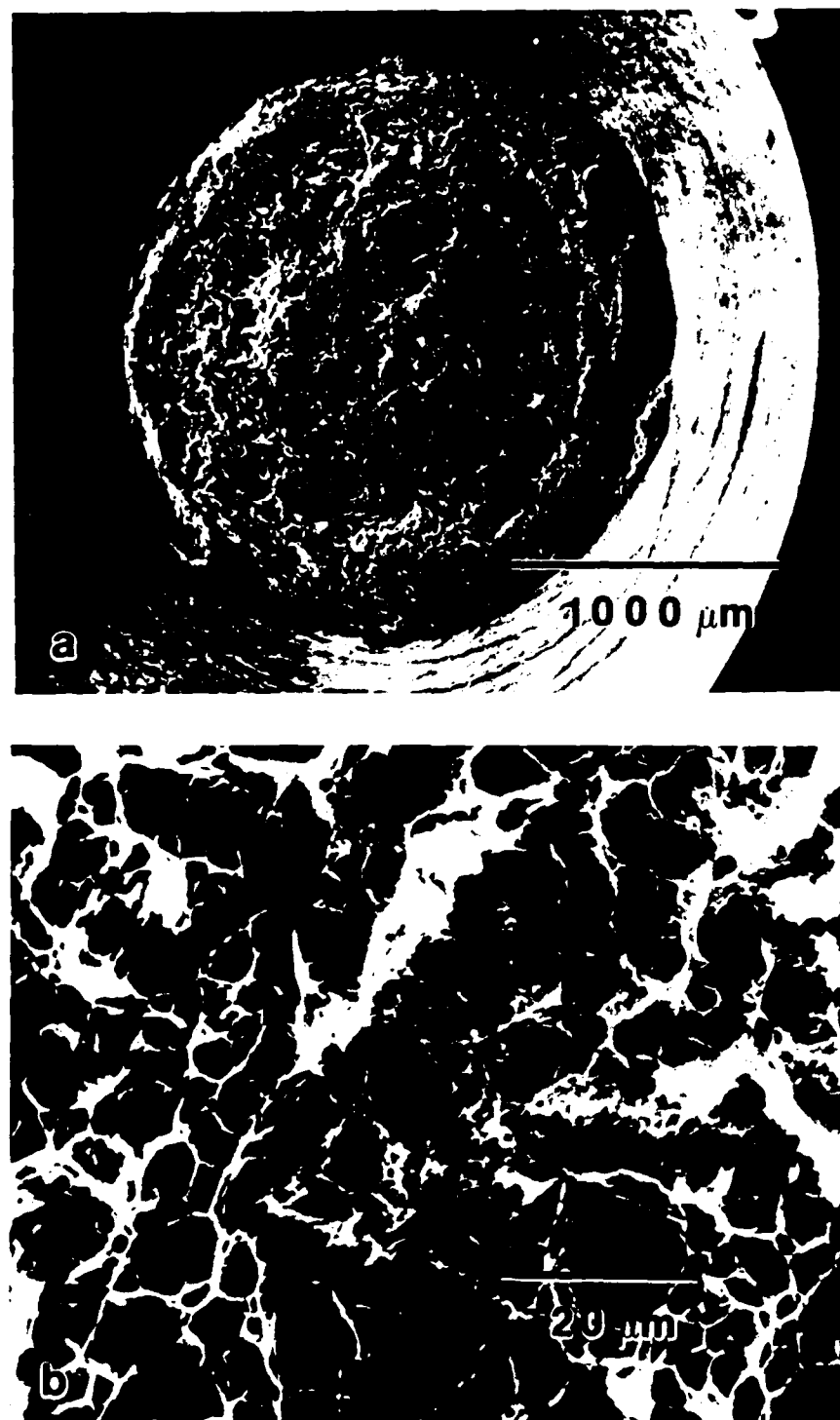
Fig. 20   SEM micrographs of a failed monotonic test specimen of the extruded Al-4Be ribbon. a)
Low magnification showing ductile fracture; b) High magnification showing failure
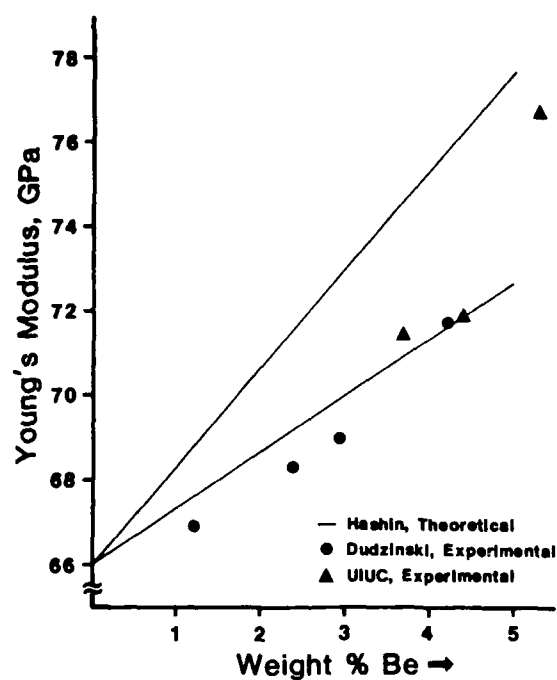mechanism by microvoid coalescence.

35

Fig. 21. Variation of elastic (Young's) modulus with Be content. Theoretical bounds were calculated for a two-phase microstructure of Al and Be using modulus and Poisson's ratio values of 66 GPa and 0.33, respectively, for Al and 293 GPa and 0.039, respectively, for Be.
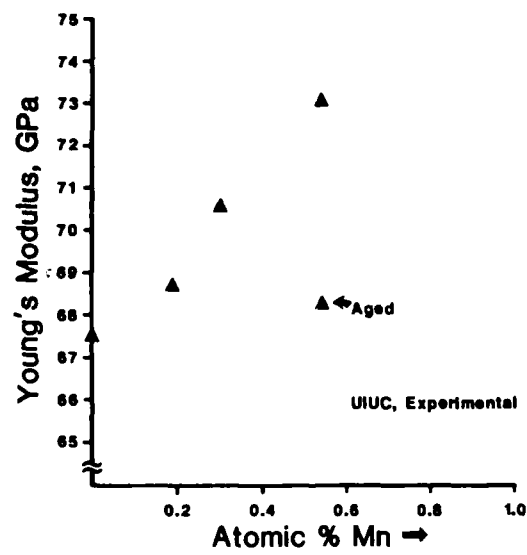
Fig. 22   Variation of elastic (Young's) modulus with Mn content. Alloys were solution-treated at 630°C and quenched prior to testing.
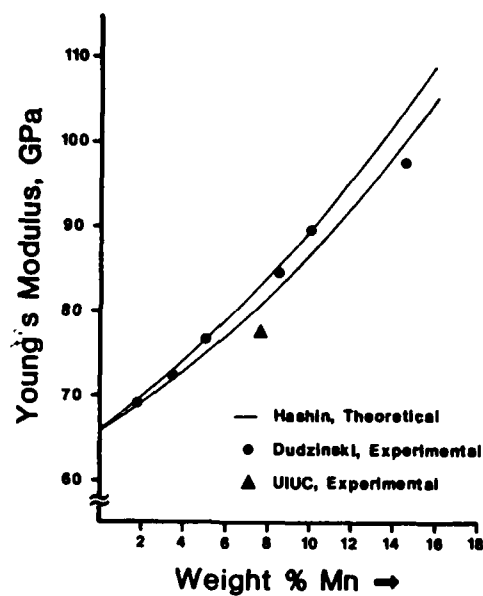
37

Fig. 23. Variation of elastic modulus with Mn content. Theoretical bounds were calculated for a two-phase microstructure of Al and Al_6Mn using modulus and Poisson's ratio values of 66 GPa and 0.33, respectively, for Al and 150 GPa and 0.25 (determined by a best fit to Dudzinski's data), respectively, for Al_6Mn.

38
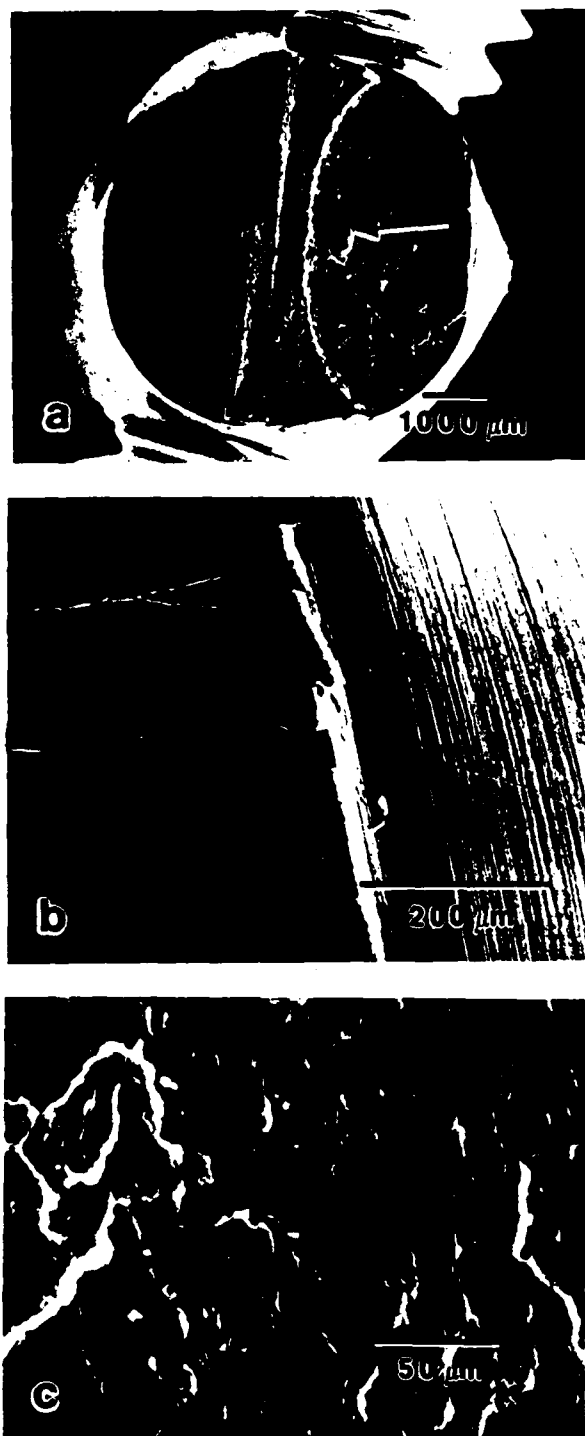
Fig. 24. SEM micrographs of fatigue-tested specimens of extruded Al-4Be ribbon showing a)
Fatigue crack in specimen #3 exposed by cutting the backside of the guage section,
relative to the crack, and fracturing the remaining portion of the material; b) Crack
initiation site in specimen #4, and c) Fatigue striations in region indicated by arrow in
"a".

39

Fig. 25. Strain amplitude versus cycles to failure for the extruded Al-4Be alloy ribbon. Heat-treated specimens were aged at 500°C for 1 hr. Data for 1100-T6 and 7075-T6 Al alloys are also shown.

40

3.2 Al-8Fe-2Mo Alloys

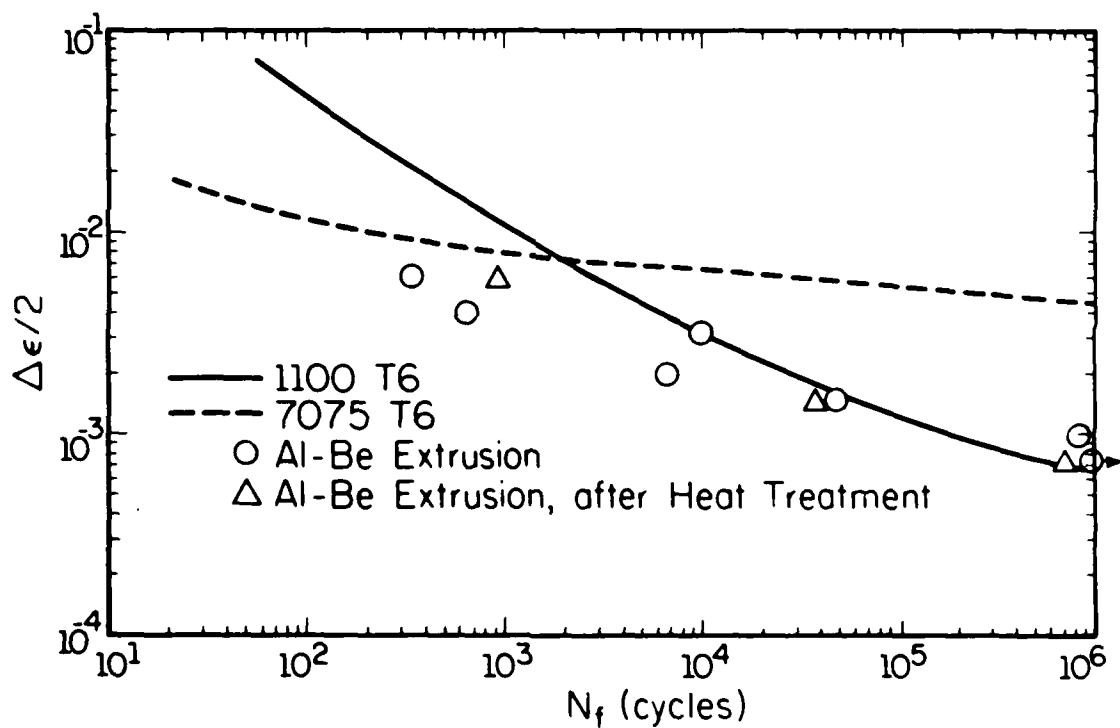The effect of Si additions on the microstructure of Al-8Fe-2Mo alloys was investigated. Al-8Fe-2Mo and Al-8Fe-2Mo-0.5Si alloys were induction melted, chill cast and then rapidly solidified into ribbons by melt spinning. The thickness of the ribbons varied from 25 to 45 mm. The microstructures of these alloys are described in the following.

3.2.1 As-Rapidly Solidified Structure

Optical microscopy revealed that, even for relatively thick ribbon, the microstructures of both alloys were completely Zone A. Thin foil TEM examination revealed a cellular-dendritic structure, similar to those in earlier reports [15]; the cell spacing was somewhat more uniform and finer (20 nm) in the Si-bearing alloy (Fig. 26a). Selected area diffraction (SAD) patterns (Fig. 26b) showed that besides the α-Al reflections, additional weak rings of intensity having d-spacings identical to those reported [15,17] for the quasi-crystalline intercellular T' phase in the Al-8Fe-2Mo alloy were also present. Microhardness measurements indicated that the Si-bearing alloy was significantly harder (355 KHN) compared to the Si-free alloy (270 KHN). This difference is probably associated with the finer grain and cell size of the Si-bearing alloy.

3.2.2 Microstructural Changes During Heat Treatment

The microstructural changes in the ribbons of both alloys, induced by heat treatment at 450°C for times ranging from 0.25 to 100 hours, were followed by TEM examination and are described below.

Al-8Fe-2Mo Alloy

Within 0.25 hrs, precipitation occurred at grain boundaries (Fig. 25a). Two types of precipitates, the $Al_6(FeMo)$ phase [12,39,40] and a bcc phase having a lattice parameter of 1.273 ± 0.01 nm, were identified; the latter phase being observed more commonly. A SAD pattern from the grain boundary precipitate indicated by the arrow in Fig. 27a is shown in Fig. 27b. This and other patterns could be indexed consistently on the basis of a bcc lattice. Further evidence for this phase is presented later. EDS analyses indicated that the bcc phase was based on Al and contained significantly larger amounts of Fe compared to Mo. The precise stoichiometry has not been determined as yet, but is tentatively described as $Al_p(FeMo)$. Generally, other than a slight coarsening of the intercellular phase, the intragrain structure showed little or no change in most

41

areas of the microstructure. However, thicker portions of the ribbon showed more decomposition, as seen in the examples in Fig. 28. The grain boundary precipitates labelled P in Figs. 28a and 28c were once again identified as the bcc $Al_p(FeMo)$ phase (see respective SAD patterns in Figs. 28b and 28d). On occasion, the bcc phase was also observed as facetted particles within grains.

Further aging to 4 hrs led to additional precipitation of the $Al_6(FeMo)$ and $Al_p(FeMo)$ phases, together with transformation of the intragrain structure to needles of the orthorhombic θ' Al_3Fe phase [39,40]. Representative examples are shown in Figs. 29a and 29b. The precipitate labelled A in Fig. 29b was identified as $Al_6(FeMo)$ (see SAD pattern in Fig. 29c). The precipitate labelled B was identified as the bcc $Al_p(FeMo)$ phase. A [001] SAD pattern taken from this precipitate is shown in Fig. 29d. The bcc Bravais lattice for this phase was established by convergent beam electron diffraction (CBED). Patterns taken of the ZOLZ and the FOLZ are shown in Figs. 30a and 30b, respectively. For a bcc lattice, the ratio of the spacings of the ZOLZ and FOLZ is equal to $\sqrt{2}$ [41]. Measurements of these spacings from the patterns in Figs. 299d and 30b gave $d_{FOLZ}/d_{ZOLZ} = 12.73/9.02 = 1.41 = \sqrt{2}$, which establishes the bcc nature of the lattice. Additional examples of diffraction patterns recorded from similar precipitates in other areas of the microstructure are shown in Figs. 31a-c.

On continued aging to 50 hrs, the orthorhombic θ' Al_3Fe needles progressively disappeared; the microstructure at this stage consisted of a dispersion of rather coarse precipitates of the $Al_6(FeMo)$, $Al_p(FeMo)$ and the monoclinic Al_3Fe phases. In addition, a phase, tentatively identified as the bcc $Al_{12}Mo$ (lattice parameter of 0.758 nm), was also identified. TEM micrographs, together with associated diffraction patterns for the $Al_6(FeMo)$, $Al_p(FeMo)$ and $Al_{12}Mo$ phases are shown in Figs. 32 and 33. Evidence for the monoclinic Al_3Fe phase is presented in the TEM micrographs and diffraction patterns in Figs. 34-35. This phase forms incoherently and displays fine twins (Figs. 34a and 35a), which produce extra reflections and streaks in the diffraction patterns [39]; the streaks form perpendicularly to the thin dimension of the twins. It appeared that the Al_3Fe phase formed at the grain boundaries from the $Al_6(FeMo)$ and $Al_p(FeMo)$ phases.

Al-8Fe-2Mo-0.5Si Alloy

The aging response of this alloy was remarkably different from that of the Al-8Fe-2Mo alloy. In contrast to the behavior of the ternary alloy at 0.25 hrs, precipitation was not limited to the grain and subgrain boundaries alone, but instead spread throughout the microstructure. A bright-field micrograph and associated SAD pattern demonstrating this effect are shown in Figs.

36a and 36b, respectively. The precipitates which form at the grain and sub-grain boundaries are larger than those within the grains; the latter appear with a straight-edged cuboidal/polygonal morphology, which indicates that nucleation has taken place coherently. A dark-field micrograph (Fig. 36c) obtained from the precipitate reflection indicated by the arrow in Fig. 36b images several precipitates with a common orientation. Precipitates having the same morpholoy as described above have been reported in Al-8Fe-V-Si alloys [21]. In these alloys, the precipitates have been identified as the bcc α-$Al_{12}Fe_3Si$ phase, which is isostructural with $Al_{15}Mn_3Si_2$. The similarity in the microstructures suggests that the Si effects have been reproduced in the Al-8Fe-2Mo alloy.

Further aging to 4 hrs produced virtually no change in the microstructure (Figs. 37a-c). Although the intragrain precipitation processes commenced somewhat earlier in the Si-bearing alloy relative to the Si-free alloy, the overall thermal stability was markedly superior, as evident from Fig. 38, which shows the microstructure after a 50 hr aging. There is some evidence of particle coarsening and spheroidization; however, the microstructure does not show the marked coarsening characteristic of the Al-8Fe-2Mo alloy. Moreover, no evidence was seen for the incoherent monoclinic Al_3Fe phase. EDS analyses indicated that the intragrain precipitates were based on Al and contained Fe and Si; small amounts of Mo were also present. A detailed investigation utilizing analytical electron microscopy and X-ray diffraction is being carried out to determine the crystallography and composition of the precipitates in Si-bearing Al-8Fe-2Mo alloys.

3.2.3 Microstructures of Compacted Material

Dynamic compaction utilizes the energy of a high-amplitude shock wave to consolidate particulate rather than the combined effects of high temperature and high pressure. In this technique, a shock wave is generated in the powder mass either by the impact of a high-velocity projectile or by an explosive front. The dynamic compaction device utilized in this work consists of a light-gas "gun" through which a projectile is accelerated to high velocities until it impacts the powder assembly, generating a high-amplitude shock wave within the powder mass. This device is shown schematically in Fig. 39. Accelerating gas pressures of 2000 to 3500 psi result in projectile velocities of 1200 to 1500 m/s. The shock pressures generated within the powder mass are estimated to be on the order of 2-8 GPa. Dynamic compaction is capable of producing compacts which are near theoretical density in a wide variety of materials. The aluminum alloy compacts produced in this work were all > 98% of theoretical density.

In dynamic compaction, as the shock wave travels through the powder assembly, it deforms the powders to fill void space, losing energy in the process. It is theorized that local surface melting occurs during this process and accounts for some of the interparticle bonding in the compact. Recent evidence suggests that, while local melting may indeed occur, the distribution

43

and extent of such melting is minimal and probably does not influence the interparticle bonds significantly [42]. Instead, this evidence shows that the most likely influence of dynamic compaction on interparticle bonding is the extreme local deformation and disruption of surface oxide layers which inhibit bonding. Generally, the interparticle bonding in dynamically consolidated pieces is poor. Consequently, additional consolidation routes which may produce well-bonded pieces of material with retained RS microstructures are also being examined in this program.

The Al-8Fe-2Mo alloy was consolidated by extrusion and dynamic compaction. The RS ribbon was produced by melt-spinning onto a copper wheel in a helium atmosphere. The ribbon produced was examined optically, by TEM, and mechanically (bend test) to ensure that it possessed the desirable Zone A microstructure. The ribbon was then reduced to particulate using a rotating blade technique. For the extrusion, ribbon particulate was packed into an OFHC copper can, hot-outgassed, and then sealed. The can was soaked at 300°C for two hours prior to blank-die hot compaction at a pressure of 1270 MPa. The compacted can was then soaked for two hours at 300°C and extruded at a 14:1 extrusion ratio. For dynamic compaction, the particulate was loaded into a steel powder can, hot-outgassed and then sealed. The can was placed into the compaction device with no other treatments. The gun firing pressure, which was 20 MPa, resulted in a projectile velocity of 1133 m/s. The initial shock pressure induced in the powder material is estimated to be ≈ 4 GPa. In addition to dynamic compaction alone, a hybrid process involving dynamic compaction followed by HIP was attempted. HIP was performed in a conventional HIP unit operating at 186 MPa (27 ksi). The Al-8Fe-2Mo DC'd compact was not placed in a container for HIP. Instead, the DC'd compact was canless-HIP'd at 350°C for 2 hours. The density of the consolidated materials was calculated using the measured mass and micrometer measurements of the dimensions of test specimens. The consolidated material was sectioned for optical and TEM specimen preparation and test specimens were machined from the remaining material.

The extruded material appeared to be 100% dense except near an area where there had been a surface rupture of the can. Most of the pores were found at prior particle boundaries. A representative optical micrograph of the material is shown in Fig. 40. A large volume fraction of the material has very little etching response, consistent with the presence of the Zone A microstructure[12] and implying that the as-rapidly solidified microstructure has been retained in the extruded material. However, TEM revealed that this was not the case.

In TEM, the extruded Al-8Fe-2Mo material was observed to possess two different types of microstructures. One type consisting of very fine equiaxed subgrains of Al, approximately 0.5μm in diameter, with particles at subgrain boundaries. This microstructure is shown in Fig. 41. In the other type of microstructure grains were much larger, on the order of 10-20μm, with large needles in the grain interior, as shown in Fig. 42. Coarse particles are also present at grain

44

boundaries. Both of these microstructures are similar to those observed in overaged laser-surface-melted material. Based on this observation and by analogy with the heat-treated structures, the large needles are assumed to be θ' Al_3Fe and the coarse particles at grain boundaries are assumed to be Al_6Fe. No trends between location in the extrusion and volume fraction of a particular morphology were evident.

The extruded material possessed a microstructure that was completely decomposed, even though the parent microstructure should have been stable at the extrusion temperature. This implies that there is some factor involved in the extrusion which accelerates the decomposition kinetics of this material.

Dynamic compaction of the Al-8Fe-2Mo produced compacts which were >99% of theoretical density but suffered from flaking and some cracking. Optically, the dynamically compacted Al-8Fe-2Mo was observed to possess a laminated structure consisting of Zone A flakes, as shown in Fig. 43. The interparticle boundaries were clearly evident and there was no indication of interparticle melting. The bonding, which was achieved by mechanical interlocking of the flakes, was such that some of the surface pieces could be flaked off. It was apparent that the Zone A microstructure produced by rapid solidification had been retained and TEM observations of the microstructure verified these findings. The microstructure consisted of large areas of Zone A as shown in Fig. 44, although in some isolated regions dynamic recrystallization had occurred, leaving very fine equiaxed Al grains. Such a recrystallized area is shown in Fig. 45. In a few isolated areas, more extensive decomposition had occurred, the intercellular phase having decomposed into coarse Al_6Fe. An example of this type of area is shown in Fig. 46. These anomalous areas were observed infrequently and do not seem to be associated with interparticle boundaries. There was no evidence of the θ' Al_3Fe phase anywhere in the compact. This observation assumes more significance when it is recalled that in thermally decomposed ribbon the microstructure generally consists of Al grains with Al_6Fe particles at the grain boundaries and numerous θ' Al_3Fe needles within the Al grains [40]. Thus, the microstructure observed in the decomposed regions in the DC'd material varies drastically compared with thermally decomposed material. This difference suggests some change in the conditions under which decomposition has occurred. Future work involving the phases produced during decomposition under various conditions may give some insight as to the temperatures and stresses which were experienced during consolidation.

In the Al-8Fe-2Mo ribbon which was dynamically compacted and then hot-isostatically pressed the result was similar. Optically, the Zone A appeared to have been retained during the subsequent HIP as shown in Fig. 47a. The interparticle boundaries were again clearly evident with no evidence of sintering. TEM observation confirmed these findings. The predominant feature of the microstructure was large areas of unaffected Zone A, an example of which is seen in

45

Fig. 47b. In a few isolated areas long bands of Al_6Fe were observed, such as those illustrated in Fig. 48; these are believed to have formed by growth of the smaller Al_6Fe particles found in the dynamically compacted material. Thus, the only effect of HIP on the dynamically compacted material was a slight growth in the Al_6Fe particles which formed during dynamic compaction and there appeared to be no effect of HIP on the retained Zone A.

The mechanical properties of the extruded Al-8Fe-2Mo were good despite the loss of the original RS microstructure during consolidation. Mechanical properties were measured by tension tests and by fracture toughness tests performed on sub-size fracture toughness specimens. Monotonic tensile test results are shown in Table 5. The 20°C and 315°C values for strength and ductility are comparable to those published for pre-alloyed powder extruded with similar parameters [11]. Fracture surfaces of the 20°C and 315°C tensile specimens were examined by scanning electron microscopy (SEM). The fractographs in Fig. 48 show a difference between the 20°C and 315°C test specimens. Individual pieces of ribbon can be discerned in the 315°C specimen whereas the 20°C specimen has a more "normal" fracture surface. One possible

Table 5

Results of tensile tests performed on extruded ribbon tested at 20°C and 315°C.

Test Temperature (°C)	Young's Modulus (GPa)	Yield Strength (0.2% offset) (MPa)	Ultimate Tensile Strength (MPa)	Reduction in Area (%)
20	82.0	404	462	4.0
315	63.4	239	282	32.5

explanation for this difference in fracture surface appearance is that at elevated temperatures the strain to failure of the bonds at ribbon interfaces is much less than that of the ribbons themselves. The bonds would then fail early in the test whereas individual ribbon pieces could accomodate a much higher strain. This mechanism would allow the material to behave as a continuous body, accounting for the large reductions in area, until it was near to failure and the bonds separated, allowing each ribbon to neck and fail somewhat independently.

The fracture toughness of the extruded ribbon was measured using chevron-notched short-rod specimens tested in a Fracjack loading device [43]. These results, along with the results of other Al alloys tested in the device are reported in Table 6. Specimens from an extrusion of

Table 6

Fracture toughness results from tests performed on extruded ribbon and powder.

Alloy	MPa√m
7075-T6511	22.8
7178-T6511	17.1
Al-8Fe-2Mo	
PWA powder	9.25 avg.
UIUC ribbon	13.25

Al-8Fe-2Mo produced by Pratt and Whitney Aircraft Group are included for comparison. The latter was produced with parameters nearly identical to that of the extruded ribbon, but more importantly, with atomized powders rather than ribbon. Originally, the powder had a very large volume fraction of Zone B which contains large microstructural constituents whereas the ribbon had a very fine cellular structure. During extrusion, Zone B would decompose into a coarser microstructure than Zone A. It is presumed that increased fracture toughness of the extruded ribbon is an effect of microstructure, the extruded powder having a higher volume fraction of coarse intermetallic particles compared to the extruded ribbon. It appears, then, that ribbon poses at least one advantage over powder, that being an improvement in fracture toughness, although the fracture toughness of the extruded ribbon is still less than that of other high-strength Al-alloys. This is probably due to the presence of intermetallic needles in these alloys which serve as efficient crack paths, thus reducing the toughness of Al-8Fe-2Mo alloys.

The mechanical properties of the Al-8Fe-2Mo compacts produced by dynamic compaction and by the hybrid process were not evaluated due to the lack of integrity of the samples. Rockwell "B" hardness measurements of the compacts were ≈50 on the transverse section. Hardness measurements on longitudinal sections resulted in cracking due to delamination. Tensile specimens machined from the compacts suffered from flaking and crushed in the test machine grips, demonstrating the lack of interparticle bonding. Thus, while the retention of RS microstructures during DC is a major advantage of the process, the lack of good interparticle bonding limits the process. The lack of any significant effect on the rapidly solidified microstructure by the subsequent HIP is encouraging. Future attempts using this technique will involve sealing the compacted material in a HIP can to prevent gas from permeating particle boundaries.

Experiments designed to examine enhanced microstructural degradation were performed on laser-treated material. The extrusion of rapidly solidified ribbon was performed at temperatures well below those at which the Zone A microstructure decomposes. Thus, it seems likely that there is some factor involved which accelerated the coarsening rate. These experiments were designed to examine such effects. Laser passes were produced on cast slabs of Al-8Fe-2Mo. These laser-treated slabs were then ground from the back side until the laser pass penetrated the thickness of the slab, as indicated schematically in Fig. 50. Some laser passes were deformed by cold rolling and subsequently heat-treated to assess the effect of plastic deformation on decomposition. Other laser passes were heat-treated while a compressive stress was simultaneously applied to identify any stress-enhanced decomposition. The effect of these treatments was then evaluated by optical and transmission electron microscopy.

The cold-rolled laser passes were rolled to various deformations to introduce plastic strains of 25 to 75%. The deformed laser passes were then heat-treated at 400°C for 2 hours; conditions under which the stability of the Zone A microstructure is tenuous. The specimens were then examined by TEM to assess the amount of decompostion that had occurred. Fig. 51 shows a typical example of the resultant microstructure for a sample which had been cold-rolled 65% and then heat-treated. In all cases the microstructures were similar to that expected for a purely thermal treatment at 400°C for 2 hours. Therefore, particle deformation is probably not a dominant factor in governing the enhanced decomposition of the Zone A microstructure in Al-8Fe-2Mo.

The laser passes to which a stress had been applied while at elevated temperatures showed similar results. Samples were held at temperatures of 260°C, 300°C, 360°C, 400°C and 450°C. Stresses applied at each temperature ranged from 138 MPa (20 ksi) to 517 MPa (75 ksi). For all stress levels applied to specimens heated to 400°C or less, no accelerated decomposition was observed. All of the specimens heated to 450°C had decomposed entirely. These results are consistent with the thermal stability of this alloy, and indicate a minimal effect of applied stress on the decomposition kinetics of the Zone A microstructure in Al-8Fe-2Mo.

These results indicate that particle deformation and applied stress have little effect on the decomposition of the Zone A microstructure in Al-8Fe-2Mo, and it is likely that adiabatic heating during the extrusion process is the dominant factor involved in the decomposition of this microstructure during extrusion. In order to negate the effect of adiabatic heating, a lower initial particulate temperature may be required. However, interparticle bonding will be difficult to achieve under such conditions, and it may be impossible to force the material through the extrusion die. Thus, the problem of effective consolidation of rapidly solidified particulate limits full exploitation of rapid solidification processing of aluminum alloys.
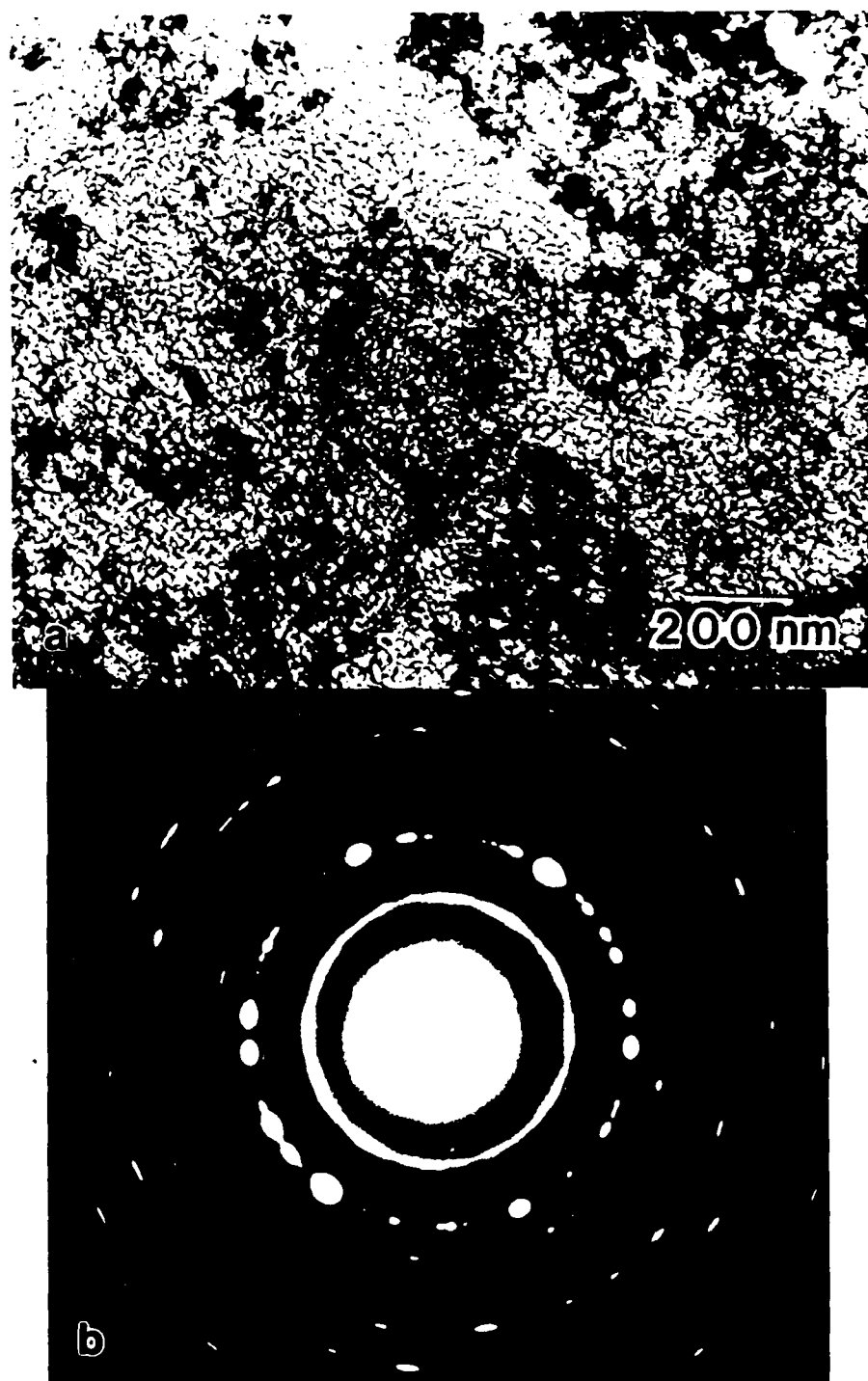
Fig. 26. As-rapidly solidified microstructure of Al-8Fe-2Mo-0.5Si ribbon. a) BF micrograph; b) SAD pattern.
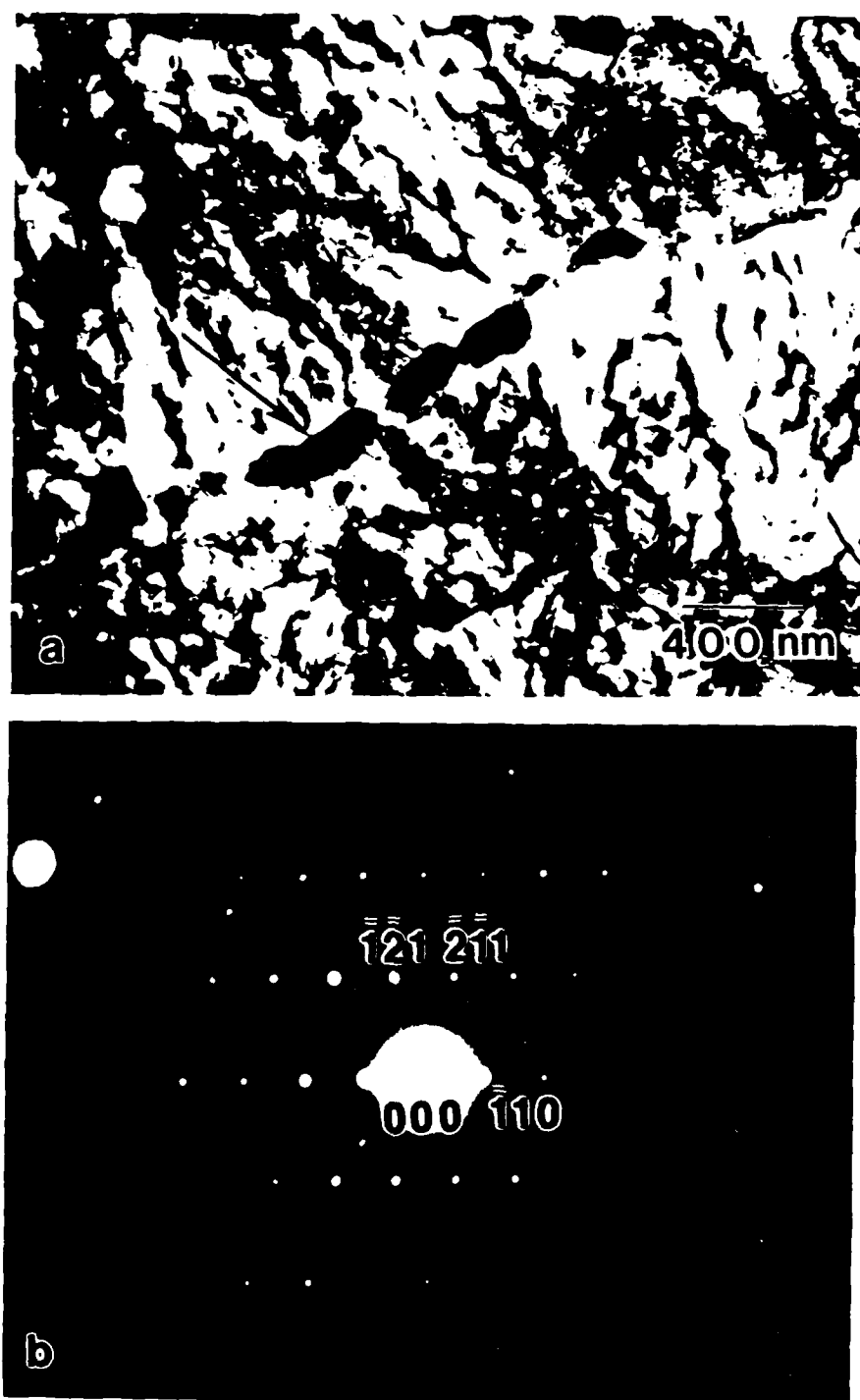
Fig. 27. Microstructure of Al-8Fe-2Mo ribbon aged at 450°C for 0.25 hrs. a) BF micrograph showing precipitation at grain boundaries; b) [113] SAD pattern of precipitate indicated by the arrow in "a".
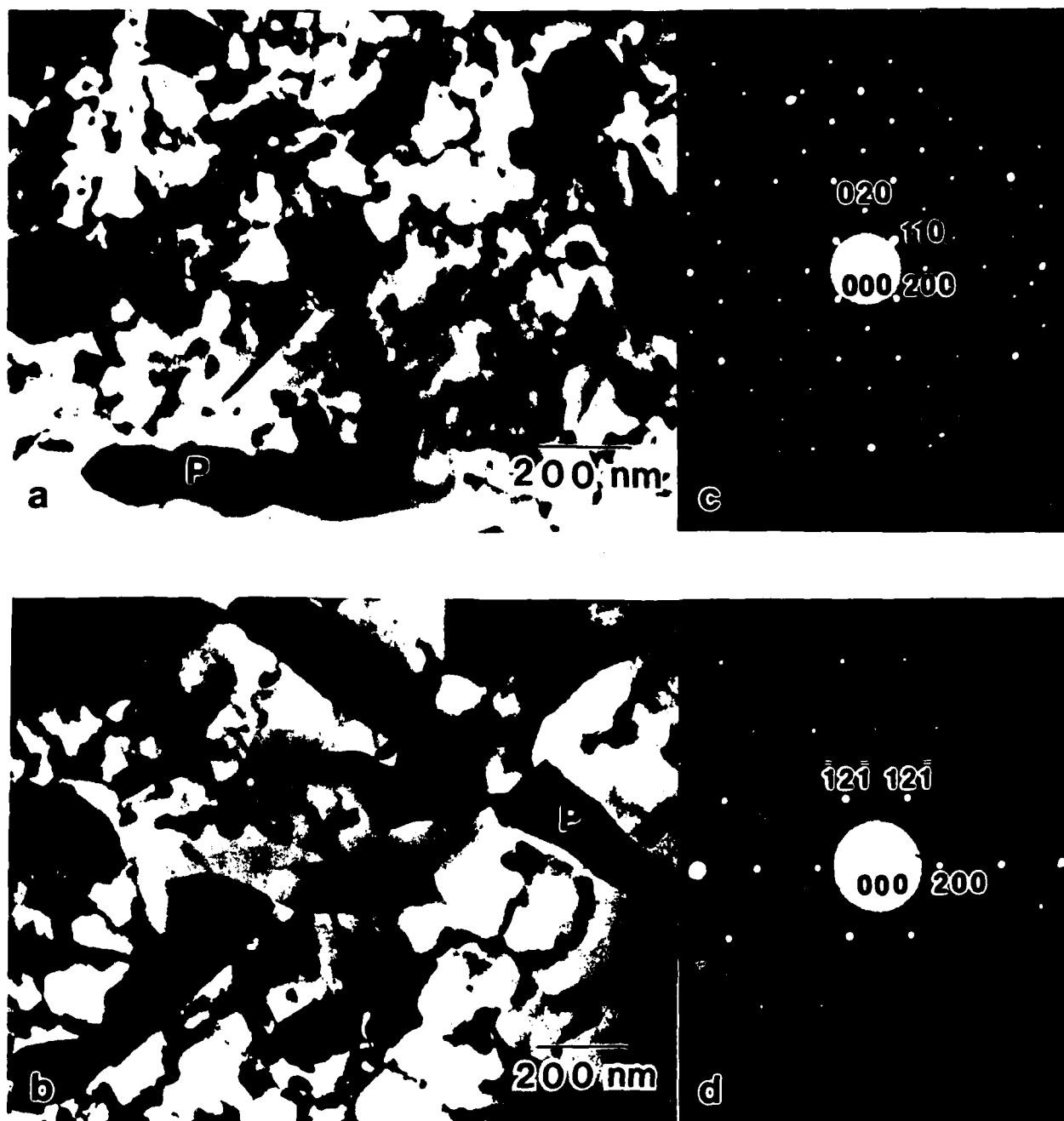
50

Fig. 28. Microstructures of thicker portions of the Al-8Fe-2Mo ribbon aged at 450°C for 0.25 hrs.
a), b) BF micrographs; c), d) [001] and [012] SAD patterns of the bcc Al_p(FeMo) particle
labelled P in "a" and "b", respectively.
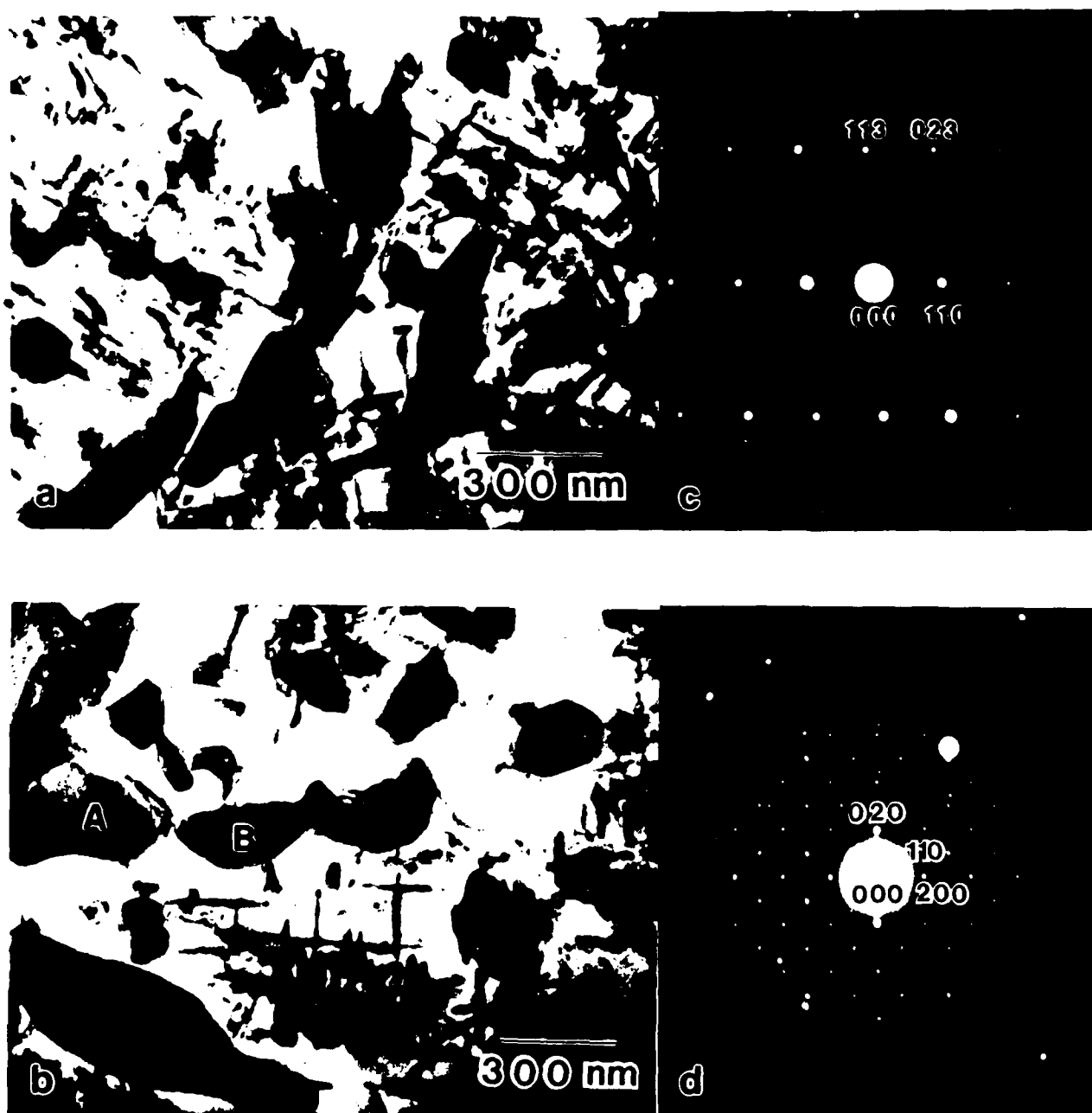
Fig. 29. Microstructures of Al-8Fe-2Mo ribbon aged at 450°C for 4 hrs. a), b) BF micrographs; c) [33$\bar{2}$] and [001] SAD patterns of precipitates labelled A (Al$_6$(FeMo)) and B (Al$_p$(FeMo)), respectively, in "b".

52
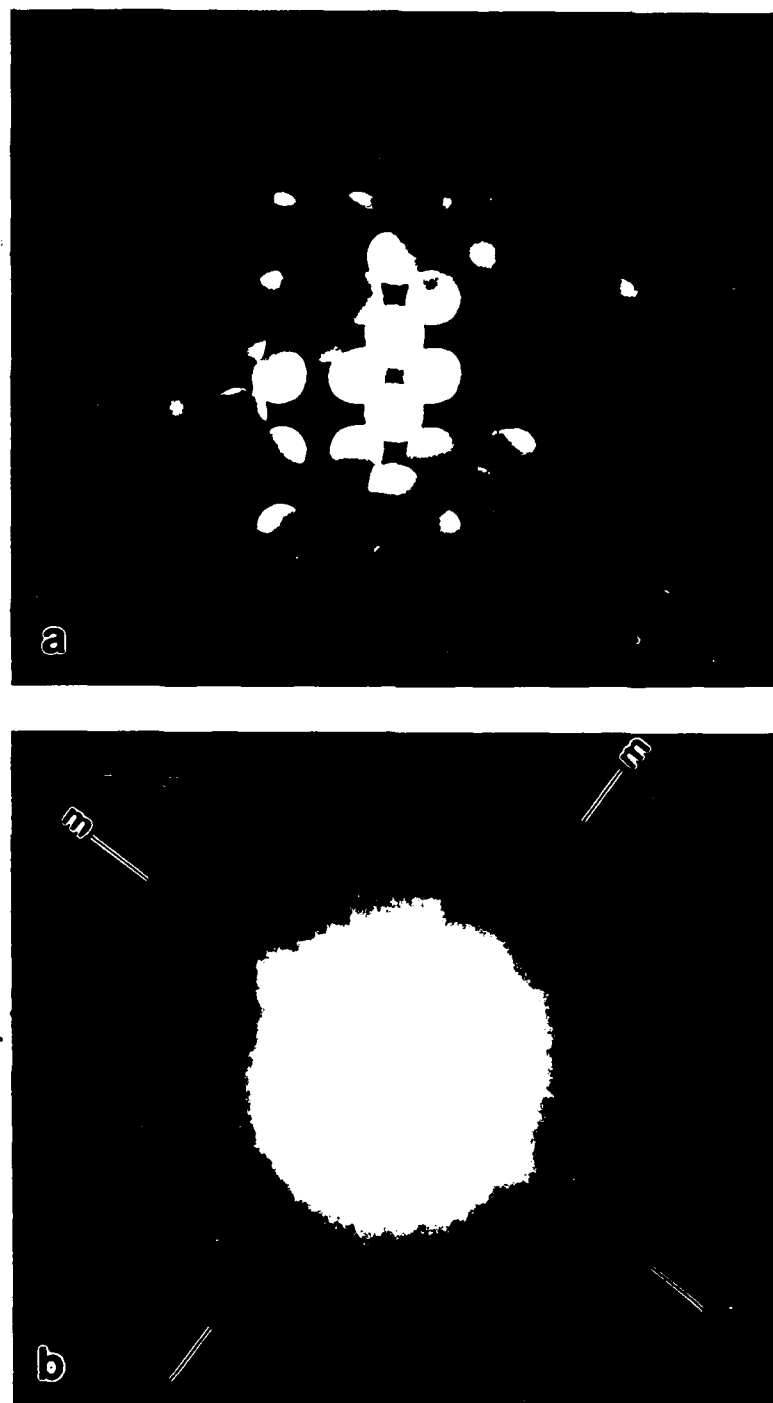
Fig. 30. [001] convergent beam patterns of precipitate labelled B in Fig. 29b. a) ZOLZ; b) FOLZ.
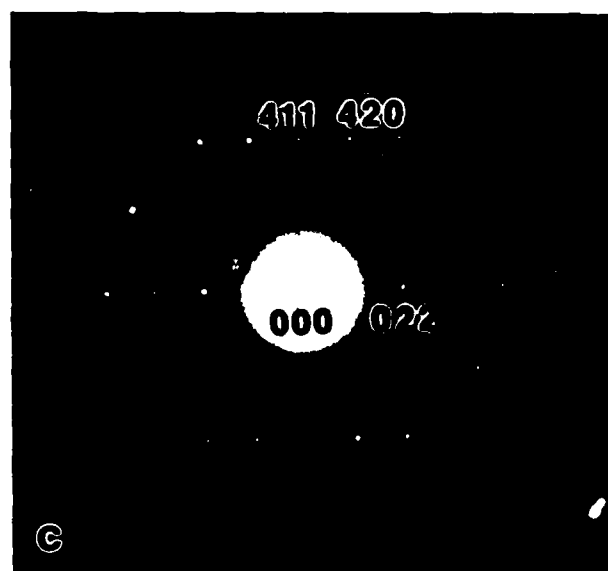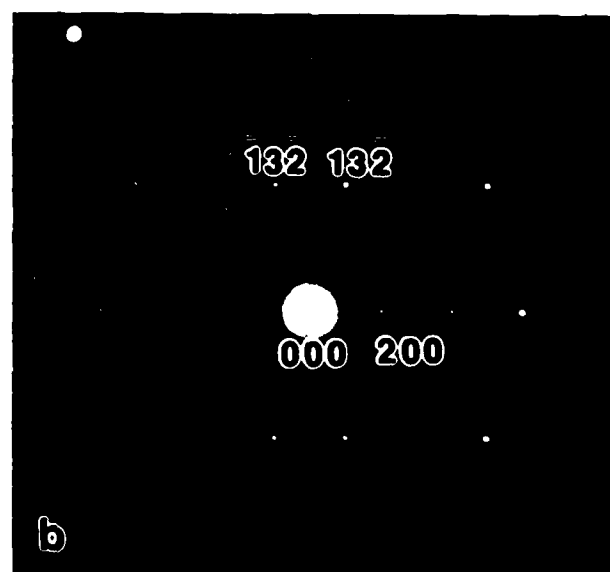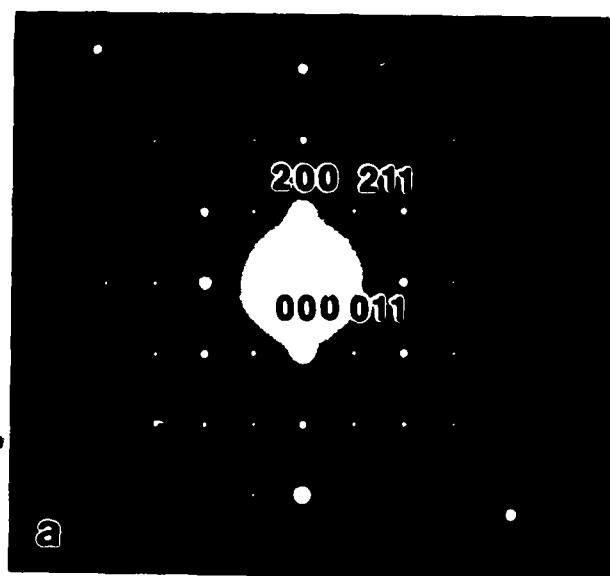
Fig. 31. Additional examples of SAD patterns taken of the bcc $Al_p(FeMo)$ phase in the Al-8Fe-2Mo ribbon aged at 450°C for 4 hrs. a) [011]; b) [023]; c) [122].
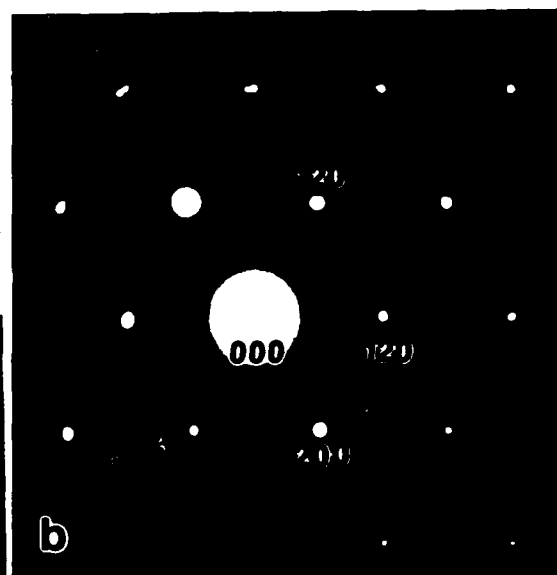
Fig. 32. Microstructure of Al-8Fe-2Mo ribbon aged at 450°C for 50 hrs showing coarse
Al$_6$(FeMo) precipitates. a) BF micrograph; b) [004] SAD pattern of "a"; c) DF
micrograph from spot indicated by arrow in "b".
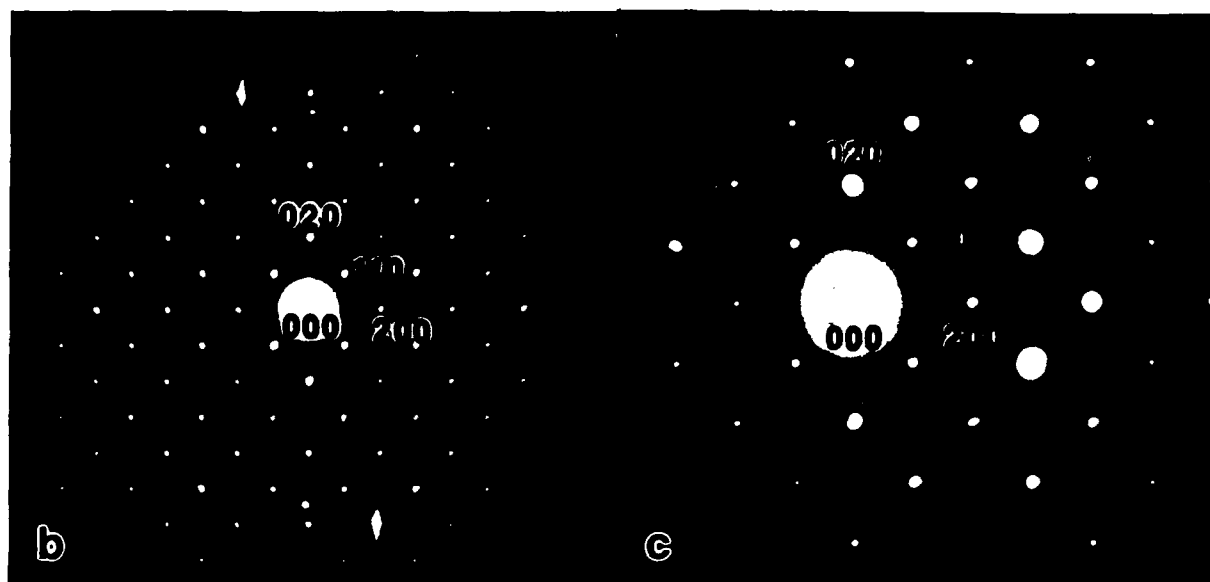
Fig. 33. Microstructure of Al-8Fe-2Mo ribbon aged at 450°C for 50 hrs. a) BF micrograph showing the Al_p(FeMo) phase (labelled A) and the bcc phase, tentatively identified as $Al_{12}Mo$ (labelled B); b) and c) are [001] SAD patterns of the precipitates labelled A and B in "a".
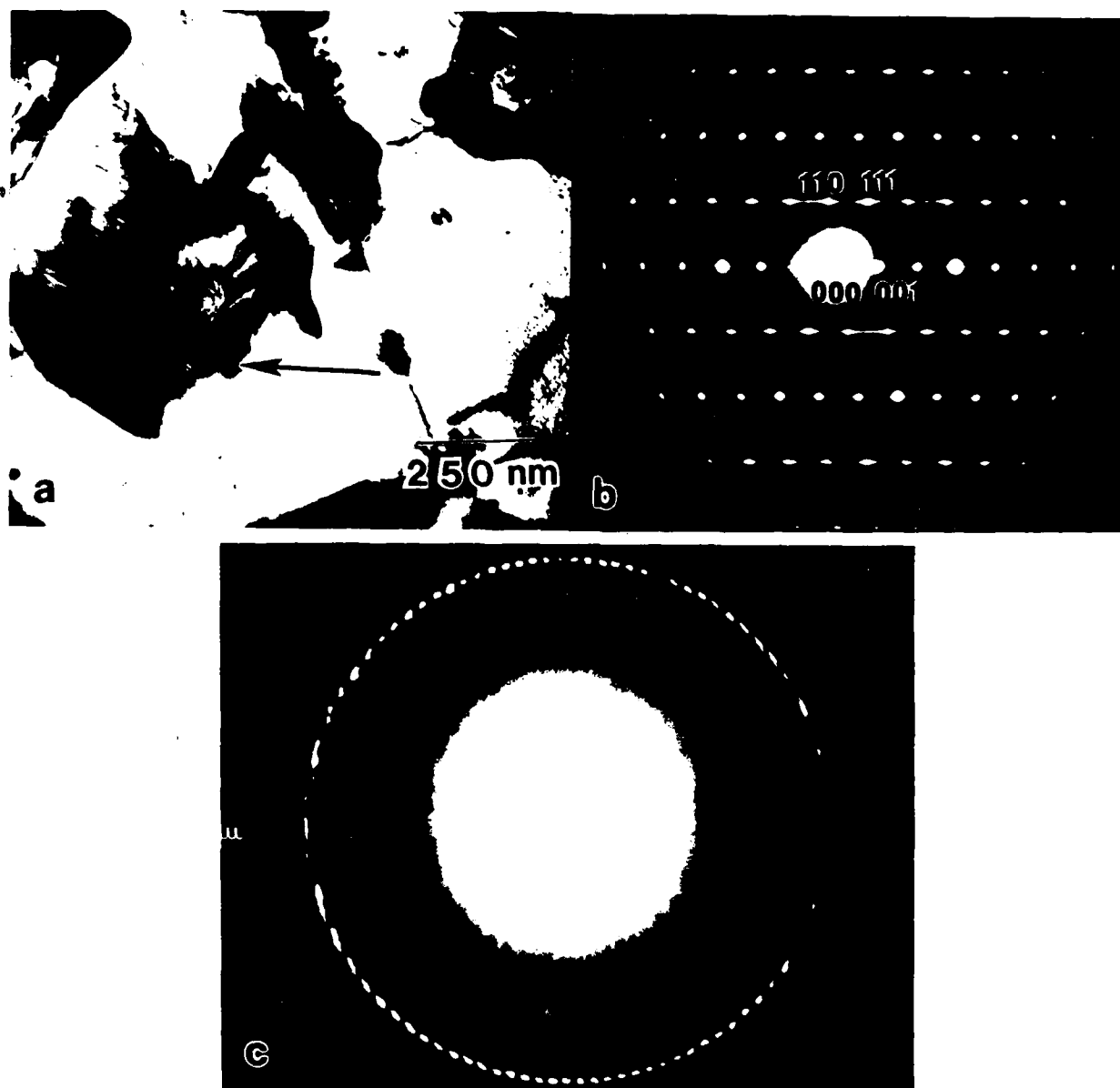
Fig. 34. Example showing the formation of the incoherent monoclinic Al₃Fe phase in the Al-8Fe-
2Mo ribbon aged at 450°C for 50 hrs. a) BF micrograph; b) and c) [110] SAD and
CBED patterns, respectively, of the Al₃Fe precipitate indicated by the arrow in "a".

57
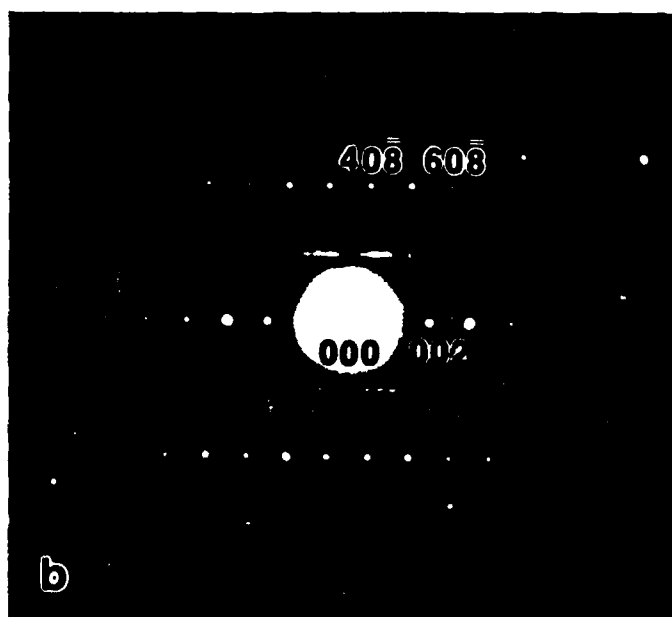
Fig. 35. An additional example of the monoclinic Al₃Fe phase in the Al-8Fe-2Mo ribbon aged at
450°C for 50 hrs. a) BF micrograph; b) [010] SAD pattern of the Al₃Fe precipitate
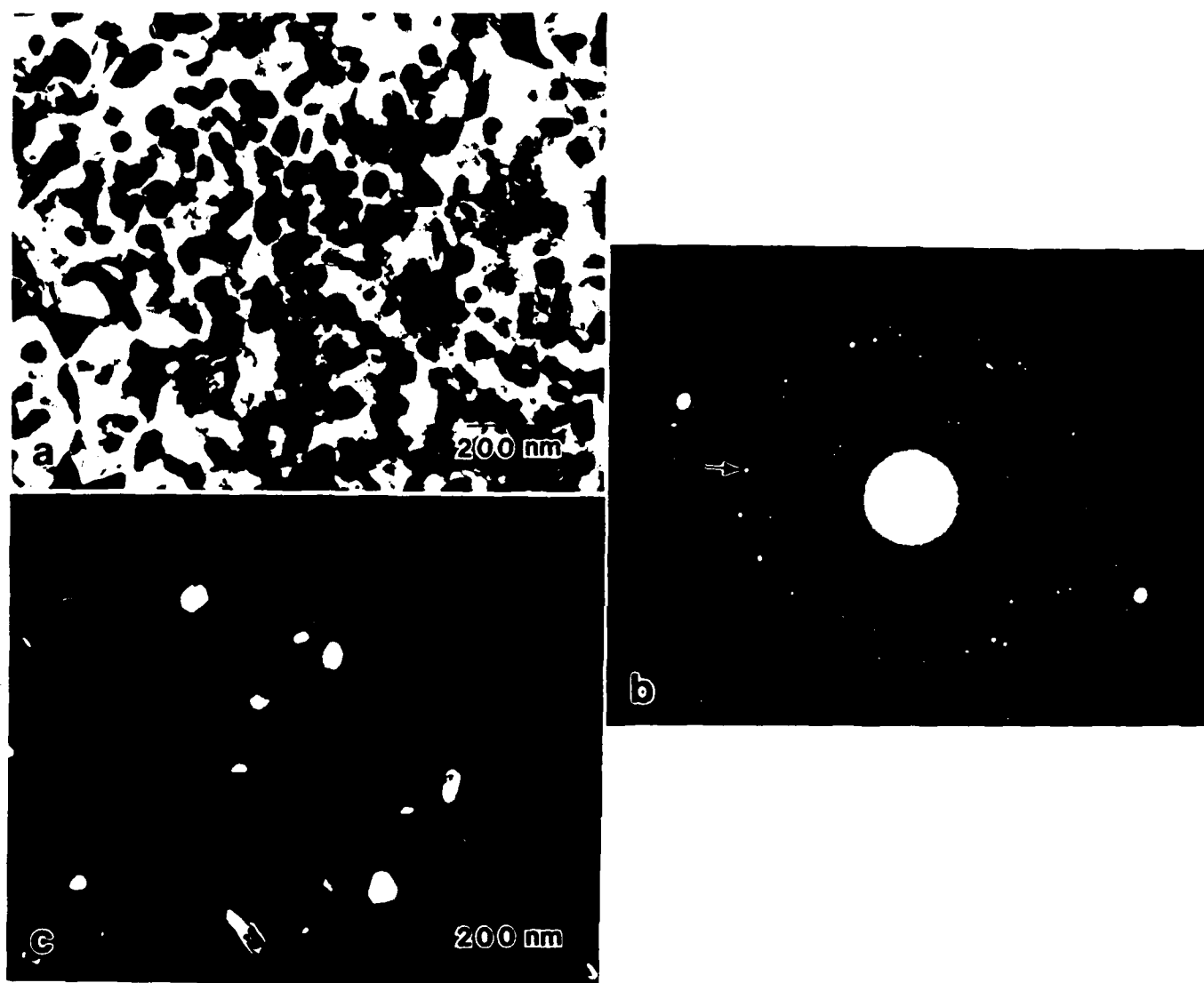indicated by the arrow in "a"..

58

Fig. 36. Microstructure of Al-8Fe-2Mo-0.5Si ribbon aged at 450°C for 0.25 hrs. a) BF micrograph; b) SAD pattern; c) DF from precipitate spot indicated by the arrow in "b".
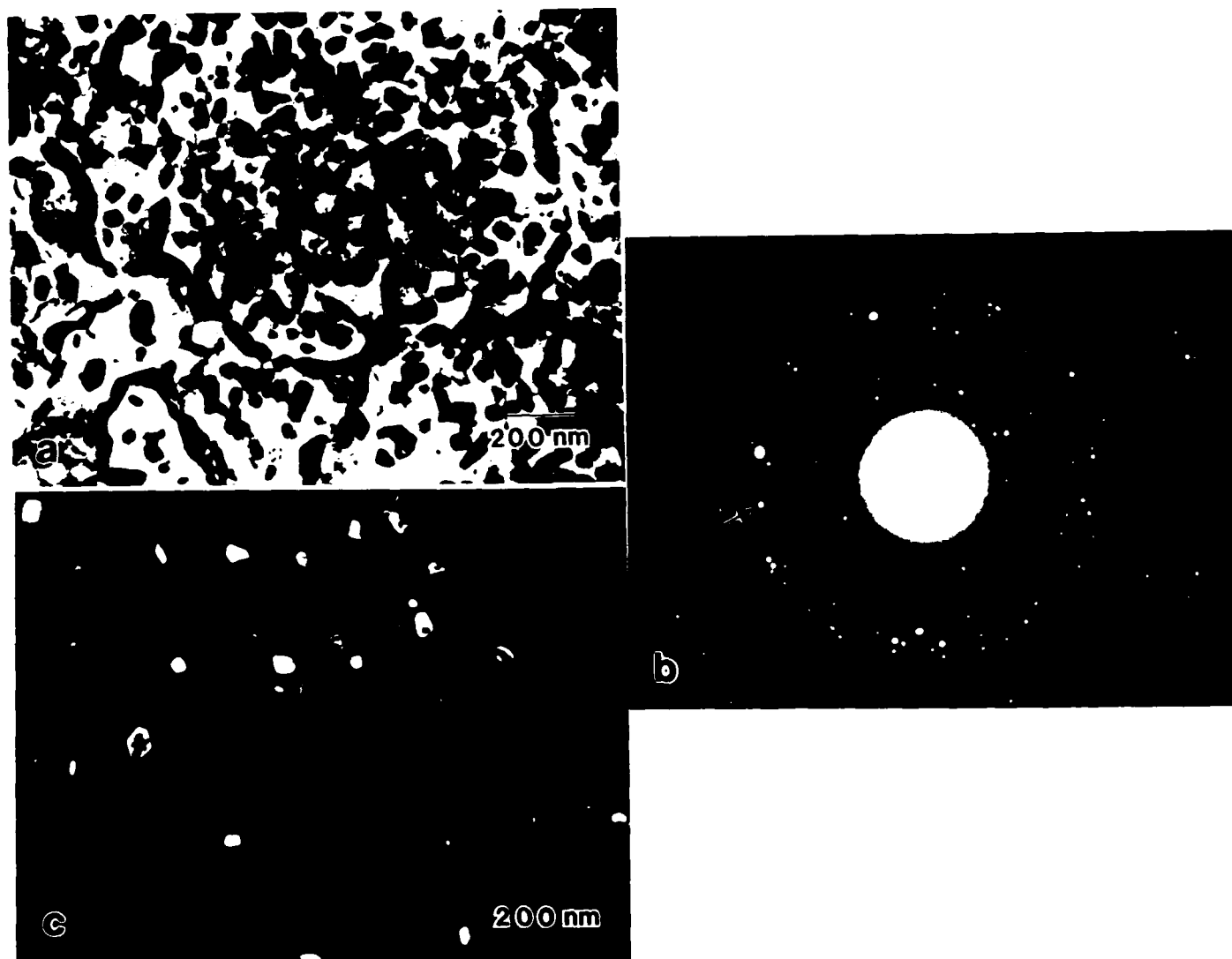
Fig. 37. Microstructure of Al-8Fe-2Mo-0.5Si ribbon aged at 450°C for 4 hrs. a) BF micrograph;
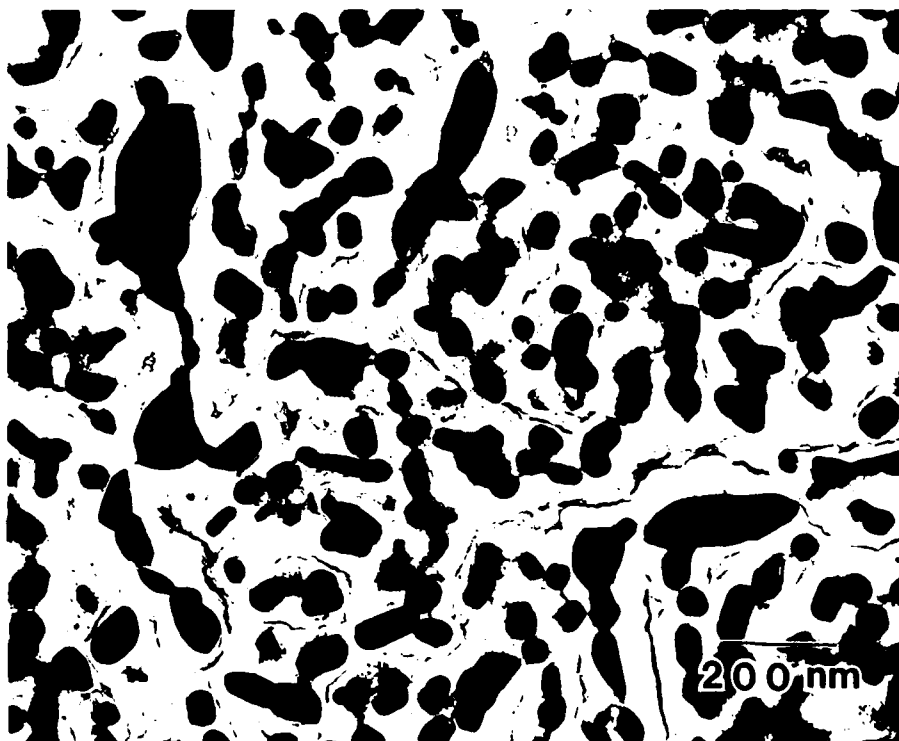b) SAD pattern; c) DF from precipitate spot indicated by the arrow in "b".

Fig. 38. BF micrograph of Al-8Fe-2Mo-0.5Si ribbon aged at 450°C for 50 hrs.
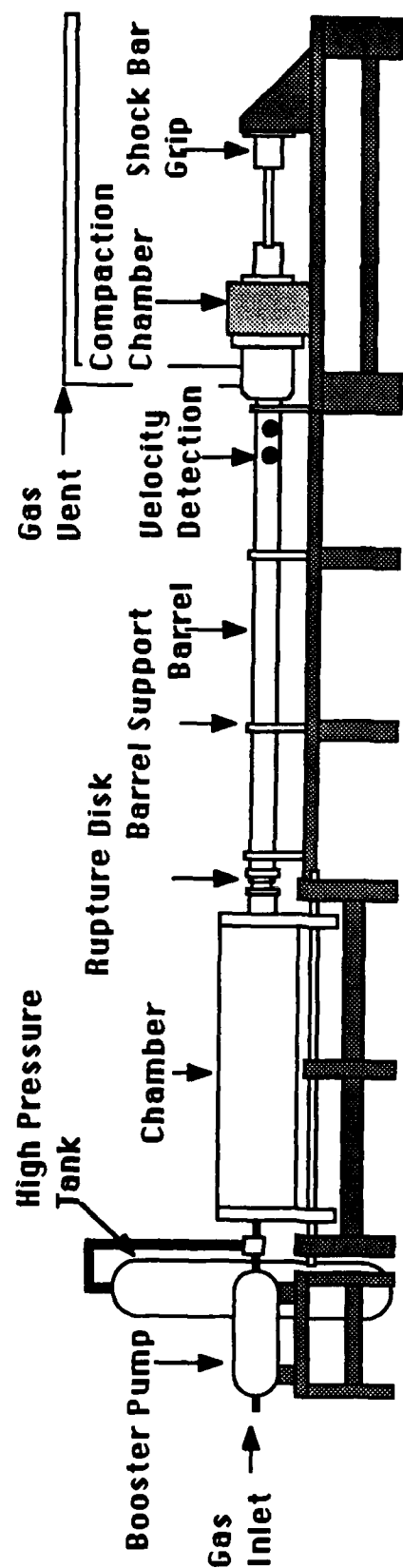
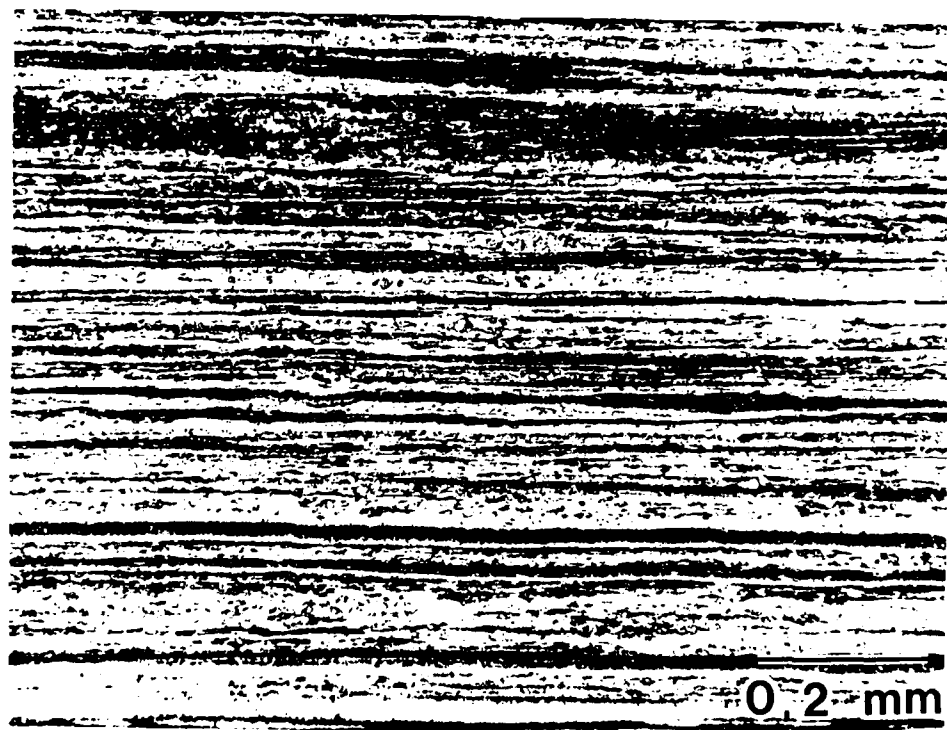Fig. 39.   Schematic diagram of the dynamic compaction device.

Fig. 40. Light optical micrograph of a longitudinal cross-section of the extruded Al-8Fe-2Mo ribbon. Etched with Keller's reagent.
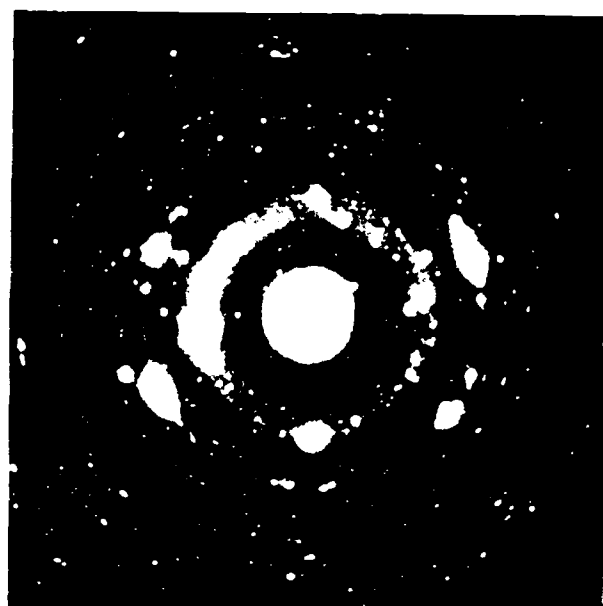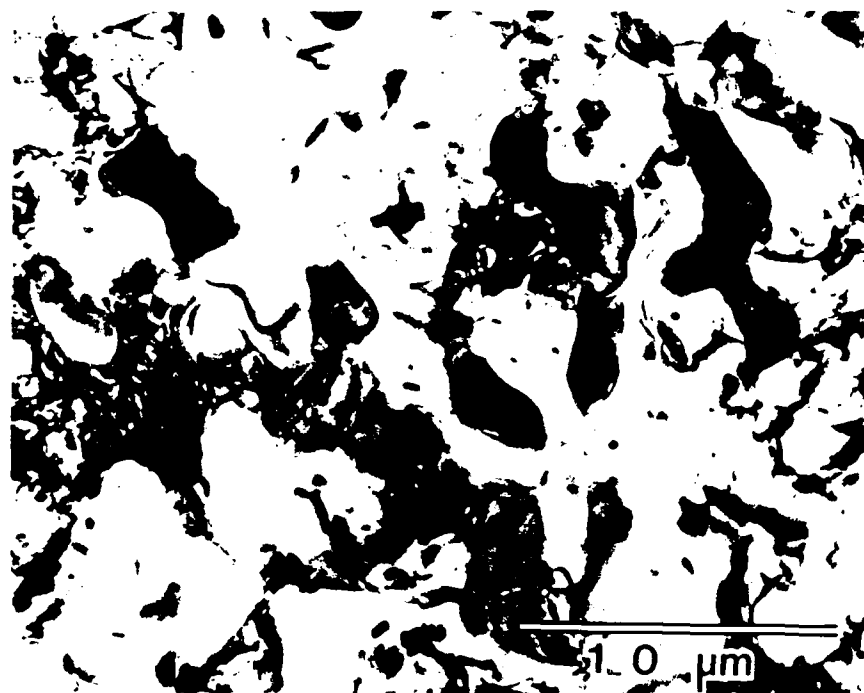
Fig. 41. Bright-field transmission electron micrograph and associated SAD pattern showing one
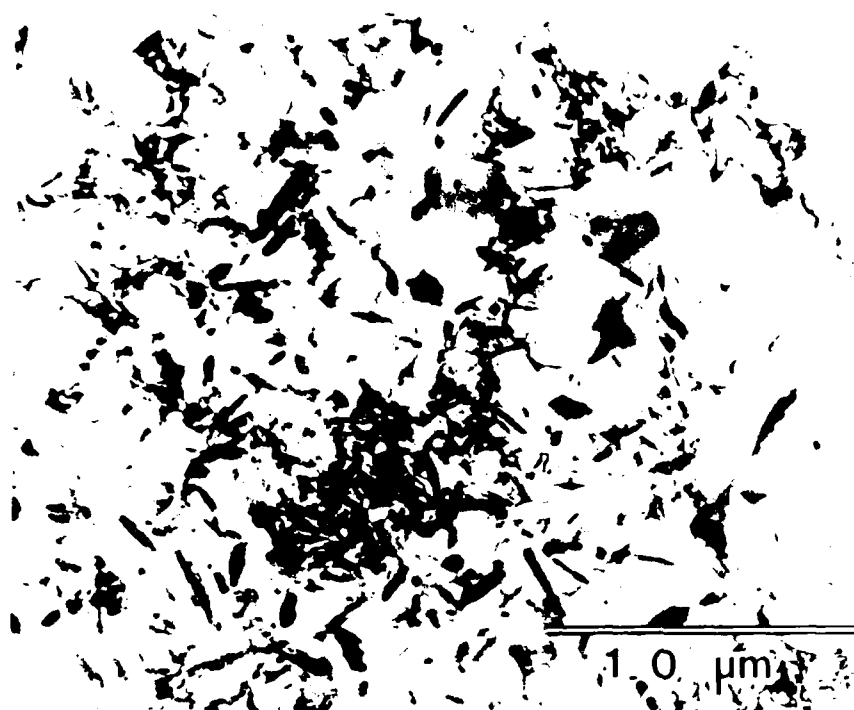type of microstructure observed in the extruded ribbon.

Fig. 42. Bright-field transmission electron micrograph and associated SAD pattern showing a second type of microstructure observed in the extruded ribbon.
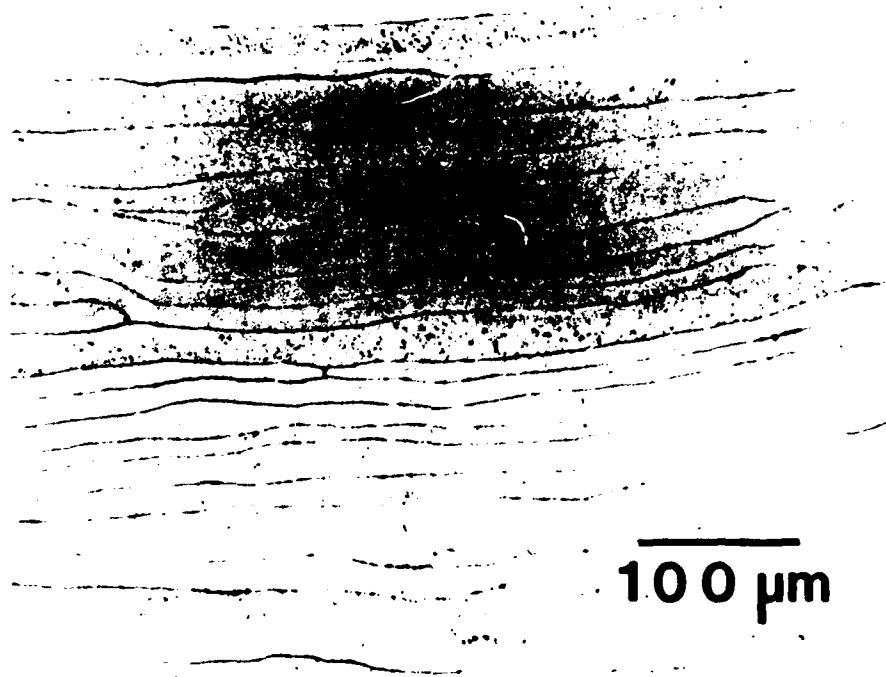
65

Fig. 43. Optical micrograph of dynamically compacted Al-8Fe-2Mo ribbon particulate.
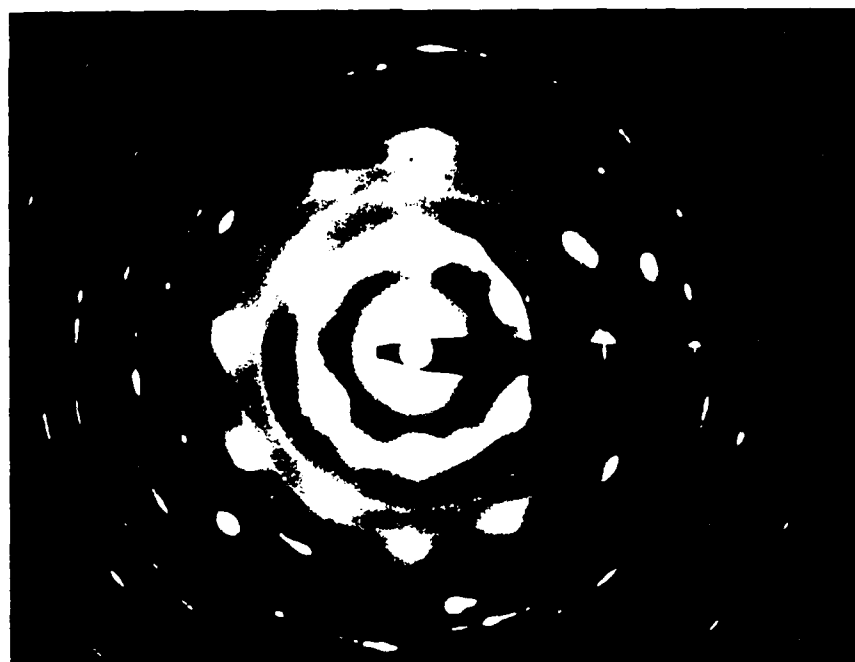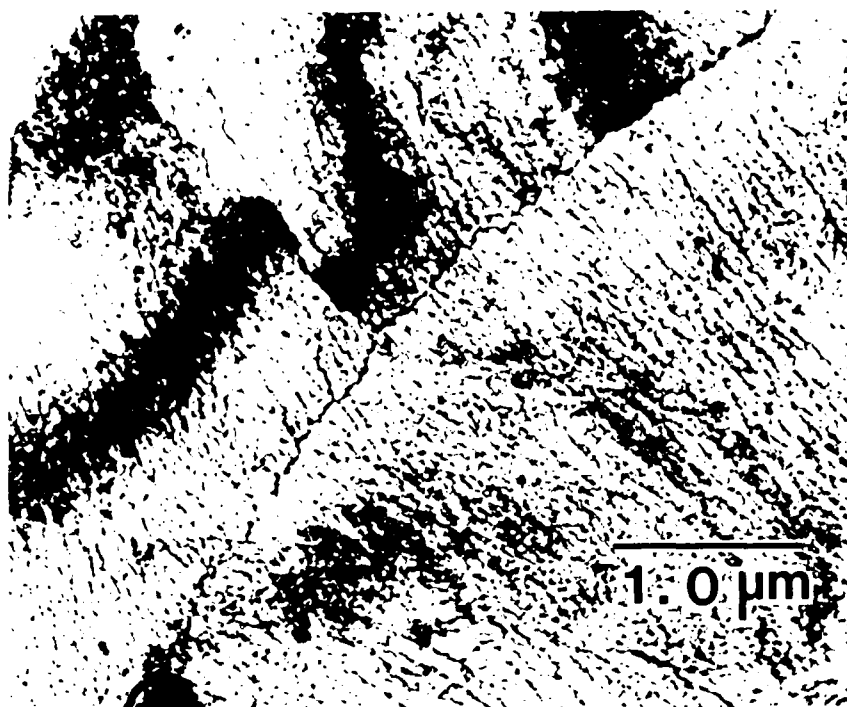
Fig. 44. Bright-field transmission electron micrograph and associated SAD pattern of the zone A microstructure in dynamically compacted Al-8Fe-2Mo ribbon particulate.
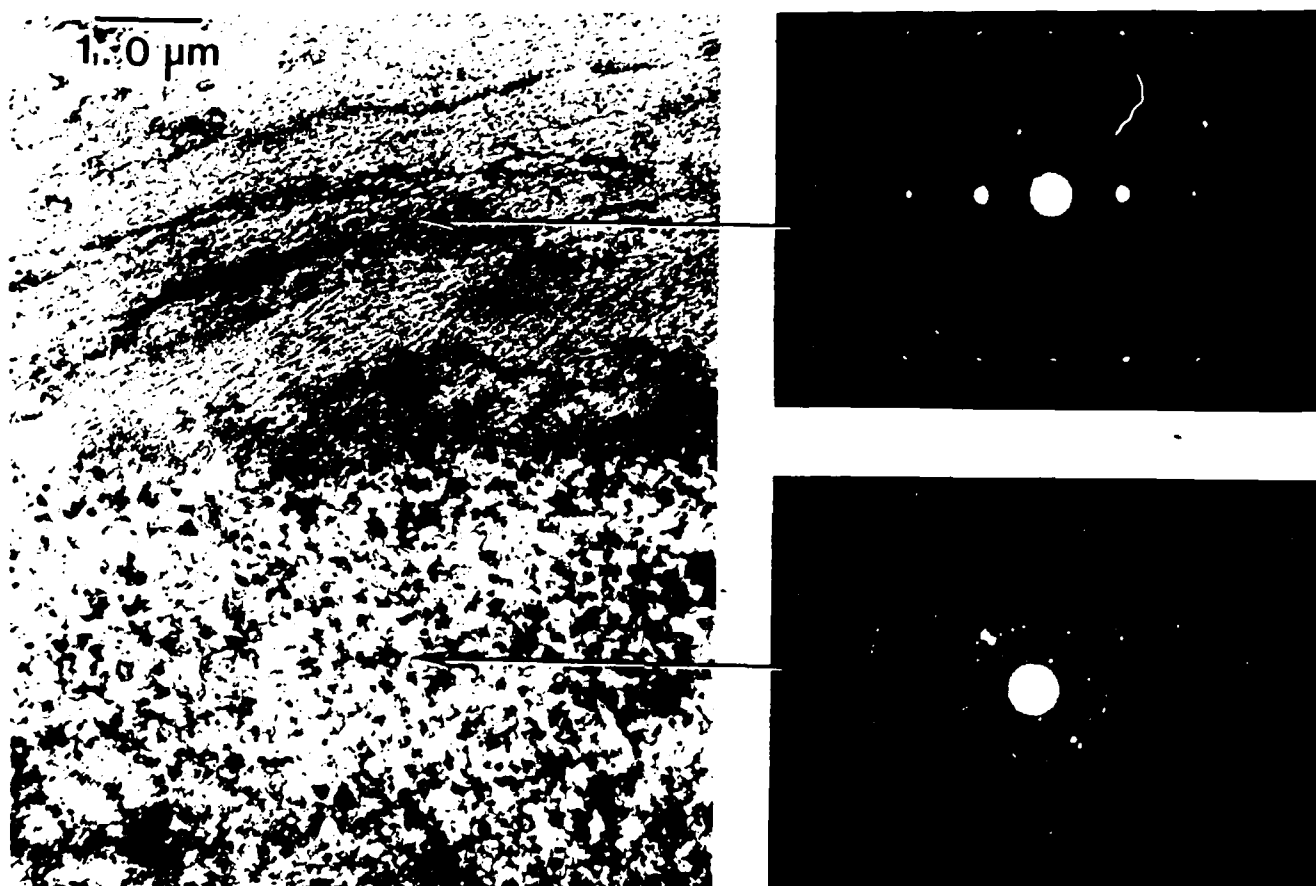
Fig. 45. Bright-field transmission electron micrograph and associated SAD pattern of
recrystallized grains within the zone A matrix in dynamically compacted Al-8Fe-2Mo
ribbon particulate.

Fig. 46. Optical micrograph of dynamically compacted and canless HIP'd Al-8Fe-2Mo ribbon particulate.
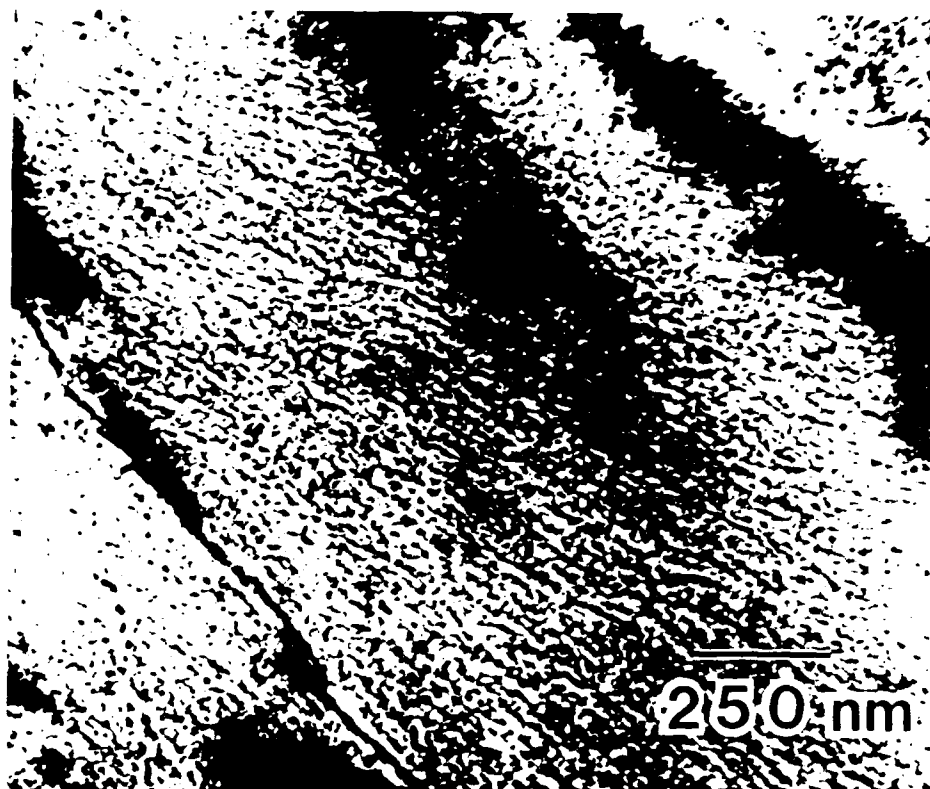
Fig. 47. Bright-field transmission electron micrograph of the zone A microstructure in dynamically compacted and canless HIP'd Al-8Fe-2Mo ribbon particulate.
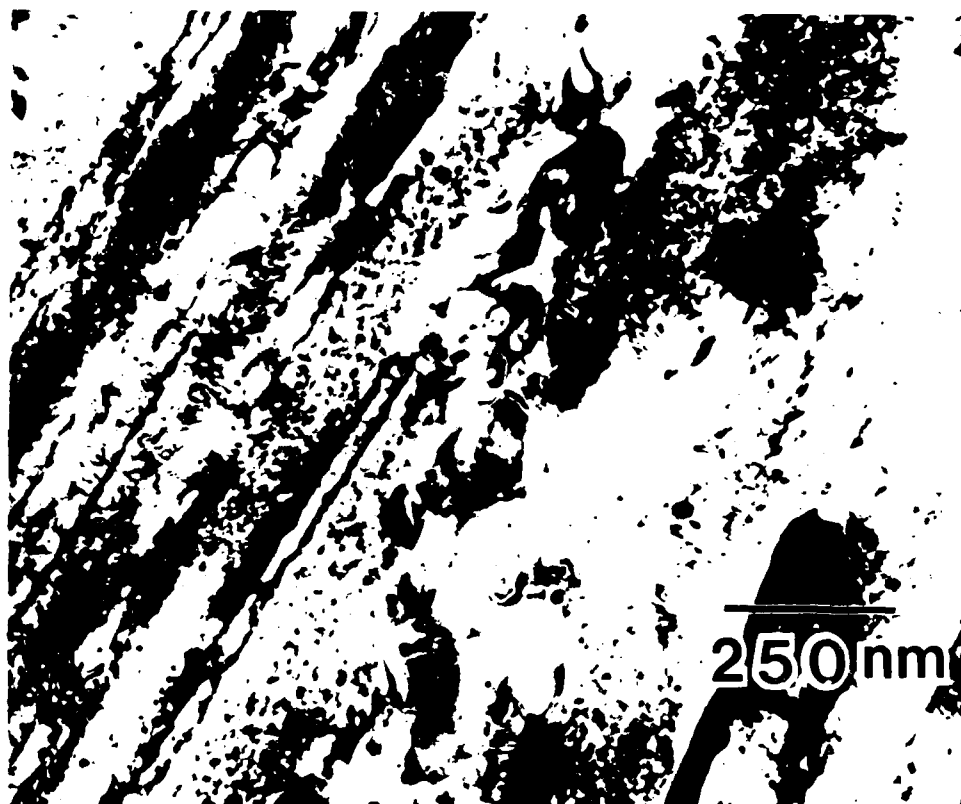
Fig. 48. Bright-field transmission electron micrograph of bands of Al$_6$Fe observed in the dynamically compacted and canless HIP'd Al-8Fe-2Mo ribbon particulate.

71

Fig. 49. Scanning electron micrographs of extruded-ribbon tensile specimen fracture surfaces tested at a) 20°C and b) 315°C.
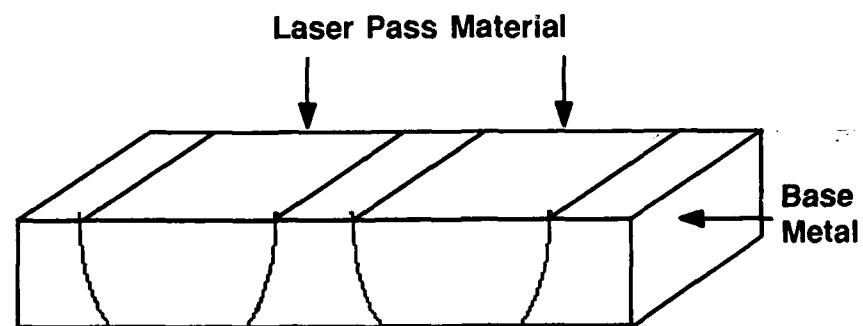
Fig. 50. Schematic diagram showing laser passes thinned for subsequent cold deformation or pressing.

Fig. 51. Bright-field transmission electron micrograph and associated SAD pattern of the microstructure of an Al-8Fe-2Mo laser pass which had been cold rolled to 65% and then heat treated at 400°C for 2 hours.

74

3.3 Mg Alloys

3.3.1 Microstructures and Mechanical Properties of Mg-Gd Alloys

Mg-20 wt% Gd alloys were prepared to study the aging and mechanical property behavior of Mg-rare earth alloys since these alloys offer attractive potential for high temperature applications. The as-cast microstructure of the allo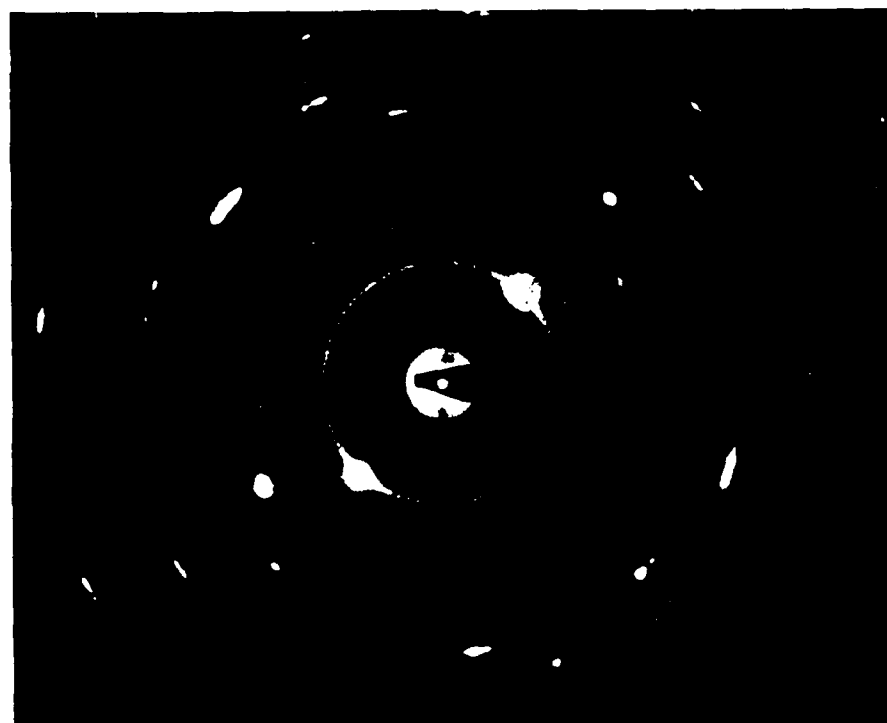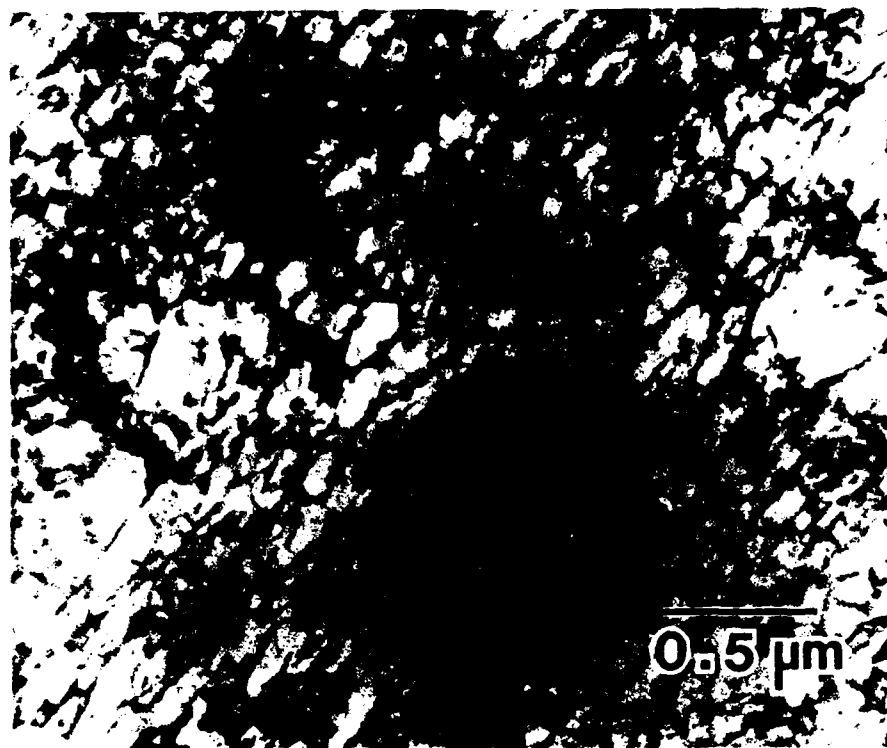y was dual phase with grains of α-magnesium and an intermetallic identified by analytical electron microscopy as $Mg_{24}Gd_5$ located along the grain boundaries (Fig. 52). The alloy was solution treated by holding at 538°C in the single phase α-magnesium region for 10 hours which was followed by a water quench. This heat treatment preserved the α-magnesium solid solution. The alloy slugs were then aged at 300°C and 350°C for various times. Microhardness data obtained from these specimens revealed that a hardness maximum occured for both aging temperatures after 2 hours, with the highest hardness values being achieved in the 300°C aged condition (Fig. 53). Examination of this alloy after aging revealed long thin precipitates within the matrix (Fig. 54). Convergent beam analysis of these precipitates identified them as $Mg_{24}Gd_5$. A precise crystallographic orientation relationship existed between the precipitates and the matrix, with three variants of the precipitate being observed. The orientation relation of the precipitates was determined to be $(0001)_{Mg}//(011)_{ppt}$ and $[2110]_{Mg}//[111]_{ppt}$. Three variants are possible with this relationship, which confirms the microstructural observations. For this orientation relationship and shared symmetry, the possible shapes for the precipitate are a pedion, a pinacoid, and a sphenoid, and the pinacoid, or platelet, is the structure observed in this system. The platelets grow along the [0001] directions on {0110} planes (Fig. 55). Short range ordering and metastable precipitates in Mg-rare earth alloys have been reported in the literature [44], with diffuse reflections appearing at $1/2 \ (0110)_{Mg}$ positions. These reflections may be due to either G. P. zones or the local ordering reported to occur in this system. Further work on this aspect is in progress. Test bars of the alloy were produced and tested at room and elevated temperature (Fig. 56). Mechanical property results from the testing of this alloy after heat-treatment revealed a large decrease in strength between alloys aged at 300°C and those aged at 350°C (Table 7). An examination of the microstructure showed that the precipitates in the alloy aged at 350°C were much more elongated than those aged at 300°C. Precipitates aged at 300°C had a aspect ratio (l/d) of ≈ 5, whereas those aged at 350°C had an aspect ratio of ≈ 20.1. In all cases, the alloys had low ductilities, which may have resulted from the large grain size in the test specimens. This behavior is common in cast magnesium alloys [45], and is controlled by additions of Zr to the alloy. This was not carried out in the case of the Mg-20wt%Gd alloys because the effects of Zr in this system is not known. The fracture surfaces of the specimens in general had the appearance of a brittle fracture, with some regions exhibiting local

Table 7

Mechanical Properties* of Mg-20 wt% Gd after Various Heat Treatments

Specimen	0.2%Y. S. (MPa)	U.T.S. (MPa)	%Elongation
as-cast	136.2	154.4	3.36
solution treated	72.3	157.0	7.47
aged at 300°C			
25°C	-	214.3	0.51
200°C	81.2	212.3	1.74
aged at 350°C			
25°C	-	139.6	0.52
200°C	82.5	195.0	0.94
HK31A-T6			
25°C	200.0	255.3	8.0
200°C	145.3	165.0	21.3

*The properties of commercial HK31A-T6 are included for comparison.

plasticity (Fig. 57). Coarse slip bands were observed on the surface of the test bars (Fig. 58), which result from deformation due to dislocation flow (slip) being localized on a few slip planes by the restricting action of the precipitates formed on aging. This may also be a contributing factor to the low observed ductilities in these alloys. The modulus of the Mg-20 wt% Gd alloys was also measured during testing and the values are given in Table 8. From Table 8, the addition of Gd to magnesium appears to lower the modulus.

Table 8

Elastic Modulus of Mg-20wt%Gd

Specimen	Temp. (°C)	E (GPa)
as-cast	25	41.6
solution treated	25	37.9
aged at 300°C	25	47.2
	200	40.6
aged at 350°C	25	41.8
	200	41.3
pure Mg	25	44.8

3.3.2 Microstructures of Mg-Li-Si Alloys

The material used in this study were produced by LithCo from 99.997% Mg and low-sodium lithium additions. The alloy compositions are shown in Table 9. The alloys were

Table 9

Compositions of the alloys chosen for use in this study.

Mg-5wt%Li	Mg-5 wt% Li-5wt%Si
Mg-8wt%Li	Mg-8wt%Li-5wt%Si
Mg-12wt%Li	Mg-12wt%Li-5wt%Si

resistance melted in an argon atmosphere and chillcast into 2.5 cm molds. The compositions were chosen to produce alloys from each of the three phase fields in the Mg-Li phase diagram, and the silicon concentration was determined from the results of previous studies on Al-Ni and Co alloys [46]. It was hoped that alloys containing ≈5 wt.% silicon could be undercooled sufficiently by rapid solidification to produce a refined coupled eutectic microstructure. The alloys were processed by laser surface melting (LSM), melt spinning to ribbon (MSR), and centrifugal atomization (CA) to achieve a rapidly solidified matrix. Helium was used as a cover gas during processing to both reduce oxidation and increase the rate of heat extraction. Specimens for heat-treating were encapsulated in quartz with a Ar-5%SiO$_2$ atmosphere. The specimens were then examined using optical microscopy, x-ray diffractometry, scanning electron microscopy, and transmission electron microscopy. Specimens for transmission electron microscopy were prepared using two different methods. Those alloys containing silicon were ion-milled using an argon beam, whereas those without silicon additions were jet electropolished. Scanning electron microscopy was carried out using a Jeol 35-C, and both Phillips 420T analytical and 430 analytical electron microscopes were used for the transmission work. X-ray diffraction analysis was conducted on a Rigaku/D-max scanning diffractometer.

Optical micrographs of the alloys are shown in Figs. 59a-f. The Mg-5wt%Li alloy had some eutectic present at the grain boundaries in the as-cast condition, but after holding the alloy at 500°C for 12 hours and furnace cooling only α-magnesium remained. The eutectic Mg-8wt%Li had the appearance of a divorced eutectic, with α platelets in a β matrix (Fig. 59c). Upon examination of the β matrix, it was found that a regular array of α lamellae were present (Fig. 60). This behavior has been previously reported for alloys slightly richer in lithium [47]. At present a consistent crystallographic relationship has not been determined for the lamellae. The Mg-12wt%Li alloy was free of α; the apparent precipitate phase on the micrograph shown is an artefact

77

produced by water pick-up on the newly polished surface. The alloys containing silicon were all hypereutectic, and contained large primary Mg_2Si crystals and an irregular, almost script-like eutectic. The main effect of the silicon was to greatly reduce the average grain size of the alloys; from 65µm to 12µm for the 5wt%Li alloy, and 630µm to 35µm for the 12wt%Li alloy. The morphology of the matrix was also cellular in the silicon containing alloys. The appearance of the Mg-8wt%Li-5wt%Si was completely different from that of the alloy without silicon. The α phase formed around the primary Mg_2Si crystals, and an irregular collection of α, β, and eutectic Mg_2Si formed in the region between these crystals (Fig. 59d). The large platelets and divorced eutectic structure present in the binary was totally absent. The grain size in the binary Mg-12wt%Li alloy had been decreased by the addition of silicon (Figs. 59e,f). This was attributed to the nucleation of β grains on the hypereutectic Mg_2Si crystals. It was also observed that the primary silicide crystals contained a fine granular substructure which tended to crumble when polished. This was attributed to the presence of Li, as the effect increased with the Li content, and primary crystals in a binary Mg-5wt%Si alloy did not exhibit this behavior.

The surface of the rapidly solidified melt pools was rough and rippled, but no evidence of cracking was observed in any of the alloys. There was little effect of LSM on the binary α and β alloys. The only noticeable effect was at the melt pool interface, where any grain boundary intersected by the melt pool had rotated and grown into the melt pool perpendicular to the interface and parallel to the heat extraction direction (Fig. 61). The microstructure of the Mg-8wt%Li alloy still consisted of α and β platelets, but their average size had been reduced by a factor of ≈ 100 (Fig. 62). At higher magnification there was no evidence of α precipitation in the β regions, the α platelets had a definite orientation relationship with the β phase (Figs. 63a,b). The relationship observed: $(0001)_\alpha//(110)_\beta$, $(1210)_\alpha//(111)_\beta$, and $[1010]_\alpha//[112]_\beta$ has also been reported in directionally solidified material [48]. This relationship is the Burgers relationship [49] and is one of the two standard bcc-hcp relationships. The primary Mg_2Si crystals contained in the Mg-Li-Si alloys were refined by the LSM treatment, but not to the degree expected. Three regions were observed in each specimen, the unmelted base material, the interface region where only the matrix had melted and then resolidified into a refined eutectic trapping primary unmelted Mg_2Si, and the central portion of the melt pool, where all the material was molten prior to solidification (Fig. 64). The large size of the crystals in the melt pool may possibly be due to small unmelted Mg_2Si particles which were carried into the melt pool from the interface region and acted as nuclei for the solidification of the hypereutectic Mg_2Si crystals. The growth facets present on the Mg_2Si crystals in the melt pool corresponded to $\{111\}_{Mg_2Si}$ type planes (Fig. 65) and the growth directions to the $\{100\}_{Mg_2Si}$ directions. In the Mg-8wt%Li alloy containing silicon additions, the α formed in

Table 10

Microhardness* of the laser treated alloys.

Alloy	As-cast	Laser treated
Mg-5wt%Li	40.8	55.7
Mg-5wt%Li-5wt%Si	51.1	74.1
Mg-8wt%Li	42.8	71.2
Mg-8wt%Li-5wt%Si	59.9	68.4
Mg-12wt%Li	39.6	42.1
Mg-12wt%Li-5wt%Si	49.4	69.8
Mg	43.4	-----

*A knoop indenter and a 100 gram load were used. The values have a standard deviation of   ±2.3 .

cells around the Mg_2Si, and the β formed between these cells. In each alloy a fine eutectic also formed (Fig. 66). The eutectic itself was irregular but uniformly dispersed throughout the melt pool. Microhardness measurements on the melt pools of the various alloys were made, and the results are shown in Table 10. The results show that the refined silicide dispersion produced by rapid solidification processing does increase the hardness of the alloy; however, the large size of the primary hypereutectic Mg_2Si crystals is expected to still limit the tensile propertiesof the alloy.

A superheat of 250°C was used during melt spinning to eliminate the possibility of any unmelted Mg_2Si particles affecting the solidification structure in the ribbon. The ease of melt spinning and surface condition of the ribbon increased with increasing silicon content. The as-spun microstructure of the Mg-8wt%Li alloy is shown in Fig. 67. The microstructure is predominately α, with small grains of β dispersed throughout the matrix. Silicon additions again resulted in the formation of crystals of Mg_2Si, although on a finer scale than in the LSM alloy (Fig. 68), and the volume fraction of fine Mg_2Si eutectic had increased. Upon aging this microstructure for 2 hours at 300°C, fine irregular precipitates formed in the matrix; the primary Mg_2Si crystals also appeared to have spheroidized after this heat treatment. After 2 hours at 500°C the uniform matrix of α, β, or α/β, depending on the alloy composition, contained large Mg_2Si precipitates (Fig. 69). In an attempt to produce a more uniform dispersion of silicide in the matrix, several binary Mg-Si alloys with lower concentrations of silicon were melt spun. The melt spun ribbon of the Mg-2.75wt%Si alloy was very brittle despite having a coupled eutectic microstructure. (Fig. 70). This microstructure was unaffected by a 2 hour 300°C anneal, but after

79

a 2 hour 500°C anneal it was indistinguishable from the melt spun Mg-Li-Si alloys which had been subjected to the same treatment. Further processing of alloys using lower silicon contents is now being carried out in an attempt to obtain the coupled eutectic mictostructure in Mg-Li-Si alloys.

Two alloys were centrifugally atomized, namely Mg-8wt%Li and Mg-8wt%Li-1.5wt%Si. This silicon content was chosen to produce a fine dispersion of silicide yet retain some ductility. The α phase, β phase, and in the silicon containing alloy the Mg_2Si phase, were all detected in x-ray powder patterns. The 2θ position of the diffraction peaks for the α phase had increased. Lithium in solid solution in α-magnesium decreases the lattice parameter, which would increase the 2θ angle. The increase in the 2θ angle was greater in rapidly solidified Mg-8wt%Li powder when compared to Mg-5wt% powder processed using the same techniques. This increase was attributed to a metastable supersaturation of lithium in the α-magnesium matrix.

The powder was then dynamically compacted and the microstructure examined. The compacts were fully dense after compaction, and it has been shown that although dynamic compaction plastically deforms the matrix, it does not affect the basic microstructure of the powder [42]. The microstructure of the binary alloy contained both α and β grains randomly distributed throughout the matrix (Fig. 71a). No rational orientation relationship between the α and β phases in the powder was observed. The Mg-8wt%Li-1.5wt%Si alloy had small Mg_2Si rods at the boundaries of α cells (Fig. 71b). Small β grains were located at the grain boundaries, and a few were also located within the cells. Optical micrographs show that both the alloys had refined microstructures, with regions of local melting at the powder-powder interfaces (Figs. 72a,b). The compacts were subsequently heat treated for 2 hours at 300°C. After the heat treatment, the α and β phases had coarsened significantly in the binary alloy (Fig. 72c), whereas only slight changes were observed in the silicon containing alloy (Fig. 72d). The regions in the binary alloy which were melted during the compaction process are much more refined after heat treatment compared to the bulk of the material. The reason for this behavior is not known, but it is possible that oxide from the surface of the powder is mixed into the melted region during compaction and this oxide suppresses the growth of the α and β grains much like the silicide dispersion in the silicon containing alloys. Microhardness values obtained from the as-compacted and heat treated material show that the alloy containing silicon retains a greater percentage of as-compacted hardness after heat treatment than the binary alloy. Hardness values for the binary alloy Mg-8wt%Li are 61.7 as-compacted and 47.8 after the heat treatment, or 77% of the as-compacted value. Hardness values for the Mg-8wt%Li-1.5wt%Si alloy are 65.4 as-compacted and 57.5 after heat treatment, or 87.9% of the compacted value. From the data it appears that the silicide dispersion acts as an effective barrier to the growth of the α and β phases. The α/β alloy and the compaction and heat treating behavior of Mg-12wt%Li alloys with additions of silicon is presently under investigation.

Fig. 52. As-cast microstructure of Mg-20wt%Gd. The phase located at the grain boundaries has been identified as $Mg_{24}Gd_5$.
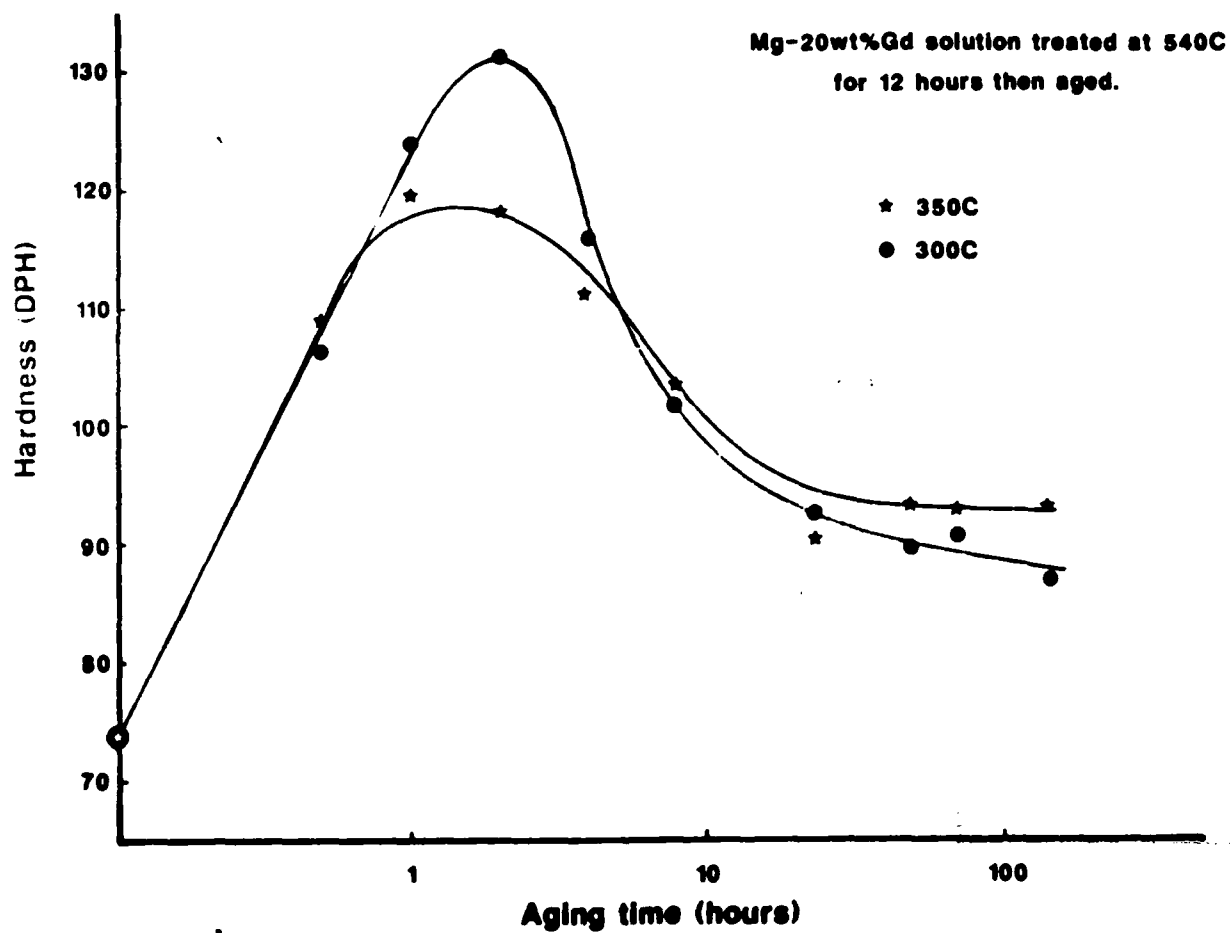
Fig. 53. Microhardness data for solution treated Mg-20wt%Gd aged at 300°C and 350°C. Both heat treat conditions show a peak hardness after a two hour age.

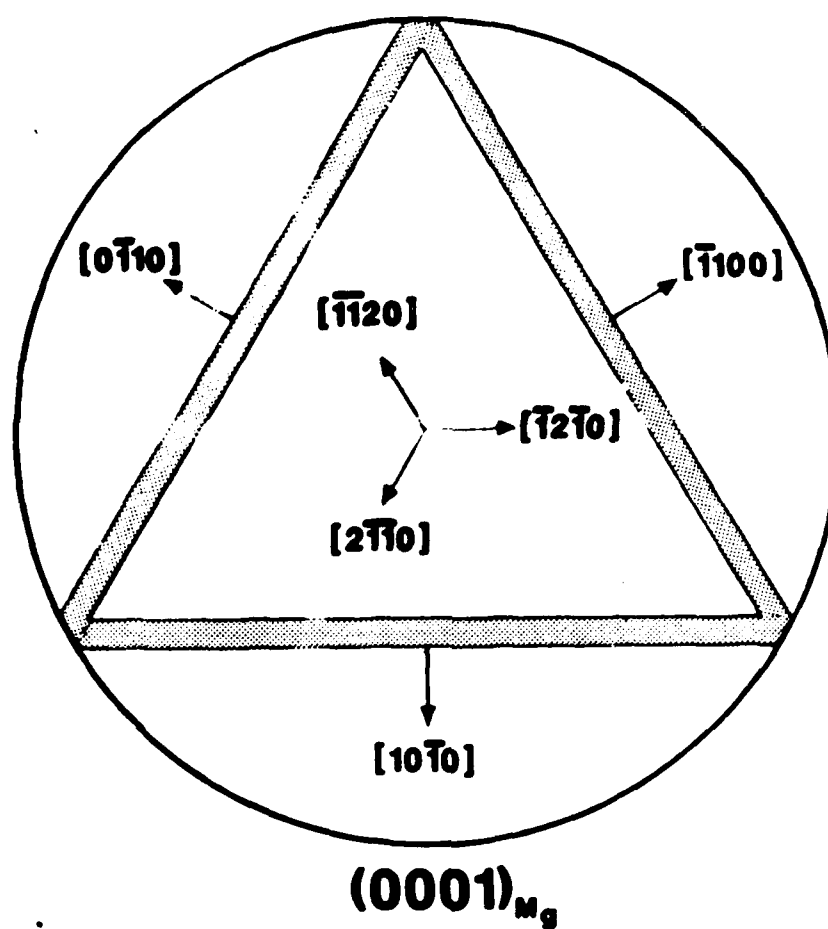Fig. 54. Precipitates formed in solution treated Mg-20wt%Gd after two hours at 400°C.

Fig. 55. Schematic diagram of the crystallography of precipitation of $Mg_{24}Gd_5$ in magnesium.

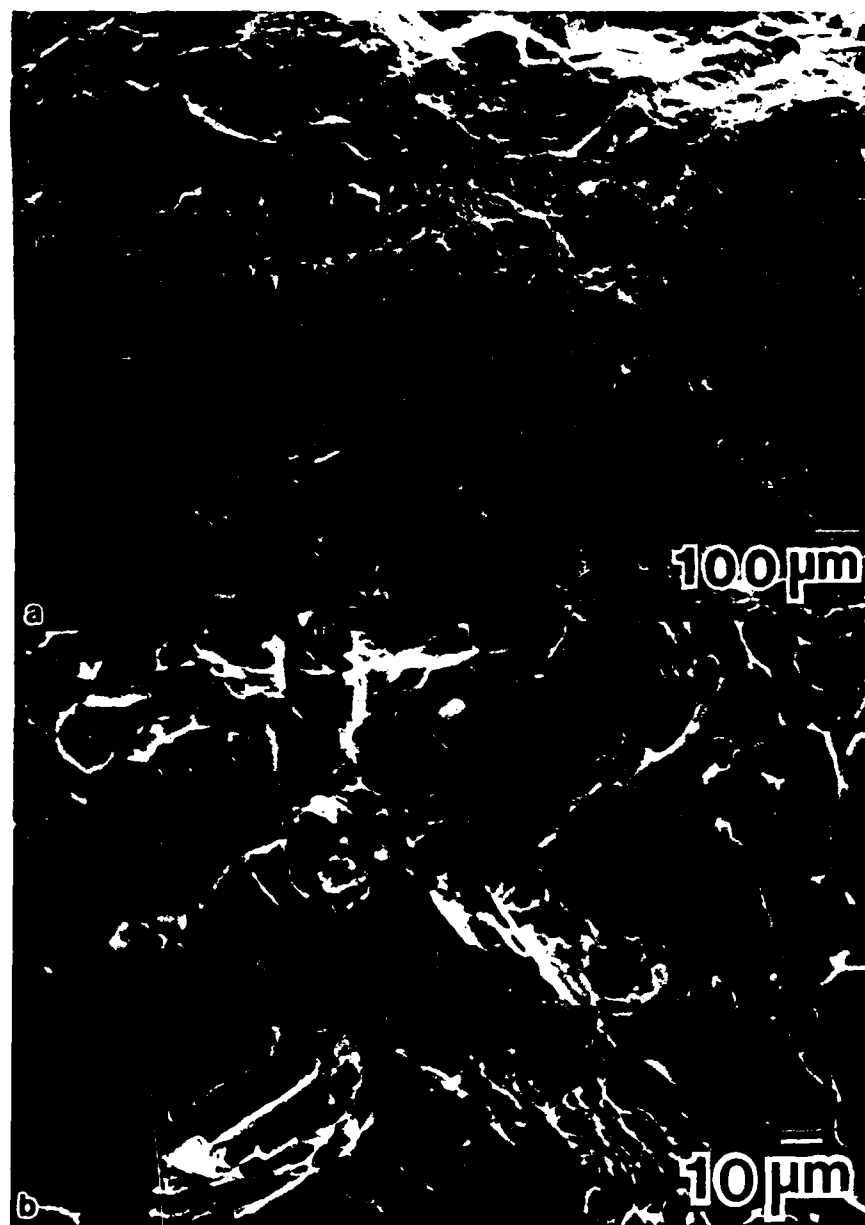Fig. 56. Tensile test bars used to determine tensile data for Mg-20wt%Gd.

Fig. 57. Fracture surface of specimen aged at 300°C for two hours. Testing temperature;
a) room temperature b) 200°C.

Fig. 58. Slip band on the surface of a tensile bar heat treated at 300°C for two hours and then tested at room temperature.
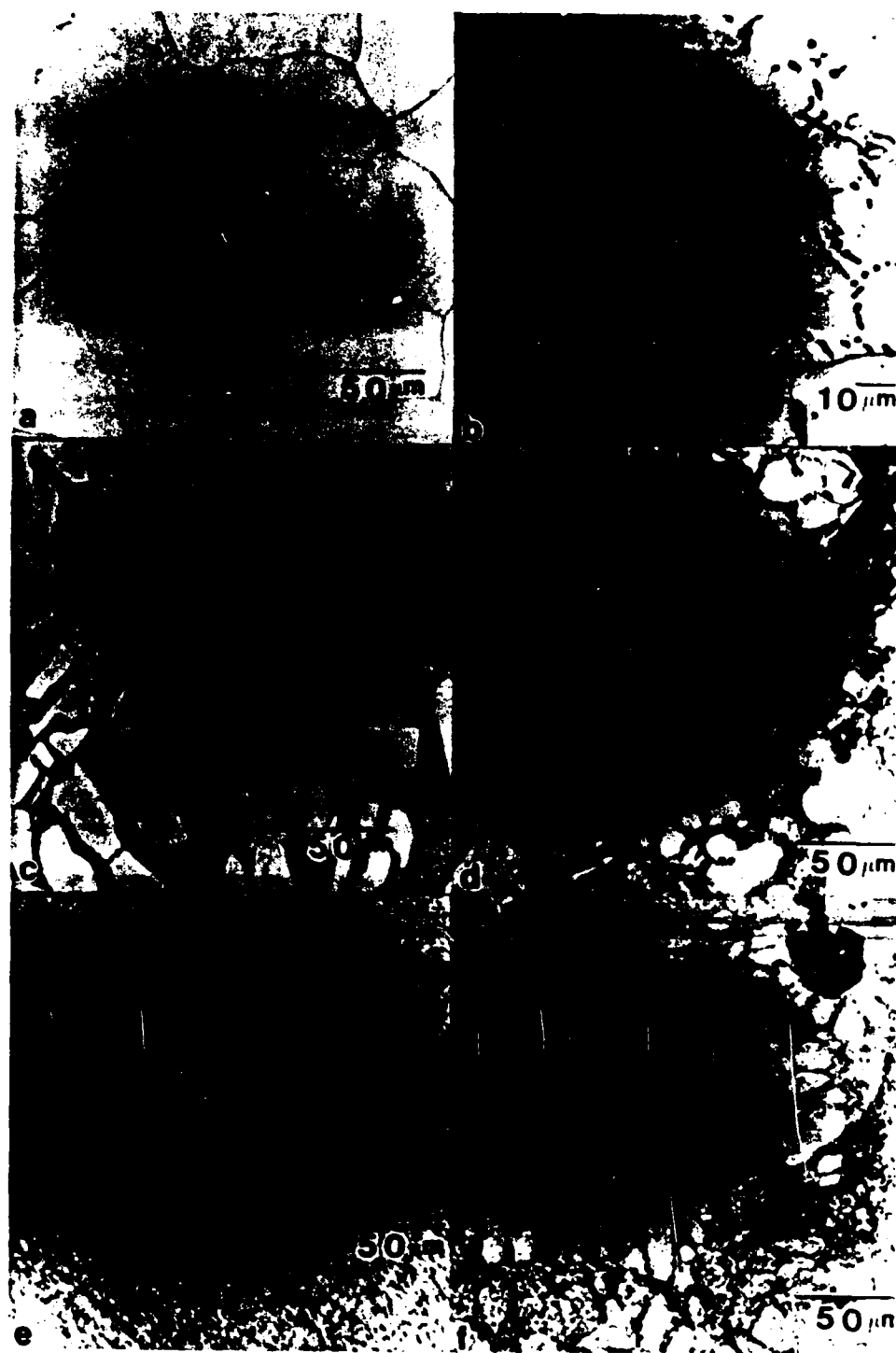
Fig. 59. As cast microstructures of Mg-Li and Mg-Li-Si alloys used in this study; a) Mg-5Li
b) Mg-5Li-5Si c) Mg-8Li d) Mg-8Li-5.2Si e) Mg-12Li f) Mg-12Li-5.4Si
All compositions are given in weight percent.

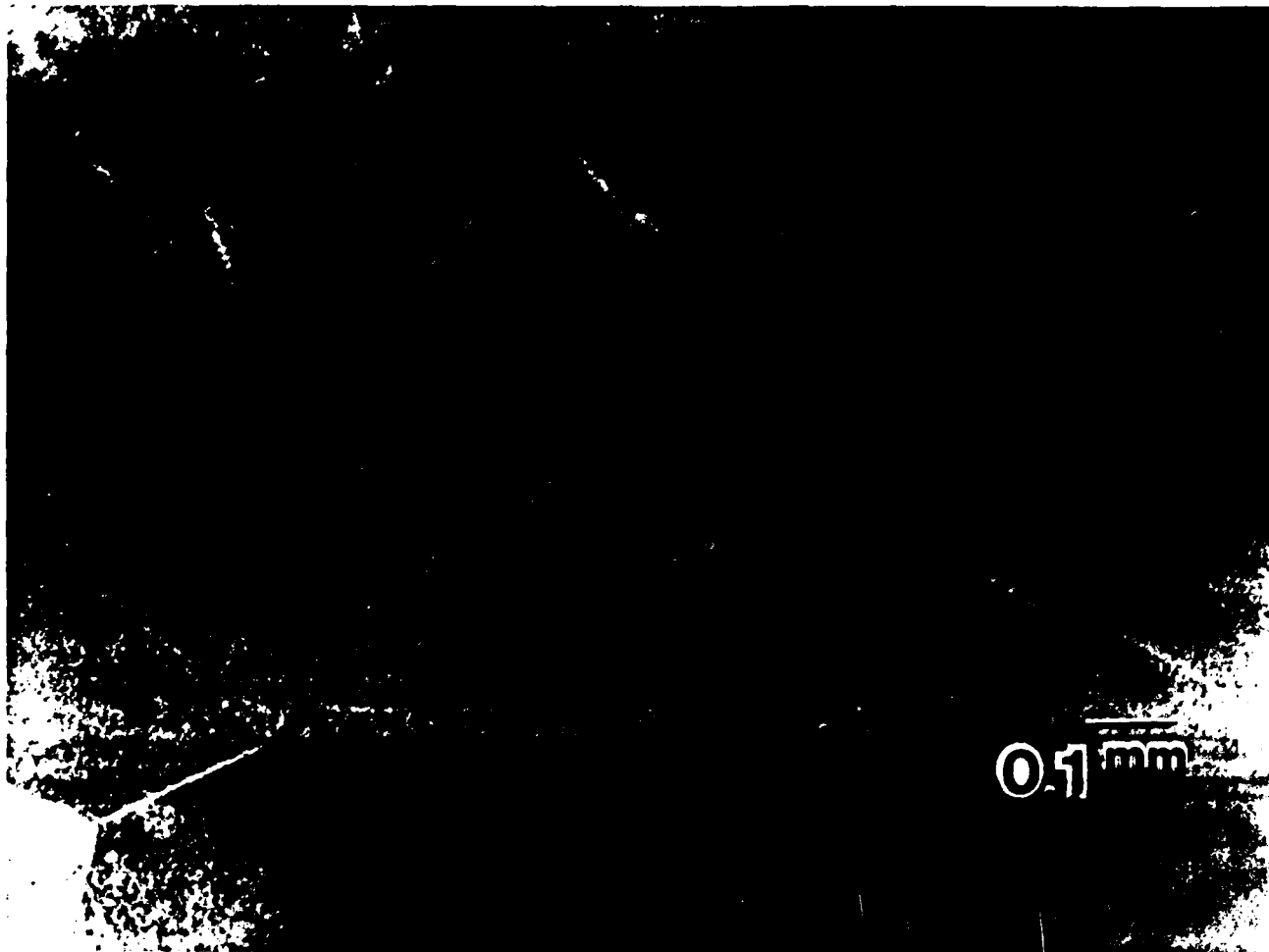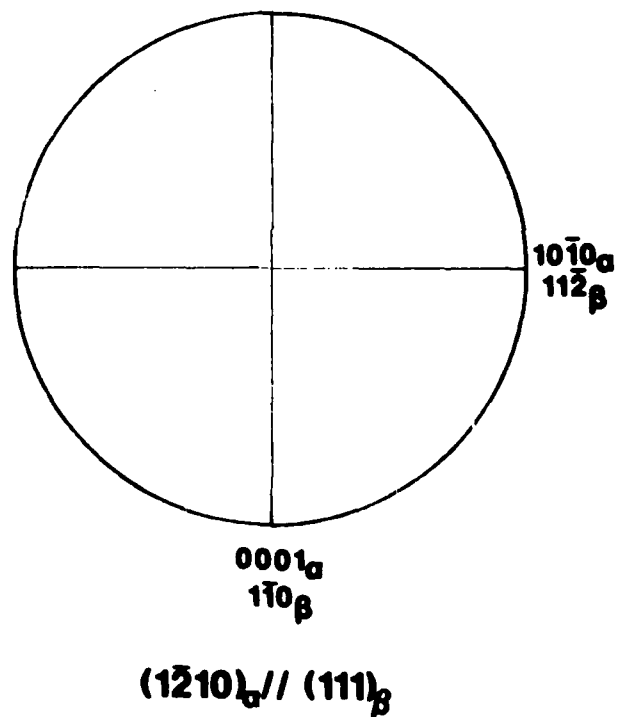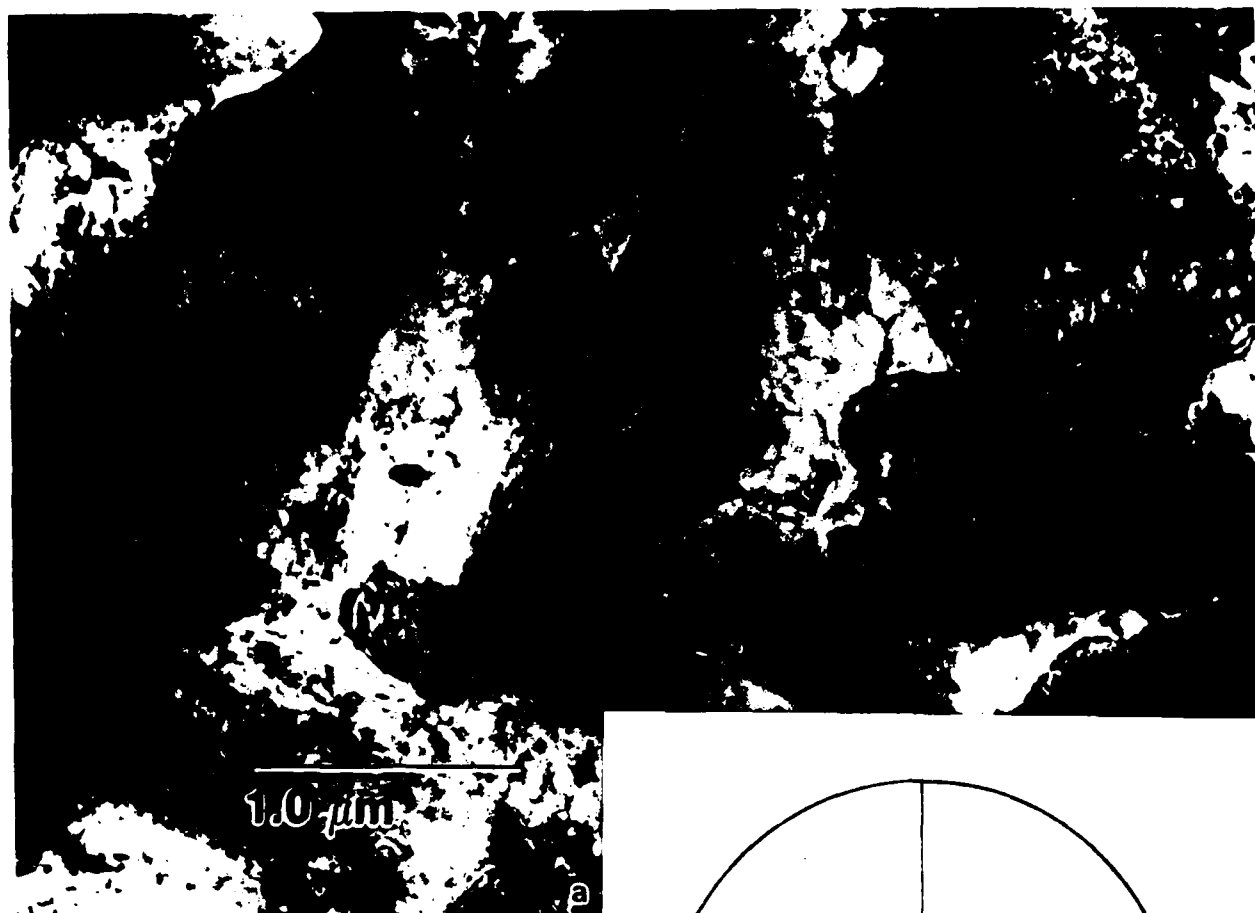Fig. 60. α lamellae in the β grains of as-cast Mg-8Li.

Fig. 61. Melt pool in laser surface melted Mg-12Li. Note the rotation of the grain boundaries at the melt pool interface.

Fig. 62. Microstructure of laser surface melted Mg-8Li.

Fig. 63. a) Microstructure of laser treated Mg-8Li alloy. b) Stereographic projection corresponding to the orientation relationship observed between the α and β phases in the laser treated material.
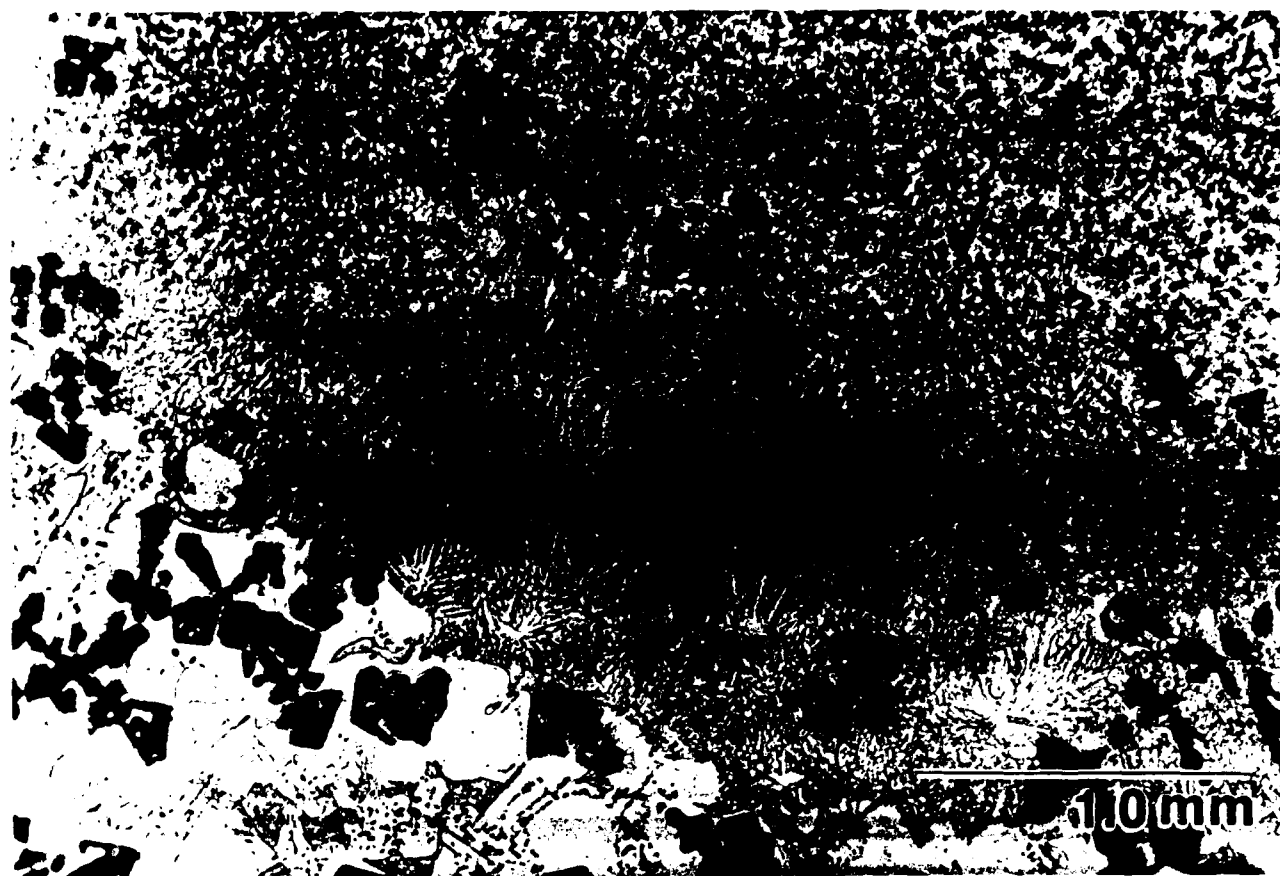
Fig. 64. Interface region of the melt pool in laser treated Mg-8Li-5.2Si.
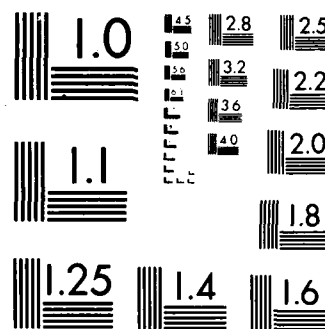
MICROCOPY RESOLUTION TEST CHART

NATIONAL BUREAU OF STANDARDS 1963-A

Fig. 65. Growth facets on Mg_2Si crystals found in the melt pool of Mg-5Li-5Si. The facets are parallel to {111} planes of Mg_2Si.
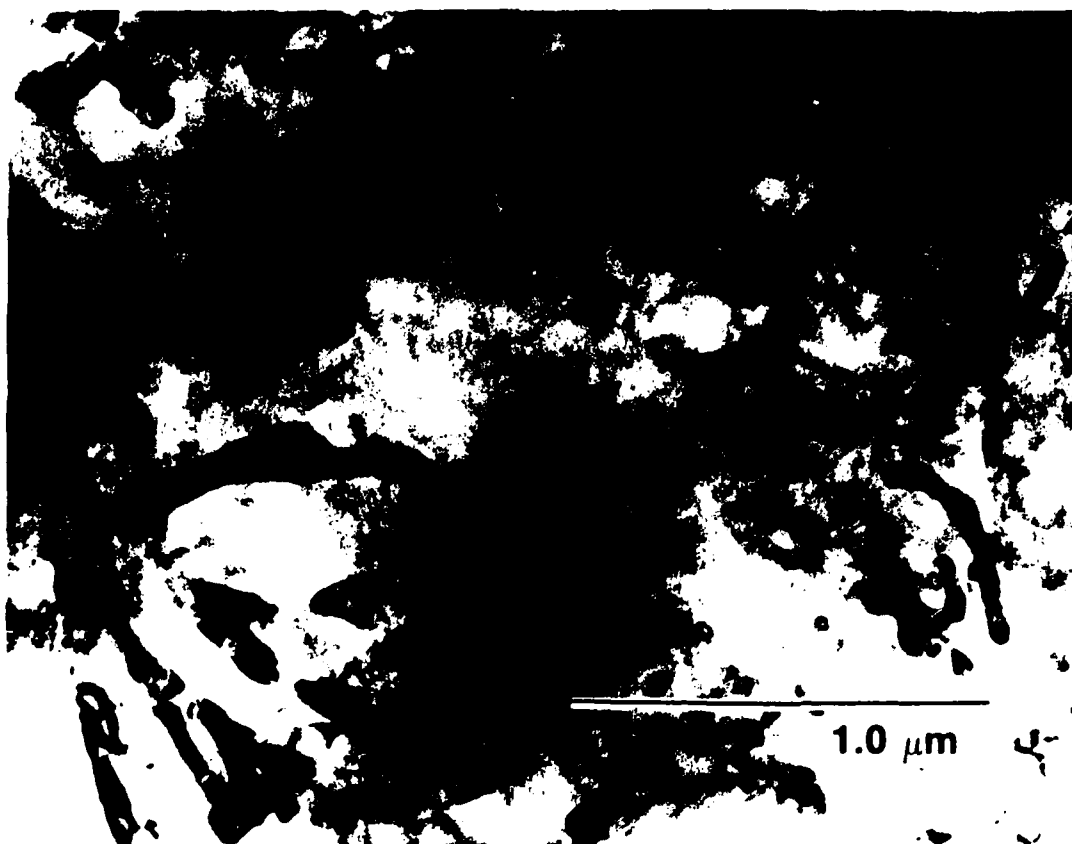
Fig. 66. Fine eutectic structure (between α or β and Mg_2Si) formed in the matrix of alloys containing silicon.

Fig. 67. Microstructure of melt spun Mg-8Li.
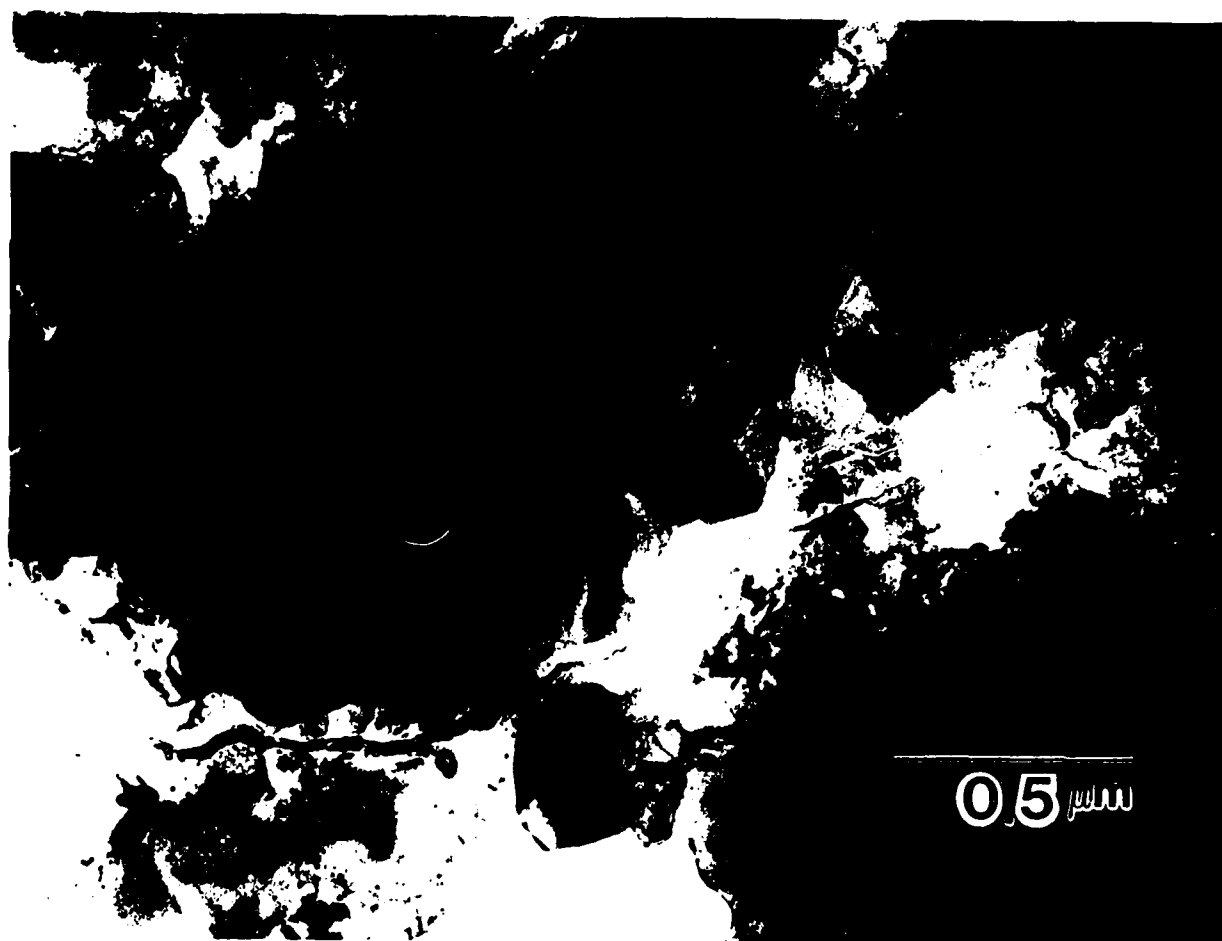
Fig. 68. Microstructure of melt spun Mg-5Li-5Si. The large crystals are primary Mg_2Si.
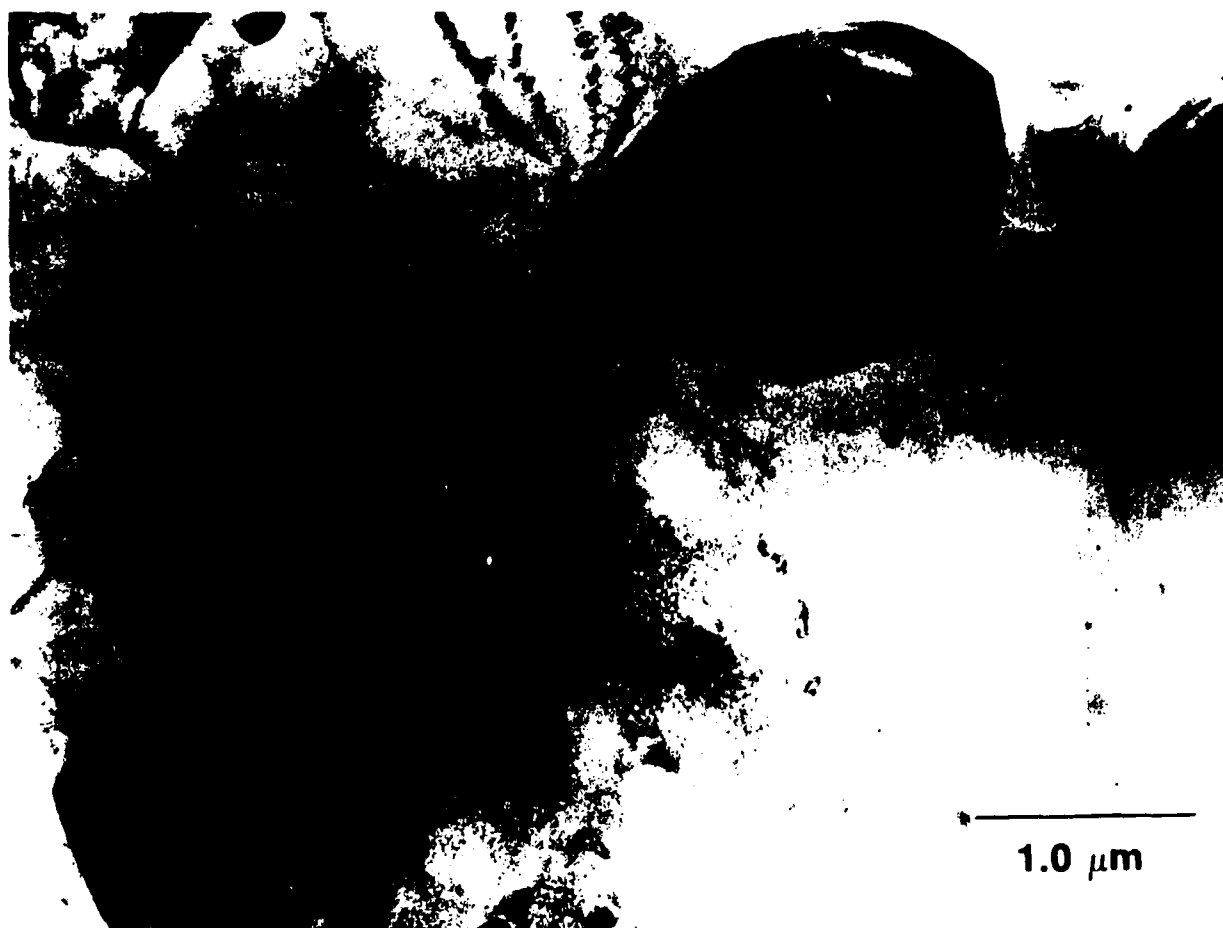
Fig. 69. Microstructure of melt spun Mg-5Li-5Si aged for two hours at 500C. The silicide has completely coarsened.

Fig. 70. Melt spun Mg-2.75Si showing a coupled eutectic microstructure.

Fig. 71. Centrifugally atomized Mg-8Li (a) and Mg-8Li-5Si (b).
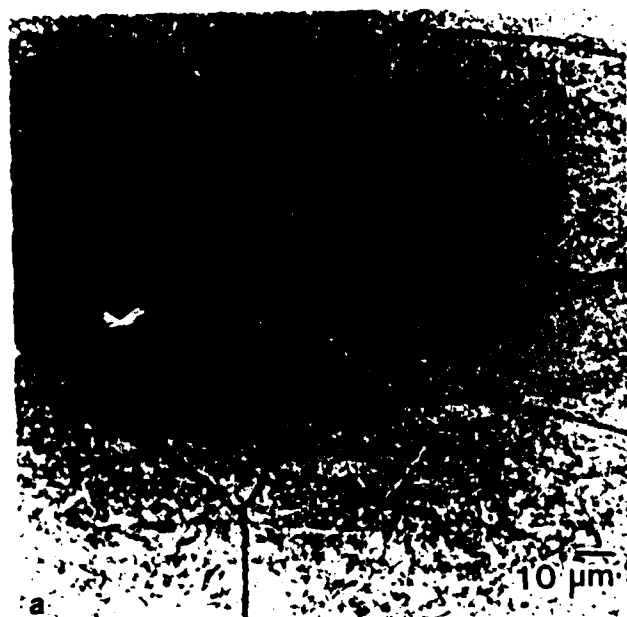
Fig. 72. Microstructure of dymanically compacted Mg-8Li and Mg-8Li-5.2Si powders.
  a) as compacted Mg-8Li b) aged two hours at 300°C
  c) as compacted Mg-8Li-5.2Si d) aged two hours at 300°C

4. FUTURE WORK

a. Determination of the crystallography and composition of the precipitates in heat-treated Al-8Fe-2Mo-Si alloys using analytical electron microscopy and x-ray diffraction.
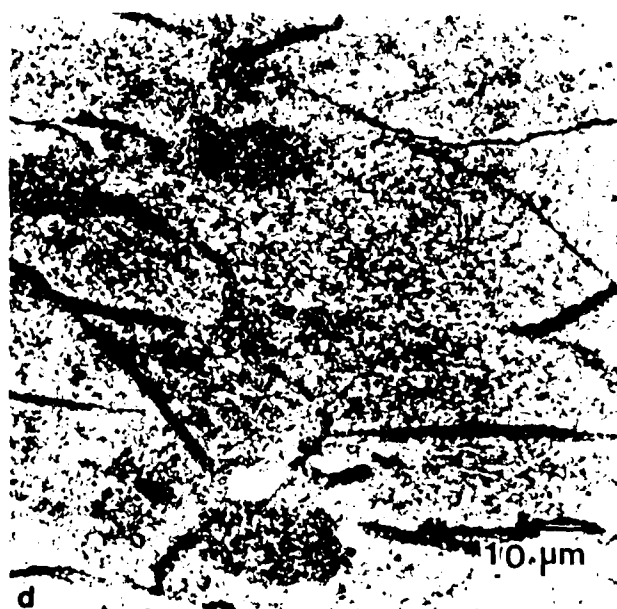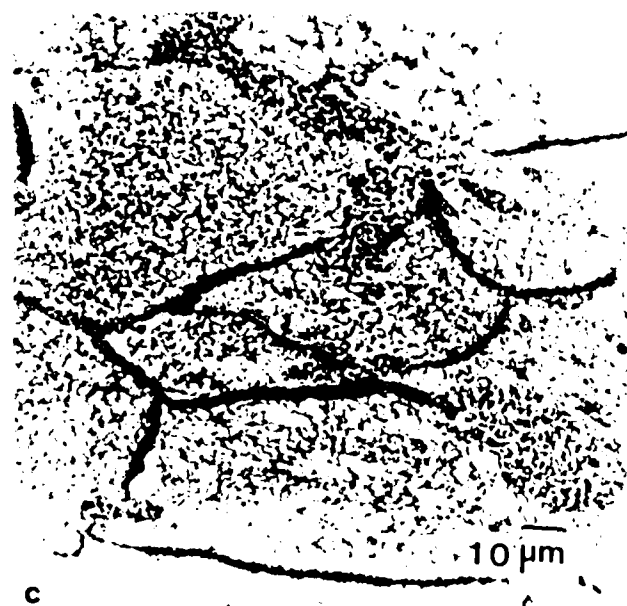
b. Determination of the mechanical properties of rapidly solidified and extruded Al-8Fe-2Mo-Si alloy ribbon.

c. Studies of dislocation-particle interactions in Al-8Fe-2Mo-Si alloys to establish the strengthening mechanism.

d. Consolidation and characterization of Al-8Fe-2Mo ribbon by the hybrid process of dynamic compaction followed by HIP.

e. Determination of the mechanical properties and thermal stability of consolidated Al-8Fe-2Mo ribbon.

f. Modifications in the matrix lattice parameter and precipitate phase morphology in Mg-20wt.%Gd by additions of Ag and Pb.

g. Studies of the rapid solidification behavior of binary Mg-Si alloys to determine the optimum composition for rapid solidification processing.

h. Production and consolidation of atomized powders of α and β Mg-Li alloys with and without silicon.

5. PRESENTATIONS FROM THIS PROGRAM

"Microstructural Decomposition of Rapidly Solidified Particulate During Consolidation," D. J. Miller and H. L. Fraser, at the 115th TMS annual Meeting, March 2-6, 1986, New Orleans, La.

"Microstructure and High Temperature Properties of a Mg-20wt%Gd alloy," F. C. Grensing and H. L. Fraser, at the 115th TMS annual Meeting, March 2-6, 1986, New Orleans, La.

"Growth of the Solid Phase in the Presence of a Liquid Miscibility Gap for Highly Undercooled Single Phase Alloys," D. C. Van Aken and H. L. Fraser, at the 115th TMS annual Meeting, March 2-6, 1986, New Orleans, La.

"Microstructure and Properties of Rapidly Solidified Magnesium Lithium Alloys," F. C. Grensing and H.L. Fraser, at Materials Week '86 TMS/AIME Fall Meeting, October 6-9, 1986, Orlando, Fl.

"Microstructure and Properties of Rapidly Solidified Material Consolidated by Dynamic Compaction and Hot Isostatic Pressing," D. J. Miller and H.L. Fraser, at Materials Week '86 TMS/AIME Fall Meeting, October 6-9, 1986, Orlando, Fl.

PUBLICATIONS FROM THIS PROGRAM

"Microstructure of Rapidly Solidified Al-In Alloys," D. C. Van Aken and H. L. Fraser, submitted to the Int. J. of Rapid Solid., in press.

"Microstructure and Properties of Rapidly Solidified Magnesium Lithium Alloys," F. C. Grensing and H.L. Fraser, in "Proceedings of the Fall Meeting TMS/AIME '86",at Materials Week '86 TMS/AIME Fall Meeting, October 6-9, 1986, Orlando, Fl.

"Microstructure and Properties of Rapidly Solidified Material Consolidated by Dynamic Compaction and Hot Isostatic Pressing," D. J. Miller and H.L. Fraser, in "Proceedings of the Fall Meeting TMS/AIME '86", at Materials Week '86 TMS/AIME Fall Meeting, October 6-9, 1986, Orlando, Fl.

Doctor of Philosophy Degrees supported by program but not yet completed:

Consolidation of Rapidly Solidified Particulate; Dean J. Miller

Microstructural Enhancement of Magnesium Alloys Containing Lithium and Rare Earth Additions; Fritz C. Grensing

6. REFERENCES

1. R.S. Leigh, *Phil. Mag.*, 42, p.139 (1951).

2. B. Nobel, S. J. Harris and K. Dinsdale, *J. Mater. Sci.*, 17, p. 461 (1982).

3. N. Dudzinski, J. R. Murray, B. W. Mott and B. Chalmers, *J. Inst. Metals*, 74, p. 291 (1948).

4. N. Dudzinski, *J. Inst. Metals*, 81, p. 49 (1952-53).

5. N. Dudzinski, *J. Inst. Metals*, 83, p. 444 (1954-55).

6. B. Paul, *Trans. AIME*, 218, p. 36 (1960).

7. Z. Hashin and S. Shtrikman, *J. Mech. Phys. Solids*, 11, p. 127 (1963).

8. R. J. Scaeffer, M. Rosen, J. J. Smith, D. Shechtman and R. Mehrabian, In: *Rapid Solidification Processing, Principles and Technologies III*, R. Mehrabian, ed., NBS, Gaithersburg, MD, p. 397 (1982).

9. D. C. Van Aken and H. L. Fraser, *Acta Metall.*, 33, p. 963 (1985).

10. J. W. Zindel, D. C. Van Aken, R. D. Field, P. Kurath and H. L. Fraser, In: *Proceedings of Symposium on Mechanical Behavior of Rapidly Solidified Materials*, S. M. L. Sastry and B. A. Macdonald, eds., AIME, Warrendale, PA, p. 189 (1985).

11. C. M. Adam, R. G. Bourdeau and J. W. Broch, Application of Rapidly Solidified Alloys, *AFWAL Final Report No. AFWAL-TR-81-4112*, Contract No. F33615-76-C-5136 (1982).

12. H. Jones, *Mater. Sci. Engr.*, 5, p. 1 (1969-70).

13. C. M. Adam, In: *Rapidly Solidified Amorphous and Crystalline Alloys*, B. H. Kear, B. C. Giessen and M. Cohen, eds., Elsevier, New York, 8, p. 411 (1982).

14. J. W. Zindel, J. T. Stanley, R. D. Field and H. L. Fraser, In: *Rapidly Solidified Powder Al Alloys, ASTM STP 890*, M. E. Fine and E. A. Starke, Jr., eds., ASTM, Philadelphia, p. 186 (1986).

15. J. W. Zindel, R. D. Field, P. Kurath and H. L. Fraser, In: *Aluminum Alloys: Their Physical and Mechanical Properties*, E. A. Starke, Jr. and T. H. Sanders, eds., Chameleon Press, London, p. 288 (1986).

16. R. E. Sanders, Jr. and G. J. Hildeman, Elevated Temperature Al-Alloy Development, *AFWAL Final Report No. AFWAL-TR-81-4076*, Contract No. F33615-77-C-5086 (1981).

17. R. D. Field, J. W. Zindel and H. L. Fraser, *Scripta Metall.*, 20, p. 415 (1986).

18. H. L. Fraser, Rapid Solidification Processing and Powder Metallurgy of Al Alloys, *AFOSR Final Technical Report No. AFOSR-82-0186* (1986).

19. S. K. Das, *Oral Presentation*, Westec, Los Angeles, CA (1986).

20. A. M. Brown et al., In: *Aluminum Alloys: Their Physical and Mechanical Properties*, E. A. Starke, Jr. and T. H. Sanders, eds., Chameleon Press, London, p. (1986).

21. D. J. Skinner, R. L. Bye, D. Raybould and A. M. Brown, *Scripta Metall.*, 20, p. 867 (1986).

22. National Materials Advisory Board, Commission on Engineering and Technical Systems, *Rapid Solidification Processing: Status and Facilities Final Report*, Publication NMAB-401, National Academy Press, Washington, D.C. 1982

23. J. E. Morgan and B. L. Mordike, *Metal. Trans. A*, 12A, p. 1581 (1981).

24. M. E. Drits, L. L. Rokhlin, A. A. Oreskina and N. I. Nikitina, *Russ. Met.*, 5, p. 83 (1982).

25. L. A. Carapella, *Met. Progress*, 14, p. 297 (1945).

26. A. A. Nayeb-Hashemi, J. B. Clark and A. D. Pelton, *Bulletin of Alloy Phase Diagrams*, 5 (4), p. 365 (1984).

27. F. E. Hausen, P. R. Landon and J. E. Dorn; *Trans. Am. Soc. Metals*, 50, p. 856 (1958).

28. A. Urakami, M. Meshii and M. E. Fine, *Acta Met.*, 18, p. 87 (1970).

29. A. Ahmadieh, J. Mitchell and J. E. Dorn, *Trans. Met. Soc. AIME*, 233, p. 1130 (1965).

30. R. E. Lee and W. R. D. Jones, *J. Mat. Sci.*, 9, p. 469 (1974).

31. W. R. D. Jones and G.V. Hogg, *J. Inst. Metals*, 85, p. 255 (1956-57).

32. A. Saia and R. E. Edelman, *Modern Castings*, 80, p. 686 (1964).

33. A. A. Nayeb-Hashemi and J. B. Clark, *Bulletin of Alloy Phase Diagrams*, 5 (6), p. 584 (1984).

34. D. C. Van Aken, Ph.D. Thesis, University of Illinois, Urbana (1986).

35. J. L. Murray, *Unpublished Research*, NBS.

36. J. W. Cahn and G. Kalonji, In: *Solid-Solid Phase Transformations*, H. I. Aaronson, D. E. Laughlin, R. F. Sekerka and C. M. Wayman, eds., AIME, Warrendal, PA, p. 3 (1982).

37. W. E. Mayo and T. Tsakalakos, *Met. Trans.*, 19, p. 481 (1971).

38. D. C. Van Aken, D. J. Miller, P. Kurath and H. L. Fraser, *To be Published*.

39. P. Furrer and H. Warlimont, *Z. Metallk.*, 64, p. 236 (1973).

40. M. H. Jacobs, A. G. Doggettt and M. J. Stowell, *J. Mater. Sci.*, 9, p. 1637 (1974).

41. J. W. Steeds, In: *Introduction to Analytical Electron Microscopy*, J. J. Hren, J. I. Goldstein and D. C. Joy, eds., Plenum Press, New York, p. 387 (1979).

42. D. J. Miller and H.L. Fraser, Conference procedings of the Fall Meeting AIME., Orlando, Fl., In press, Oct. 1986.

43. L. M. Barker, In: *Fracture Mechanics Thirteenth Conference, ASTM STP 743*, R. Roberts, ed., ASTM, Philadelphia, p. 456 (1981).

44. D.S. Gencheva, A.A. Katsnel'son, L. L. Rokhlin and V. M. Silonov, *Fiz. Met. Metalloved.*, 51 (4), p. 788 (1981).

45. E. F. Emley, *Principles of Magnesium Technology*, Pergamon Press, New York, p. 787 (1976).

46. J. T. Stanley, R. D. Field and H. L. Fraser, In: *"Aluminum Alloys, Their Physical and Mechanical Properties "*, E. A. Starke Jr. and T. H. Sanders Jr., eds., Chameleon Press, London, p. 307 (1986).

47. A. Alamo and A. D. Banchick, *J. Mat. Sci.*, 15, p. 222 (1980).

48. M. Prud Homme, B. Lavelle, B. Pieraggi and F. Dabosi, *J. Cryst. Growth*, 19 (1), p. 65 (1973).

49. U. Dahmen, *Acta Met.*, 30, p. 63 (1982).

END

1-81

DTIC